Probing Single Cell Biomechanics With Optical Trapping and Phonon Microscopy

Thesis submitted to the University of Nottingham for the degree of **Doctor of Philosophy, 8th of November, 2024.**

William Hardiman

14342537

Supervised by

Amanda Wright
Fernando Pérez-Cota
Claire Friel
Matt Clark

Signature _____

Date _____ / _____ / _____

I dedicate this to Ola, for all your love.

Acknowledgements

I would not have been able to complete this thesis without help and support from everyone around me. Firstly, my team of supervisors: Amanda, Fernando, Claire, Alan and Matt. Each has provided unique insight and support throughout; Amanda, you have guided and helped me in seeing the importance of finishing things instead of answering every possible question; Claire, your advice "find a method that works and then get as many results as possible with it" was instrumental in my experimental approaches. To Sal and everyone in SIOS for helping me with myriad questions: remember there are no stupid questions, just inquisitive idiots. To Francesca, for a series of inspiring conversations about Brillouin scattering in hydrated materials which were instrumental in the discussion and future work presented here. To Nico Sturman and the Micro-Manager community at *image.sc*, thanks for helping make my data acquisition possible. To my family and friends, I thank you for kind words of encouragement, and engagement in conversations about my work. Although you might not have understood everything, explaining it to you helped me reframe and contextualize so that a wider audience may understand what I have done. To Pact Coffee and Des Rêves et Du Pain, for nourishing and inspiring me whenever I turned to you. To Hercules, for reminding me that even when I'm working I have to take care of myself and those around me. And also for countless mice. To Mum, for enabling everything I have done and encouraging me throughout whilst reminding me to eat well. And lastly to Ola, who has been here for me throughout, inspiring me to do my best work and be my best self. The ideas you have provided me with cannot be quantified or summarised and neither can your love or support.

Abstract

Single cell biomechanics is concerned with the viscoelastic properties of biological organisms on the length scales of whole cells and the macromolecules that comprise them (tens of microns to nanometres). This is an area of increasing research interest, with biomechanics being found to affect many healthy and diseased states of the cell. Many cell types are sensitive to the mechanical properties of their surroundings, which affects not only their own mechanical properties, but also such diverse things as mitotic cell division and stem cell differentiation. In probing cell mechanics, the cytoskeleton is of particular interest due to its multifaceted role; it is a prestressed network of proteinaceous filaments and cross-linkers which has been described as the source of order in the cell. The cytoskeleton is crucial to mechanosensing, force transduction, cell motility and division, and to regulation of the mechanical properties of cells. Many diseases are pathologies of the cytoskeleton, and it is a common target for anti-cancer drugs.

Here are included novel measurements using Brillouin light scattering including those of live cells demonstrating the potential for live cell study. Finally, the results from different techniques are compared, contrasted and discussed. Actin disruption in live cells by 1µM latrunculin B was found by external passive microrheology to reduce geometric stiffness by $4\,\mathrm{N/m}$

after 40 minutes (median from 11 cells); a time course experiment with phonon microscopy found longitudinal elasticity reduced by 3.6% after 26 minutes with continued slow softening over 2 hours. To my knowledge, no prior publications report a time course of cell elasticity during cytoskeletal disruption. Microrheology experiments without drug treatment revealed cells stiffening $2\,\mathrm{N/m}$ and while cytoskeletal active strain rate decreased, the stress rate increased; this is the first such observation of changes in cell stress rate.

This thesis is concerned with the measurement of cellular viscoelasticity, and bringing together information from two measurement techniques which probe vastly different aspects of cell mechanics. The bulk of the thesis focusses on microrheology of living cells, with an analogy developed between a bead bound to the cell and an optically trapped bead: first a theoretical framework is built for data interpretation; next microrheological analyses are developed for measurements with optical tweezers; then results obtained from non-invasive measurements of live cells are presented and discussed. Phonon microscopy, based upon picosecond laser ultrasound, is detailed and applied to cell measurements; study of cytoskeletal dynamics within live cells is demonstrated.

Research Outputs

The work presented in this thesis contains aspects which have been published in peer-reviewed journals and presented orally at both national and international conferences. Additionally, I was a finalist for the Faculty of Engineering Three Minute Thesis (3MT) competition in 2022. Here follows a complete list of publications I have contributed to and conference presentations I have made.

Publications:

Picosecond Ultrasonics For Elasticity-Based Imaging And Characterization Of Biological Cells. Pérez-Cota, F., Fuentes-Domínguez, R., La Cavera, S., Hardiman, W., Yao, M., Setchfield, K., Moradi, E., Naznin, S., Wright, A., Webb, K.F. and Huett, A., 2020. Journal of Applied Physics, 128(16), p.160902.

Living Cells as a Biological Analog of Optical Tweezers – a Non-Invasive Microrheology Approach. Hardiman, W., Clark, M., Friel, C., Huett, A., Pérez-Cota, F., Setchfield, K., Wright, A.J., and Tassieri, M., **2023**. *Acta Biomaterialia.*

Parallel Imaging with Phonon Microscopy. Fuentes-Domínguez, R., Yao, M., Hardiman, W., La Cavera, S., Setchfield, K., Pérez-Cota, F., Smith, R.J., Clark, M., **2023**. *Photoacoustics.*

Classification Of Cancer Cells At Sub-Cellular Level By Phonon Microscopy And Deep Learning: Towards Phonon-Based Diagnostics. Pérez-Cota, F., Martinez-Arellano, H., Hardiman, W., La Cavera, S., Thornton, L., Fuentes-Domínguez, R., Smith, R.J., McIntyre, A., Clark, M., **2023** *Scientific Reports.*

Label-Free 3D Phononic Endo-Microscopy and Elastography of Sub-Micron Biology. La Cavera, S., Hardiman, W., Yao, M., Pérez-Cota, F., Fuentes-Domínguez, R., Chauhan, V., Smith, R.J., Clark, M., **2024**. *Communications Biology*

Conference Presentations:

Living Cells as a Biological Analog of Optical Tweezers – a Non-Invasive Microrheology Approach. Hardiman, W., Clark, M., Friel, C., Huett, A., Pérez-Cota, F., Setchfield, K., Wright, A.J., and Tassieri, M., 2024. *Poster at Annual European Rheology Conference, Leeds, UK.* Awarded poster prize by Royal Society of Chemistry journal, Soft Matter.

Advances in Phonon Microscopy of Live Cells. Hardiman, W. Pérez-Cota, F., Fuentes-Domínguez, R., La Cavera, S., Setchfield, K., Friel, C., Smith, R., Clark, M., Wright, A.J.. 2023. *Oral presentation at BioBrillouin 2023, Dublin, Ireland.*

Non-invasive Microrheology of Living Cells. Hardiman, W. Clark, M., Friel, C., Huett, A., Pérez-Cota, F., Setchfield, K., Tassieri, M. and Wright, A.J.. 2022. *Oral presentation at Photon 2022, Nottingham, UK.*

Non-invasive Microrheology of Living Cells. Hardiman, W. Clark, M., Friel, C., Huett, A., Pérez-Cota, F., Setchfield, K., Tassieri, M. and Wright, A.J.. 2022. *Oral presentation at Photon 2022, Nottingham, UK.*

Non-invasive Microrheology of Living Cells. Hardiman, W. Clark, M., Friel, C., Huett, A., Pérez-Cota, F., Setchfield, K., Tassieri, M. and Wright, A.J.. 2022. *Oral presentation at Oxford Biomedical Imaging Festival, Oxford, UK.*

Phonon Microscopy of Live Cells. Hardiman, W. Pérez-Cota, F., Fuentes-Domínguez, R., La Cavera, S., Setchfield, K., Friel, C., Smith, R., Clark, M., Wright, A.J.. 2022. *Oral presentation at 1st Conference on Brillouin Light Scattering for Life Science and Biomedical Applications, Lyon, France.*

Statement of Contribution

The optical trapping microscope detailed in Chapter 3 was already built at the time I started this work. Due to changes in laser safety rules, I had to redesign, rebuild, and realign the optical system. Removing a lens from the beam path to change the focal position of the bead was my idea. Data acquisition for particle tracking experiments was performed using custom software designed and developed by myself and run within Micro-Manager. Confocal images in Chapter 4 were from cells cultured and stained by myself with the guidance of Kerry Setchfield and Alan Huett, and imaging was performed by me using the Zeiss Airyscan 2 Confocal Laser Scanning Microscope at the Nanoscale and Microscale Research Centre in Nottingham.

Passively measuring cell rheology using optical trapping and functionalised beads was first suggested by Manlio Tassieri and the optical trapping analogy was demonstrated by Rebecca Warren[1]. This prior work did not include observations of active strain generation, nor did it include the detailed quantitative analysis that I developed and demonstrate in Chapter 4. Interpretation of the results in the context of cellular response to bead binding is my own. Numerical methods for quantification of microrheology measurements were designed and developed by myself under the guidance of Manlio Tassieri. Elements of the work in Chapters 3 and 4 has been

published under the title "*Living Cells as a Biological Analog of Optical Tweezers – a Non-Invasive Microrheology Approach*" and presented at several conferences.

The phonon microscope was built by Fernando Pérez-Cota circa 2016[2], and I helped to deconstruct and rebuild it during the course of this work, including redesigning the optical paths to allow multiple experiments using the same laser system and integration of fluorescent imaging used during live cell experiments. I automated the fluorescent imaging with control of illumination LEDs and software to integrate image acquisition into the experiment. Use of an infra-red probe beam to study live cells had not been demonstrated prior to this work and the experiments performed to probe the contribution of the actin cytoskeleton were of my design. Aspects of the cell death study in Chapter 5 have been published under the title "*Picosecond Ultrasonics For Elasticity-Based Imaging And Characterization Of Biological Cells*" and presented at BioBrillouin conference.

Contents

Chapter 1

Introduction

1.1   Introduction to Mechanobiology

To define mechanobiology I turn to the words of revered mechanobiologist, Donald Ingber[3]:

"The recent convergence between physics and biology has led many physicists to enter the fields of cell and developmental biology. One of the most exciting areas of interest has been the emerging field of mechanobiology that centres on how cells control their mechanical properties, and how physical forces regulate cellular biochemical responses, a process that is known as mechanotransduction"

Current understanding of mechanobiology highlights the importance of length scales and time scales. Starting at the top, an organism is made up of organs, organs are made up of tissues, tissues are made up of cells and extra-cellular matrix, both of which are made up of molecules[4]. At every scale, there is order and organisation which contribute to the function of that "component". Order is characterised by molecules within liv-

ing systems being far from thermal equilibrium - proteins are folded and not aggregated, and information is stored not dissipated. Organisation is characterised by the concentration gradients maintained across different membranes within a living system. The primary interest of this thesis is at the interface of the cellular and molecular scales; at this scale there are many questions in the fundamental science that are unanswered.

We know that mechanics are implicated in diseases at the cellular scale: there are many diseases of mechanotransduction[3], meaning a dysfunctional cellular response to forces and mechanical properties is at the core of the disease. Other diseases are caused by cytoskeletal dysfunction[5–7]. Many of each are characterised by a change in the mechanical properties of the cells in question[5, 8, 9]. During metastases, cancer cells will spend some time in an adherent state when invading tissues and some time in a suspension state when circulating in the blood supply; throughout this, they are able to regulate their mechanical properties and apply forces upon their environment, enabling them to travel through the body where they sustain wide ranges of hydrostatic pressure and shear stresses[10, 11].

Mechanics are not just relevant to disease. The mechanical properties of a cell's milieu affects its behaviour[12, 13], morphology[14], and fate (resultant cell type after differentiation of stem cells)[15, 16]. I consider this adequate justification for why further interdisciplinary research into mechanobiology has great potential, not just as an interesting research question but also to develop medicines and improve lives.

1.2 The Cytoskeleton

Scaling down from cells and tissues to biomolecules, the concept of the cytoskeleton has been especially useful. Present in almost all known cells[4, 17], the cytoskeleton is a network of filamentous proteins[18], regulated by a suite of accessory proteins which can modulate the stability of fibres and polarity of cells, or generate forces required for both cell movement and for intracellular transport[19].

Taking guidance from the words of Paul Weiss;

"Lest our necessary and highly successful preoccupation with cell fragments and fractions obscure the fact that the cell is not just an inert playground for a few almighty masterminding molecules, but is a system, a hierarchically ordered system, of mutually interdependent species of molecules, molecular groupings, and supramolecular entities; and that life, through cell life, depends on the order of their interactions" [20]

I note that the cytoskeleton is regulated by a large number of proteins, many of which have received little study[21]. Thus a bottom-up study of cellular mechanobiology (i.e. in-vitro mechano-biochemistry such as rheology measurements of actin solutions) can only capture a tiny snapshot of what happens inside live cells. Equally, the regulation of the cytoskeleton by the environment of the cell (both chemical and mechanical) means it is hard to translate experiments at the cellular scale to in-vivo understanding.

The two cytoskeletal filaments which have received the most attention are actin filaments and microtubules, which are conserved across all eukaryotic cells and some prokaryotes[4, 17]. Intermediate filaments are a broader class with 6 types expressed in different tissues[22], including alpha-keratin which makes hair and nails. Greater in number, however, are the proteins
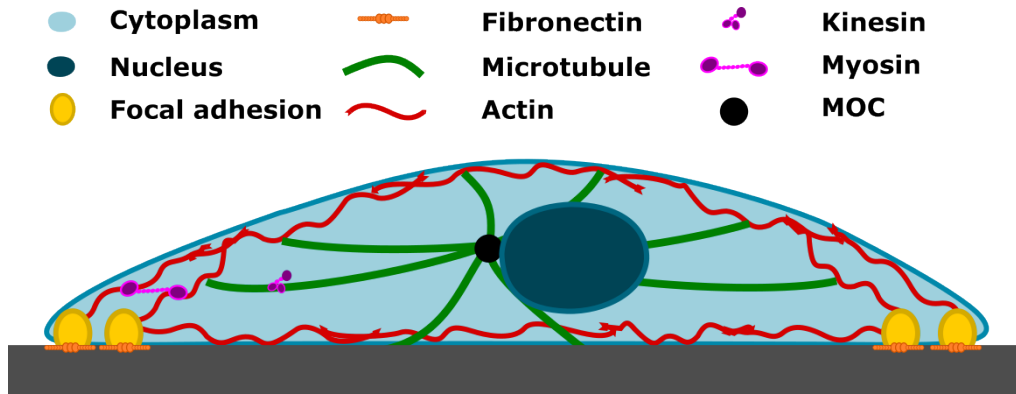
Figure 1.1: The Cytoskeleton of an Adherent Cell

Schematic of an adherent cell, showing focal adhesions binding to a substrate via fibronectin coated onto the substrate. The actin cytoskeleton is connected to fibronectin coated on the substrate via focal adhesions, and to the microtubule organising centre (MOC) via microtubules. Two types of motor protein are shown: myosin cross-links actin fibres, and kinesin transports vesicles along the microtubules.

which interact with either of these filaments[18], including motor proteins such as myosin which generates stress by cross-linking actin filaments[23].

Actin filaments have a diameter of 7 nm and 0.3-10 µm in length, while microtubules are 25 nm in diameter and 1-100 µm in length[24]. The key difference to their function, however, is not the dimensions but the mechanics and organisation. Actin is a semi-flexible polymer, with persistence length (a measure of stiffness) of around 10 µm[25, 26], while microtubules are stiffer with a persistence length of up to millimetres[27, 28]. Actin mostly localises to a cortical layer around 200 nm thick, while microtubules radiate from microtubule organizing centres within the cell. This organisation is shown in Figure 1.1 along with motor proteins and focal adhesions where the cytoskeleton links to the extracellular matrix.

The actin cortex is reported to provide the cell with the majority of its resistance to deformation. Constant turnover of filaments drives contractility and motility[29, 30], and is crucial to force balance between the cell and its surroundings[31] (either extra-cellular matrix or other cells). The

microtubule network is less dynamic[32], and aside from acting as transport routes for kinesin, the rigid struts are somewhat analogous to tent poles[33]. Compression in microtubules balances tension in the actin cortex[34], and they also act as mechanotransducers, transmitting forces to the interior of the cell[33].

In the tent analogy of cell mechanics, the pegs which anchor the cell and transmit forces to its surroundings are focal adhesions. *In vivo*, focal adhesions facilitate cell motility and support prestress by integrin receptors binding to extracellular matrix proteins[35]. A variety of signalling pathways, both biochemical and mechanical, accompany focal adhesion maturation after integrin binding and lead to recruitment of cytoskeletal proteins such as actin, vimentin and talin[36, 37]. The mechanical coupling of the extracellular matrix to the cytoskeleton allows cells to sense forces from and mechanical properties of their surroundings[38].

1.3 Cell Lines

Immortalised cell lines are a key tool for biological research, with most *in vitro* study using stable cell lines rather than primary cells directly from a donor. The first immortalised human cells and now the most common cell line, HeLa cells, have been widely used over the last 70 years and much of what we know about both physiological and pathological processes in human cells comes from study of HeLa cells[39]. As a rough metric for their ubiquity, a PubMed search for articles in the last 20 years mentioning "HeLa cells" returns almost 80,000 articles, while similar searches for the next two most common human cell lines, "HEK cells" and "MCF-7 cells", returned around 10,000 and 40,000 articles respectively.

HeLa cells, named after their donor Henrietta Lacks, are the subject of an ethical debate because Henrietta Lacks (the tissue donor) did not consent for her biopsy to be used in research. Public opinions on this case have lead to regulatory changes, including the requirement of informed consent for participation in studies. While HEK cells, an acronym for Human Embryonic Kidney, are not subject to this debate, bioethics in the Netherlands in 1977 were in their infancy with the legalisation of abortion in 1984[40], making it unlikely that consent was obtained for the use of aborted fetal tissue.

As they are the most studied and characterised cell line, cessation of the use of HeLa cells would necessitate huge repetition of scientific endeavours. Furthermore, the ethical issues around consent are not unique to HeLa cells as there was little call for regulation regarding the use of tissues from live patients until the 1970s[41]; this means the next two most common human cell lines are likely subject to similar ethical issues surrounding their origin. Phasing out the use of cells with ethical qualms about their origins would necessitate researchers discarding decades of research performed on numerous cell lines, making it inpractical and wasteful.

In this work, HeLa cells are used to study the mechanics of cellular adhesion and cytoskeletal disassembly. The cytoskeleton is highly conserved across eukaryotic cells[4], with actin expression being ubiquitous. The interaction being studied here is that triggered by the binding of streptavidin to integrin receptors, an interaction where HeLa cells are believed to behave similarly to other cell lines[42, 43]. HeLa cells are the most widely used cellular model system and have been studied in great detail[39]. Despite this, it is worth acknowledging that HeLa cells are not always "typical" cells. The techniques/methods developed on HeLa cells can, however, be transferred to a system of specific relevance to a future biological question.

1.4 Objectives of the Thesis

The objective of this thesis is to develop non-invasive biomechanical measurements which are compatible with live cell study, and to compare results from different techniques probing different length and time scales. The two techniques I have chosen, microrheology and phonon microscopy, each have unique strengths and challenges in implementation. The aims for each differ due to the various challenges presented by the two techniques. Herein I present External Passive Microrheology (EPM), a method and *novel* analysis for measuring the viscoelastic properties and active stress generation of single live cells, and development of phonon microscopy for live cell study.

External Passive Microrheology will be applied to study the mechanical effects of cytoskeletal processes in live cells without deforming cells by applying external forces. To this end, data acquisition needs to be developed and optimised to allow thousands of images per second to be acquired, and processed to track the position of a microsphere which will be stored for further processing. Development of analysis methods is needed to interpret particle tracking experiments to find the mechanical properties of the sample; this includes a new theoretical framework based upon conventional analysis of optical trapping data and improved to account for the complexities of live cell study. Concerned with these goals are Chapters 3 and 4.

Phonon microscopy will be used to measure the change in mechanical properties of cells with higher spatio-temporal resolution than offered by microrheology. First, the sensitivity will be confirmed by study of the effect of cytoskeletal targetting drugs applied before fixing cells. Transitioning to live cell work, biocompatibility will be the biggest challenge. Previous phonon microscopy has used ultraviolet pump beams, however

infrared wavelengths are expected to be more biocompatible. To make this change, opto-acoustic transducer designs need to be trialled with the aim of enabling longer experiments; experimental protocols for live cells also need consideration. Sample heating during the creation of coherent acoustic pulses introduces a systematic error on measurements of Brillouin frequency, necessitating internal controls in experimental design for live cell work. The effect of cytoskeletal disruption on live cells will be investigated, including a spatially resolved time course of cell elasticity during disruption of actin. All work towards these aims is contained within Chapter 5.

The goals stated above are written in a numbered list on the next page.

1. Passive Microrheology measurements of live cells:

    1.1. Develop software to perform video microrheology data acquisition on an existing optical trapping microscope.

    1.2. Develop analyis software to process microrheology data:

        1.2.1. Implement methods to perform numerical inversion from time to frequency domains.

        1.2.2. Create methods to measure characteristic relaxation times and frequencies.

    1.3. Perform live cell experiments:

        1.3.1. Develop analytical framework to quantify cell stiffness and viscosity.

        1.3.2. Measure changes in cell mechanical properties and active force generation over time.

        1.3.3. Elucidate the effect of actin disruption on cell stiffness, viscosity and active force generation.

2. Phonon microscopy measurements of live cells:

    2.1. Demonstrate sensitivity of phonon microscopy to the effects of cytoskeletal disruption using fixed cells.

    2.2. Develop biocompatibility of the technique:

        2.2.1. Fabricate transducers for both pump and probe at infrared wavelengths.

        2.2.2. Implement fluorescence imaging including hardware control and image processing to determine cell death time.

        2.2.3. Investigate factors contributing to biocompatibility including heating and laser light exposure.

    2.3. Measure the effect of actin disruption in live cells:

        2.3.1. Design experiment with an internal control.

        2.3.2. Develop and test drug delivery method.

        2.3.3. Process data to yield spatiotemporally-resolved cell elasticity during actin disruption.

Chapter 2

Background

The roles that forces and mechanics play in the behaviour of tissues and cells has been of increasing interest in the last thirty years[3, 44–46]. A suite of techniques, made possible by technological advances, are now available for studying the mechanics of cells[6, 47–52]; this in turn has resulted in a suite of mechanical models for cells, in order to understand the results from those techniques[53–55]. Fundamental mechanobiology, i.e. how do forces and mechanics matter to cells, presents many interesting questions such as how do cells sense forces and respond[45, 56–58]. These, however, are little good to society without asking also "how does this affect the health of an organism?" thus researchers have sought to understand the interplay between biomechanics, mechanotransduction and disease[8, 9, 59–62].

In this work I employ two different approaches to characterising different mechanical properties of single live HeLa cells. External Passive Microrheology (EPM, Chapter 4), a technique I have developed, uses optical trapping to position a bead on the surface of a cell where it adheres, before the trap is turned off. Particle tracking microrheology is then used to infer both the complex shear modulus and the active stress generation of the cell as

the adhesion site develops over tens of minutes. Phonon Microscopy (PM, Chapter 5) uses a femtosecond laser pulses to generate and detect coherent acoustic pulses within a cell, probing the longitudinal elastic modulus of the cell during disruption of the actin network.

The two techniques introduced above probe different viscoelastic parameters of the cell and vastly different time scales. EPM reports the shear modulus over milliseconds to tens of seconds and stress generation of cells over hundreds of seconds, and cells are modelled as soft viscoelastic materials. PM measures the longitudinal modulus at timescales less than a nanosecond, where cells behave like compressible elastic solids. Both apply low strains to the cells, meaning effects like fluidisation can be ignored (more detail on this in Section 2.2.5). Crucially, PM can resolve sub-cellular structures with $\sim 1\,\mathrm{s}$ temporal resolution while EPM has no spatial resolution and temporal resolution of over one minute.

This section aims to critically compare single-cell biomechanics measurement techniques, the models used to interpret the techniques, and how each has contributed to our understanding of the field. The relevant rheology and microrheology theory is explained in Section 2.2, with Figure 2.2 showing the deformation geometries for different viscoelastic moduli. The physics underpinning optical trapping and Brillouin scattering is explained in Section 2.3. Finally the impact of this work is discussed in the context of the field in Section 2.4.

2.1 Single-Cell Biomechanics

Many techniques measure subtly different parameters of the cell, at different length and time scales, such that their findings are not directly
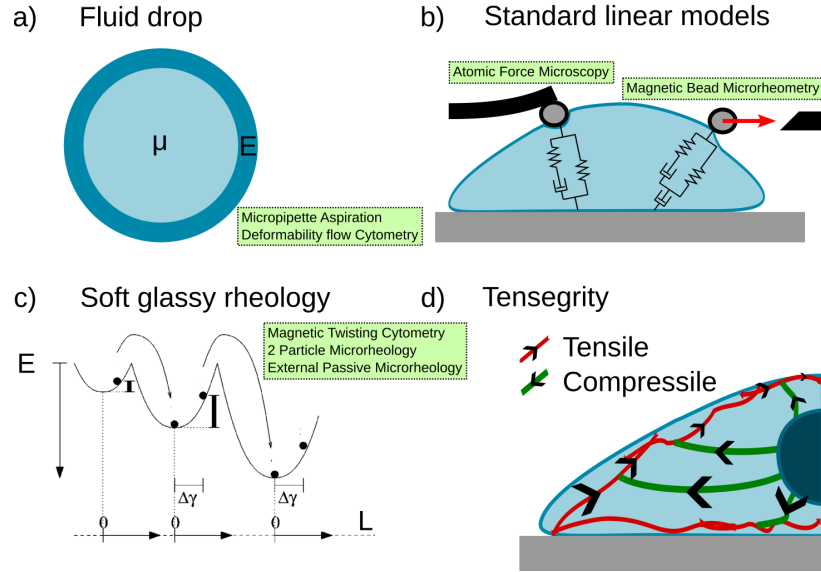
Figure 2.1: Cell mechanical models and techniques they have been applied to (green boxes). a) Fluid drop model comprising of a cortical elasticity E and a cytoplasmic viscosity μ are commonly used for whole-cell deformation of suspension cells. b) Standard linear models combining elastic (spring) and viscous (dashpot) elements can be fitted to displacement-time curves. c) Soft glassy rheology (diagram adapted from [63]), characterised by discontinuous relaxation as elements (dots) jump from one well to another, in low strain experiments. d) Tensegrity, the balance of tensile and compressile forces by different elements within the cell, has been used to explain the role of the cytoskeleton in cell mechanics and more generally cellular signalling in response to applied forces.

comparable. To further complicate any comparison, cells do not behave as ideal viscoelastic materials and exhibit a yield strain which may be as low as a few percent[63, 64]. Thus techniques have been divided into two categories: active techniques in which an external force is applied to the cell, and passive techniques in which there is not; they are summarised in Tables 2.2 and 2.1 respectively. Four models of particular interest have been identified and summarised in Figure 2.1. References to the tables and figure have been omitted from the text to improve readability.
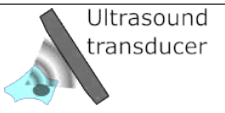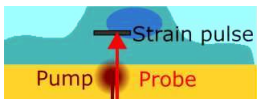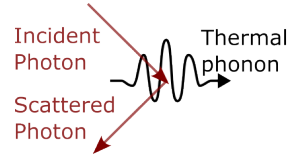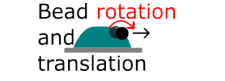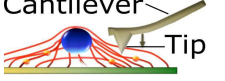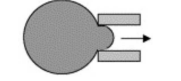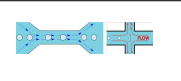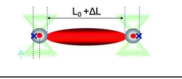
Technique	Length Scales Probed	Frequencies Probed	Quantities Measured	Schematic
Photoacoustic Microscopy[65]	>10µm∗	<1Hz	Thermal stress generated by optical absorption	
Scanning Acoustic Microscopy[66]	∼µm†	∼100MHz†	Acoustic velocity, Acoustic attenuation, Thickness	
Phonon Microscopy (Chapter 5)[67]	∼ 100nm axially, ∼ 1µm laterally	GHz	Longitudinal elastic modulus M', Acoustic attenuation	
Stimulated Brillouin Scattering[68]	∼ 2.5µm axially, ∼ 0.5µm laterally	GHz	Longitudinal complex modulus $M^*(\nu_B)$	
Magnetic Twisting Cytometry[50]	∼ 1µm	$10^{-2} \to 10^3$Hz†	Complex shear modulus $G^*(\omega)$	
Magnetic Bead Microrheometry[69]	Up to 7µm∗	0.1→10Hz†	Shear viscosity, cortical elasticity	
Atomic Force Microscopy[6]	Up to 20% of the cell by height	$1\,\text{Hz} \to$ kHz†	Young's modulus E	[6]
Optical Stretching[49]	Whole cell	<1 Hz	Shear viscosity, cortical elasticity or tension	
Micropipette Aspiration[70]	1µm → Whole cell	$1\text{mHz} \to 1\,\text{Hz}$†	Shear viscosity, Cortical elasticity or tension	[70]
Deformability Flow Cytometry[71]	Whole cell	10Hz → 20kHz†	Deformation ratio, Cortical elasticity or tension	
Optical Trapping Deformation[72, 73]	Whole cell	$1\,\text{Hz}{\to}1\text{kHz}$†	Shear viscosity, Cortical elasticity or tension	[72]

Table 2.1: Active cellular biomechanics measurement techniques. Length- and time-scales (frequencies) probed and typical quantities extracted are given for each. Frequencies marked with † indicate they are limited by the instrumentation (typically camera speed). The length scale probed by photoacoustic microscopy (marked ∗) is sample-dependent, as discussed in the text. Contradictory results have been published for the length scale probed by magnetic bead microrheometry[48, 69] (marked ∗), and are discussed in the text. Schematics with a reference are replicated from the cited publications.

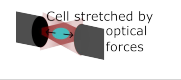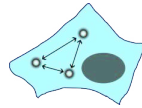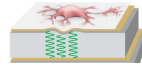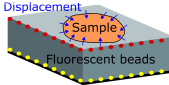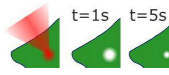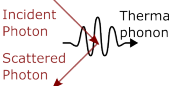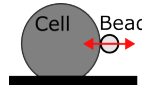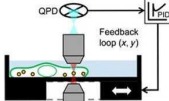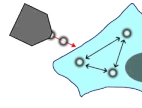| Technique	Length Scales Probed	Frequencies Probed	Quantities Measured	Schematic
Endogenous Tracer Microrheology[23]	$1 \rightarrow 10\mu m$	$\sim 0.1 \rightarrow 100 Hz$†	Complex shear modulus $G^*(\omega)$, Stress fluctuation spectrum $\Delta(\omega)$	
Elastic Resonator Interference Stress Microscopy[74]	$2\mu m \rightarrow$ whole cell	$<1Hz$	Normal component of cell prestress	[74]
Traction Force Microscopy[75]	$0.1\mu m \rightarrow$ whole cell	$<0.1Hz$	In-plane component of cell prestress	
Fluorescence Recovery After Photobleaching[76]	$\sim 1\mu m$	$<1Hz$	Nanoscale shear viscosity	
Spontaneous Brillouin Microscopy[77, 78]	$\sim 1\mu m$	GHz	Complex longitudinal modulus $M^*(\nu_B)$	
External Passive Microrheology (Chapter 4)[79]	Up to microns	$1mHz \rightarrow 1kHz$†	$G^*(\omega)$ for $\omega \gtrsim 1Hz$, Strain fluctuations for $\omega \lesssim 1Hz$	[79]
Feedback Tracking Microrheology[?]	$\sim 1\mu m$	$10^{-2} \rightarrow 10^5 Hz$ †	Complex shear modulus $G^*(\omega)$	[?]
Ballistic Injection Nanorheology[52]	$1 \rightarrow 10\mu m$	$0.1 \rightarrow 100Hz$†	Complex shear modulus $G^*(\omega)$, Stress fluctuation spectrum $\Delta(\omega)$	

Table 2.2: Passive cellular biomechanics measurement techniques. Length- and time-scales (frequencies) probed and typical quantities extracted are given for each. Frequencies marked with † indicate they are limited by the instrumentation (typically camera speed). Schematics with a reference are replicated from the cited publications.

2.1.1 Active Techniques

Active techniques for probing single cell mechanics, that is to say methods where an external force is applied to cells, are listed in Table 2.2. Below I divide them based upon the length-scale probed.

2.1.1.1 Whole Cell Deformations

The first single-cell biomechanics measurements were made by deforming whole cells via micropipette aspiration (MA). A pipette with internal diameter less than the size of a cell is pressed against the cell and hydrostatic pressure is used to aspirate the cell partially into the pipette[47, 70, 80]. In early experiments, researchers identified that small cellular deformations are dominated by the elasticity of a cortical layer of the cell (referred to as membrane tension), while larger deformations cause the cell to flow in a viscous manner. Thus the cell was modelled as an elastic cortex filled with viscous cytoplasm.

The simple model used for micropipette aspiration is useful for analysing large and fast deformations of suspension cells. One application is deformability flow cytometry (DFC), in which cells are individually subjected to shear or extensional stress (depending on the geometry used) of up to kPa[71, 81]. The high throughput of DFC (hundreds of cells per second) means it is one of the few biomechanical techniques found in the clinic where it is used for cell phenotyping. The high stresses applied to cells, however, means that the viscosity value calculated from DFC is not necessarily comparable to that which may be found by other techniques.

Both MA and DFC are typically applied to suspension cells, as are optical trapping (OT) deformation techniques and optical stretching (OS).

15

Optical trapping techniques include use of beads adhered to the cell as "handles" which can be optically trapped, while optical stretching uses the forces applied to a cell by light in order to deform it. The magnitudes of stress applied, however, is very different to DFC or MA, with the optical techniques applying stresses on the order of a few Pascals[49]. As a result, both OT and OS probe mechanical properties closer to the unperturbed state of the cell, avoiding effects of rejuvenation caused by large strains. The optical stretcher can measure a cell in around a second, making it suitable for cell-population studies; this revealed the correlation between cancer cell deformability and malignancy (i.e. malignant cells are more deformable)[59]. Optical trapping measurements take longer (seconds to minutes per cell), but have demonstrated the importance of pre-stress and deformation history for suspension cells[72] and elucidated the mechanical properties of red blood cells in sickle cell anaemia[8] and malaria[9].

2.1.1.2 Point-Contact Measurements

Other techniques listed in Table 2.2 are mostly applied to adherent cells. While study of suspension cells allows for higher throughput and clinical applications, adherent cells are more widely studied. One common method is to use an external probe, such as a bead adhered to the cell, both for applying forces to the cell and tracking the resultant deformation.

Atomic force microscopy (AFM) is often lauded as the gold standard for biomechanical measurements of adherent cells because it directly measures Young's modulus[82, 83]. However the measurement can be influenced by to the tip geometry, the indentation depth and speed[84]. Furthermore, force-indentation curves necessitate use of preconceived models to fit data; commonly used are standard linear models comprising elastic springs and

viscous dashpots.

AFM is limited to studying the apical surface of cells but has revealed a connection between mechanical and electrical activity of nerve cells[85] as well as finding numerous application in the study of cancer cell mechanics[86]. Force-indentation curves are commonly analysed using standard linear models, however they may also be analysed using the soft glassy rheology or the poroelastic model[87]. The poroelastic model and its implications for microrheology are discussed in more detail in Section 2.2.4.

Magnetic twisting cytometry (MTC) has been one of the driving forces in understanding the glassy (slow-relaxing) nature of cell viscoelasticity[50], and key to this is the soft glassy model of cell rheology[88]. Applying a torque to a magnetic bead adhered to the cell surface, MTC measures the shear modulus of the cell via the bead lateral displacement. It has been applied at length to study non-linear relaxation of cells, including rejuvenation and the role that macromolecular crowding plays in cell mechanics[89–91], as well as the role of cytoskeletal remodelling in the abnormal behaviour of airway smooth muscle cells in asthma[89, 92]. The rejuvenation (recovery of unperturbed mechanical properties after deformation) of cells was revealed to follow a power-law form, also indicative of glassy rheology[88, 90].

Magnetic bead microrheometry (MBM) is conceptually similar to MTC, applying a pulling force instead of a torque, and allows for much larger force magnitudes (nN instead of pN)[69]. This may alter the compliance of the cell, which exhibits viscoelastic response with a relaxation time of $\sim 0.1\,\mathrm{s}$ and a viscous response at long times, both well described by a single standard linear model[48]. By using both magnetic and non-magnetic beads, MBM can be used to study the propagation of stress across a cell as any deflection of the non-magnetic bead is caused by cellular strain.

Such experiments revealed that the viscoelastic screening length varies between different cell lines with 3T3 fibroblasts having a screening length of around 7 µm and J774 macrophages exhibiting no induced deflections of non-magnetic beads[48, 69]. This suggests that the true length scale probed by biomechanical measurements depends on the viscoelastic properties and possibly cytoskeletal organisation of the cell under study.

2.1.1.3 Acoustic Measurements

The remaining active measurement techniques all utilise acoustic waves on some level. Scanning acoustic microscopy (SAM) is the microscopic analogue of a clinical ultrasound scanner, using a piezo transducer to generate and detect acoustic waves. Applications to single-cell study are few because the resolution is limited by the frequencies achievable by piezo transducers, however it should have excellent biocompatibility due to the low frequencies of the acoustic waves. Despite having low resolution it has been used to demonstrate differences in the speed and attenuation of sound waves between benign and malignant tissues[66].

Photoacoustic microscopy (PAM) uses a pulsed laser to generate a sound wave by localised heating, and a piezo transducer to measure the wave outside of the sample. Again, resolution is limited by the acoustic wavelength probed making it ill suited to single-cell applications, however the generation method allows for *in vivo* study of small animals[65]. While SAM directly measures acoustic parameters at MHz frequencies, PAM actually measures the optical absorption coefficient which is a quasi-static property of the sample.

Low resolution is a barrier to sub-cellular study for all-acoustic techniques such as SAM, PAM and acoustic micrometers. To perform acoustic mea-

surements at higher frequencies, generation and detection of ultrasound needs technologies other than piezo transducers. Phonon microscopy (PM, Chapter 5) uses a femtosecond pulsed laser and a multilayer opto-acoustic transducer to launch a coherent acoustic pulse into a cell, where it can be interrogated by a second laser pulse[93]. This allows axial resolution of a few hundred nanometres, however the acoustic pulse attenuates quickly and measurements are limited to within a few microns of the basal plane of the cell. It has provided insight into the mechanical behaviour of Acanthamoeba Castellanii during the encystation process that makes the single-celled organism so robust[94]. Further applications of PM have been limited so far by biocompatibility, however in this work I demonstrate protracted measurements of single live mamallian cells without killing them.

Stimulated Brillouin scattering (StBS) uses the interference pattern from two counter-propagating lasers to generate a sound wave via electrostriction and probe it by Brillouin scattering, achieving a resolution limited by the optical system. Applications thus far have been limited by high optical powers required due to the non-linear scaling of scattered light intensity and peak power[95], however recent advances using pulsed lasers to increase peak power while reducing average power have allowed for StBS study of single mammalian cells[68]. Even still, biological applications of stimulated Brillouin scattering are in their infancy.

2.1.2 Passive Techniques

Passive measurements of cell mechanics, listed in Table 2.1, occur at lower stresses and strain rates than active measurements. As a result, cellular prestress is lower but cells appear stiffer and more solid as they are not subject to fluidisation due to lower strains; additionally techniques based

upon passive microrheology also allow study of the active force generation within cells. Thus passive measurement techniques have the potential to reveal insights which are not accessible to active techniques. Additionally, a variety of different probes may be used, including synthetic micronspheres, sound waves, and fluorescent molecules, each probing different length-scales and quantities. Included in Table 2.1 is external passive microrheology (EPM), which is discussed in the context of the field in Section 2.4.

At the scale of molecules, fluorescence recovery after photobleaching (FRAP) probes cellular viscosity by photobleaching a spot within the cell and then monitoring the fluorescence intensity recovering as fluorophores diffuse into the bleached spot[76, 96]. Diffusion for particles smaller than the mesh size (hundreds of nanometres) is less hampered by macromolecular crowding and FRAP reports a nanoscale viscosity $20\times$ lower than the microscale viscosity[96]. This should be interpreted carefully, however, as the diffusivity measured may not be directly related to the viscosity. That is, the Stokes-Einstein relation ($\eta \propto 1/D$) may not hold true; in fact, cellular activity can increase the diffusivity of fluorophores[97]. While the phenomenon is not well understood, a possible explanation is that it is advantageous to the cell to have non-specific transport faster than diffusion alone would achieve.

Each of the techniques mentioned thus far have probed cellular compliance, be it viscosity or elasticity, however the force generation of cells is also of interest. Techniques such as traction force microscopy (TFM) and elastic resonator interference stress microscopy (ERISM) can measure the transverse and normal components, respectively, of the stress tensor at the cell surface. Each measures deformations of an elastic layer below the cell, limiting the time scale probed to the relaxation time of the elastic layer, typically on the order of a second. These techniques can quantify both

intercellular forces, with TFM finding forces of up to 200nN[98], and cell-substrate forces, with ERISM resolving the relation between fluctuations in the force applied by migrating cells and their speed[74, 99]. TFM can also measure the time evolution of the strain energy within cells, showing differences in force-time and strain energy-time response to contractile agonists[100], demonstrating the variability in cellular mechanical response to different chemical signals.

2.1.2.1 Passive Microrheology Techniques

Endogenous tracer microrheology (ETM) is the simplest cell microrheology experiment, in which motion of endogenous particles is tracked and analysed[23]. While the fluctuations of single particles can reveal the shear modulus of its milieu, correlations between nearby particles can reveal both the active stress fluctuation spectrum of the cytoskeleton and the shear modulus of the unperturbed cytoplasm (recall that colloidal particles alter the rheology of their surroundings, Section 2.2.4). This was able to confirm that the soft glassy rheology model can be applied to the cytoplasm as well as giving the first insight into the frequency distribution of cells' active stress fluctuations. Despite its simplicity, ETM has not found a wealth of applications due to its non-specificity: different subcellular components exhibit different diffusive behaviours, determined by their specific interactions and transport mechanisms.

Overcoming the problems presented by use of endogenous probes, ballistic injection nanorheology (BIN) uses compressed gas to fire probes into the cell. Again single probes can be studied as can the correlations between multiple probes. This enables study of more varied cellular systems and BIN has revealed cell stiffness in both 2D and 3D cultures[101, 102] as well

as revealing the role of the Rho signalling pathway in cellular response to shear flow[102].

To perform widefield particle tracking experiments, a fast camera is required, limiting the shortest timescale which can be probed. For single particle tracking experiments, laser interferometry with a quadrant photodiode at the back focal plane can be used to achieve higher temporal resolution; this comes at the cost of only being able to track particle position if it is within $\sim 200[\text{nm}]$ of the probe laser focus. To overcome this, feedback tracking microrheology (FTM) uses the position of probe particle to guide stage movements, hence keeping the probe within the linear response region of the quadrant photodiode[**?**]. Reporting over a wider frequency range than any other cell microrheology technique, FTM has demonstrated that soft glassy rheology is inherent to the cytosol and increases with macromolecular crowding[103**?**].

2.1.2.2 Spontaneous Brillouin Scattering

Microrheology experiments probe a length scale which is determined by the size of the probe particle, typically on the order of microns. Scaling down, thermally generated acoustic phonons with wavelengths of hundreds of nanometres can be probed by spontaneous Brillouin microscopy (SpBM). This allows for measurement of longitudinal viscosity and elasticity at the Brillouin frequency, typically GHz, where cells and even water are predominantly elastic (i.e. $M''(\nu_B) \gg M'(\nu_B)$). The length scale probed by Brillouin-scattering techniques is determined by the largest of the optical point spread function and the acoustic mode being probed; while higher numerical aperture lenses would increase the resolution of Brillouin scattering, it would also result in spectral broadening for StBS and SpBM[104]

and increased attenuation of phonon microscopy signals[67].

Brillouin scattering for single cell study is still in its infancy however recent advances in instrumentation have enabled a range of applications. A key challenge to studying biological samples, especially tissues, is isolating the Brillouin scattered light from the Rayleigh line, typically achieved with notch filters. As a non-invasive all-optical technique it is possible to make *in vivo* measurements such as studying the formation of the gastrointestinal tract in *Drosophila* embryos[105]. Studies on spinal cord repair in zebrafish have not only shown that an injury is accompanied by tissue stiffening, but also that excising tissues alters their mechanical properties, making it all the more important to develop *in vivo* biomechanical techniques[106].

The role of heterogeneity and interpretation of Brillouin frequency from biological specimens is a subject of contemporary debate in the bioBrillouin community, with some claiming Brillouin scattering merely probes water content[107]. Studying the dehydration of gelatine gels[108] enabled Bailey *et. al.* to disprove this, showing that Brillouin scattering probes stress relaxation and demonstrating a glassy transition at low hydration.

2.2 Rheology

Rheology, from Greek "rheos", meaning flow, is the study of deformations and flows of matter. Rheology experiments involve measuring the strain (in 1D this is change in length over original length $\epsilon = \Delta x/x$), and the stress, or force per unit cross-sectional area $\sigma = F/A$. This is commonly either measuring the time-dependent strain, $\epsilon(t) = x(t)/x_0$, within a sample in response to a step stress, σ_0; or measuring the time-dependent stress, $\sigma(t)$, in response to a time-varying strain, $\epsilon(t)$. In the latter case, analysis is
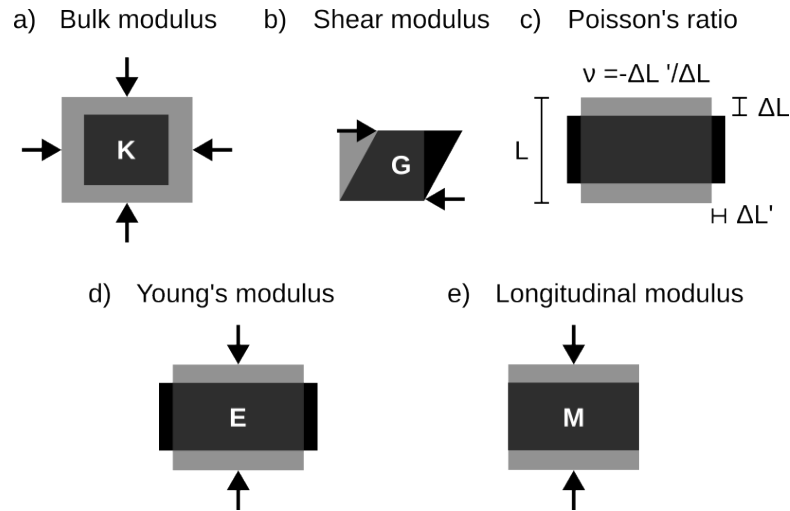
Figure 2.2: a) Bulk modulus determines material response to an isotropic stress. b) Shear modulus for "slippage" type deformations. c) Poisson's ratio, ν, describes compressibility of a material. d) Young's modulus determines response to uniaxial stress with unconstrained lateral dimension. e) Longitudinal modulus determines response to uniaxial stress with zero lateral strain.

typically carried out in the frequency domain.

Materials' response to deformations are often described in terms of the shear modulus, G, the Young's modulus, E , and Poisson's ratio, ν. Other common quantities are bulk modulus, K, and longitudinal modulus, M. For the case of an isotropic material, any two of these are adequate to fully describe any deformation. Figure 2.2 shows deformations which depend only on one of the moduli. Having demonstrated these four moduli, I will continue this section concerning myself only with the shear modulus as it is the modulus probed by microrheology, although much of the below theory can equally be applied to any of these moduli.

2.2.1 Constitutive Relations

The relation between stress, σ, and strain, ϵ, for a step-stress or an oscillatory strain can respectively be summarised by the relations:

$$\epsilon(t) = \sigma_0 J(t),$$
$$\hat{\sigma}(\omega) = \hat{\epsilon}(\omega) G^*(\omega) \tag{2.1}$$

with shear creep compliance, $J(t)$, defining the time-dependent relation and the complex shear modulus, $G^*(\omega)$, describing the frequency-dependent relation between stress and strain. In the more general case

Material response can equivalently be expressed in the frequency domain as complex modulus, $G^*(\omega)$, or in the time domain as creep compliance, $J(t)$, or shear relaxation modulus, $G(t)$. These equivalent quantities are related by [109]

$$\int_0^\tau G(t) J(\tau - t) dt = \tau, \tag{2.2}$$

$$G_r = \frac{dG(t)}{dt} = \hat{G}^*(t), \tag{2.3}$$

$$G^*(\omega) = \mathbf{i}\omega \hat{G}(\omega), \tag{2.4}$$

$$G^*(\omega) = G'(\omega) + \mathbf{i} G''(\omega), \tag{2.5}$$

with imaginary unit $\mathbf{i} = \sqrt{-1}$, time t, lag time τ, and angular frequency $\omega = f/2\pi$. Clearly the modulus and the compliance are inverse - a stiffer material has higher modulus and lower compliance. The complex modulus has a real part, the elastic (or storage) modulus G', and an imaginary part, the viscous (or loss) modulus G''.

Using the complex modulus to describe a material response has the primary advantage that the elastic and viscous components can be easily separated
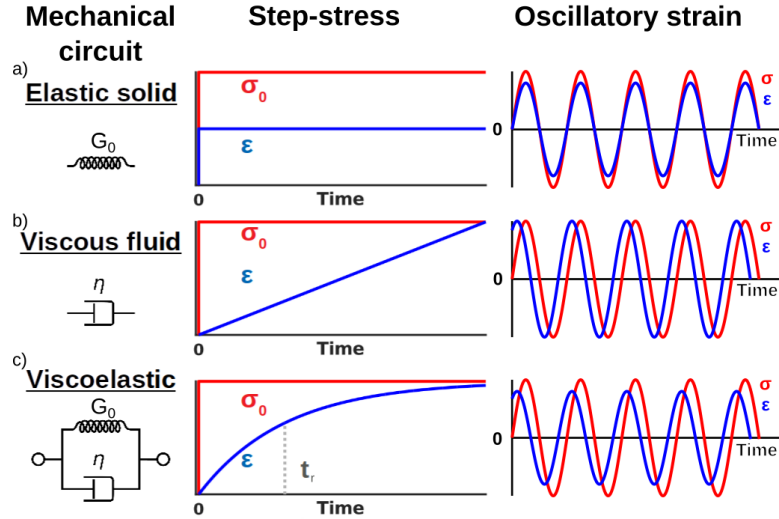
Figure 2.3: Mechanical circuits for three model materials (first column), the time-dependent strain (ϵ) in response to a step stress (σ_0) (second column), and the time-dependent stress (σ) in response to oscillatory strain (ϵ) (third column). Materials shown and their complex moduli are a) ideal elastic, Equation 2.6 b) ideal viscous, Equation 2.7 and c) Kelvin-Voigt viscoelastic, Equation 2.8.

and inspected. Using the three materials in Figure 2.3 as an example, the complex moduli for each could be written as

$$G_a^*(\omega) = G_0 \tag{2.6}$$

$$G_b^*(\omega) = \mathbf{i}\eta\omega \tag{2.7}$$

$$G_c^*(\omega) = G_0 + \mathbf{i}\eta\omega, \tag{2.8}$$

where G_0 is the elastic modulus, η is the viscosity and ω is angular frequency.

Note that while the model materials here have frequency-independent elasticity (a and c) and viscosity linear with frequency (b and c), viscoelastic materials may exhibit power-law behaviours for both. Furthermore, many materials exhibit a non-linear response for strain with increasing stress. Despite this, linear viscoelastic theory is relevant in this thesis as it forms the basis for microrheology theory and the Generalised Stokes-Einstein Re-

26

lation. The measurements performed here using passive microrheology and phonon microscopy are within the low strain regime, where living cells can be considered linear viscoelastic materials.

2.2.2 Microrheology

Particle tracking microrheology arguably began with Robert Brown's experiments observing pollen diffusing on the surface of water; these experiments lead to the discovery of Brownian motion. Before this, Fick was the first to predict the mean squared displacement (MSD) of a particle undergoing free diffusion[110],

$$MSD = \left\langle \Delta r^2(\tau) \right\rangle = \left\langle (r(t) - r(t+\tau))^2 \right\rangle_t = 2nD\tau, \quad (2.9)$$

where n is the number of dimensions the particle is diffusing in, τ is known as the lag time, with particle position $r(t)$ at time t and the time average denoted by $\langle \rangle_t$. (Strictly this would be an average over the independent observations of the displacement for a given lag time, i.e.: $t = m\tau$ for integer m, but using **all** values of t gives better SNR[111].)

To understand Brownian motion, we consider the forces acting upon a particle, via the Langevin equation:

$$m\vec{a}(t) = \vec{f}_G(t) + \int_0^t \vec{v}(\tau)\zeta(t-\tau)d\tau \quad (2.10)$$

where a particle of mass m has instantaneous acceleration $\vec{a}$ driven by a random (Gaussian) noise $\vec{f}_G(t)$ and damped by the integral term. The integrand consists of the particle velocity $\vec{v}(\tau)$ and a microscopic memory function, $\zeta(t-\tau)$, representing viscous drag in the suspension fluid.

Starting with the Langevin equation, Mason and Weitz[112] bridged the gap between microscopic behaviour and macroscopic properties. They note that the microscopic memory function, $\zeta(t)$ in Equation 2.10 is related to the velocity autocorrelation function by the correlations in the driving force f_G. For over-damped motion the velocity autocorrelation function can be used to determine the MSD. This can be seen by first recognising that the MSD is related to the position (x) autocorrelation function $\langle x(t_0 + \tau)x(t_0)\rangle_{t_0}$:

$$MSD(\tau) = 2\left(\langle r^2\rangle - \langle x(t_0 + \tau)\ x(t_0)\rangle_{t_0}\right); \qquad (2.11)$$

and then considering that for over-damped motion the mean force, velocity and displacement for a given time interval are all proportional. Thus the bulk viscosity of the fluid in Laplace space, $\tilde{\eta}(s)$ with Laplace frequency s, relates to the microscopic memory function by a constant of proportionality

$$\tilde{\zeta}(s) = 6\pi a\tilde{\eta}(s), \qquad (2.12)$$

depending only on the particle radius, a. Thus the Laplace transformed MSD, $\langle \Delta\tilde{r}^2(s)\rangle$, is related to the Laplace transformed shear relaxation modulus

$$\tilde{G}(s) = s\tilde{\eta}(s) = \frac{s}{6\pi a}\left[\frac{6k_BT}{s^2\langle\Delta\tilde{r}^2(s)\rangle} - ms\right], \qquad (2.13)$$

where $\tilde{G}(s)$ is the Laplace transform of the gradient of the relaxation modulus $G_r(t)$, also known as the relaxation spectrum. The ms term which represents particle inertia can be neglected at frequencies much less than the reciprocal of the velocity relaxation time of the particle. For typical microrheology experimental conditions, the frequency where particle inertia becomes relevant is on the order of MHz. By analytical continuation between the Fourier and Laplace domains, a simplified form can be written

in terms of the complex modulus:

$$G^*(\omega) = \frac{k_B T}{\mathbf{i}\omega\pi a} \frac{1}{\langle\Delta\hat{r}^2(\omega)\rangle}. \tag{2.14}$$

This is known to microrheologists as the generalised Stokes-Einstein relation (GSER) and is seminal in the study of diffusion to understand the mechanics of viscoelastic materials. Interpretation of the MSD is further aided by the equivalence of MSD and creep compliance in a step-stress experiment[113].

$$J(\tau) = \frac{\pi a}{k_B T}\langle\Delta r^2(\omega)\rangle. \tag{2.15}$$

Further work has examined the circumstances under which assumptions behind the GSER are valid, which is discussed in Section 2.2.4.

The analyses above were first applied to Diffusing Wave Spectroscopy[112], a microrheological technique where the autocorrelation of multiply scattered light probes the MSD of an ensemble of probe particles. Mason later extended the analyses to particle tracking microrheology[114], measuring displacements of a probe particle via forward-scattered laser light. Later, particle tracking microrheology using widefield microscopy was demonstrated with video cameras. Modern cameras make this trivial with high speeds, high resolutions, high bit-depths and dynamic ranges, and digital data streamed directly to a PC for storage or analysis.

Figure 2.4 demonstrates optical trapping video microrheology of water using an optically trapped polystyrene microsphere (typical image shown inset to d). The strong intensity gradient near the focus confines the diffusion of the bead ensuring the bead remains in the field of view and allowing it to be recorded over many minutes. Optical trapping is commonly used in microrheology when looking at solutions or weak gels where the bead would otherwise diffuse out of the field of view before sufficient data is

recorded[115]. Measurements of 200,000 images each were taken on the same bead using increasing laser powers to increase the trap stiffness $\kappa = 0.12\text{pN}/\mu\text{m}$, $0.51\text{pN}/\mu\text{m}$, and $1.4\text{pN}/\mu\text{m}$ for black, blue and red respectively. At short times (shown in b) the bead diffuses freely, unaffected by the trap, and Brownian motion is observed giving MSD $\propto D\tau$ in c) and $G'' \gg G'$ in d). At times much greater than the trap relaxation time (shown in c), the bead is confined within the trap and subdiffuse motion is observed, giving constant MSD $\propto \kappa^{-1}$ and $G'' \ll G''$. More detail on the data processing shown is in Chapter 3.
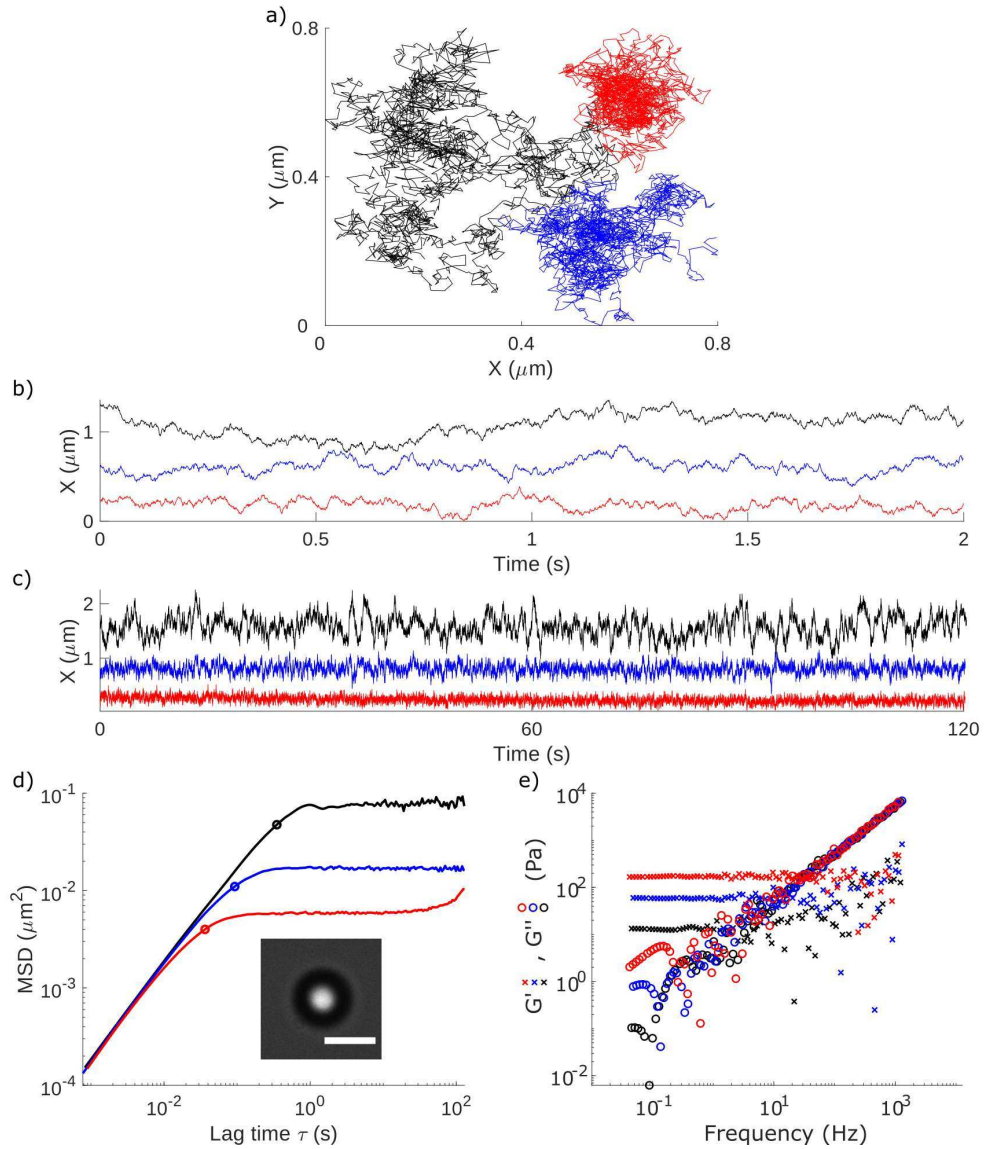
Figure 2.4: a) X and Y Position over 2 seconds of a 5μm diameter bead in water is recorded via video microscopy as described in Chapter 3. Typical image of bead shown inset to d with 10 µm scale bar. Trap stiffness was varied by adjusting laser power, resulting in $\kappa = 0.12$pN/μm, 0.51pN/μm, and 1.4pN/μm for black, blue and red respectively. At short lag times, visible in b), the bead is free to diffuse while at longer lag times, visible in c), the bead diffusion is limited by the trap. c) Corresponding mean-squared displacements with the trap relaxation times circled (Equation 3.4). d) Elastic and viscous moduli (crosses and circles, respectively) calculated using Equation 2.14.
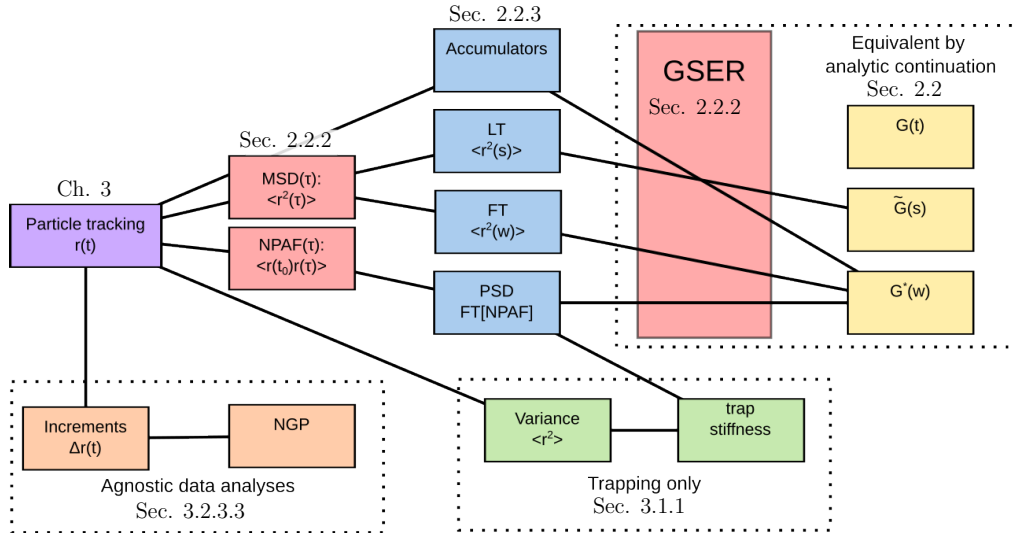
Figure 2.5: Flowchart of data analysis methods to understand experimental (position-time) data. Boxes are coloured according to which section of thesis they relate to: particle tracking and associated errors (purple); analysis methods relying on the GSER (blue); particle tracking statistics and the GSER itself (red); equivalent forms of mechanical moduli (yellow); agnostic data analyses (orange); analyses for trapping only (green).

2.2.3   Numerical Methods

Figure 2.5 summarises approaches used described within the text to use particle tracking data in order to understand the particle's motion. These are primarily to quantify the viscoelasticity of the material being probed. The methods to quantify trap stiffness in optical trapping can be generalised to any elastic confinement. Agnostic data analyses fall outside of the generalised Stokes-Einstein relation, where particle motion may not be indicative of the viscoelasticity.

The numerical inversion of time-domain particle tracking data to the frequency domain is, in general, non-trivial. This is because the Fourier transform integral,

$$\langle \Delta \hat{r}^2(\omega) \rangle = \int_{-\infty}^{\infty} \langle \Delta r^2(\tau) \rangle e^{\mathbf{i}\omega\tau} d\tau, \tag{2.16}$$

does not converge as the MSD $\langle \Delta r^2(\tau) \rangle$ does not tend to zero at long times.

There are several methods to overcome this which I have implemented and compared however the following method produces the lowest errors over a wide range of frequencies[116].

Evans et. al.[109] developed a technique to perform the inversion with minimal numerical errors by considering the experimental MSD as a piecewise function consisting of the discrete observations connected by linear sections. Thus the gradient of the MSD is a discontinuous series of piecewise functions, and the second derivative of the MSD is a series of delta functions. By analytically finding the Fourier transform of this series of delta functions, Evans arrives at the following: for a function g_k discretely sampled at times t_k for $k = 1, ...N$, the Fourier transform $\hat{g}(\omega)$ obeys

$$
\begin{aligned}
-\omega^2 \hat{g}(\omega) = & \mathbf{i}\omega g(0) + (1 - e^{-\mathbf{i}\omega t_1})\frac{g_1 - g(0)}{t_1} + g_\infty e^{-\mathbf{i}\omega t_N} \\
& \sum_{k=2}^{N} (\frac{g_k - g_{k-1}}{t_k - t_{k-1}})(e^{-\mathbf{i}\omega t_{k-1}} - e^{-\mathbf{i}\omega t_k}),
\end{aligned}
\tag{2.17}
$$

where $g(0)$ is the value of g extrapolated to $t = 0$ from above, and g_infty is the gradient of g extrapolated to infinite time. More details of my implementation of the rheological Fourier transform are in Section 3.3.3, including considerations of data processing to improve SNR. In implementing Equation 2.17, the recommendations of Tassieri et. al.[117] were followed including data interpolation.

There exist other methods for performing the above numerical inversion[118]. Particularly noteworthy is Yanagishima's[119] real-time method for calculating rheological moduli during particle tracking experiments. Other methods, however, give higher errors on the resulting viscoelastic modulus[116].

2.2.4 Mechanics Beyond LVE and GSER

So far, discussion has considered situations where the sample viscoelastic properties probed by microrheology are the same as would be probed by bulk rheology. The systems have been assumed to be ergodic, meaning an average over an ensemble of particles will yield the same result as an average for one particle over a span of time. This is the case for simple fluids such as water or glycerol, but not for colloidal systems such as found inside living cells and tissues[120].

In many colloidal systems, a characteristic length scale known as the mesh size can be defined or empirically determined. The diffusion of a particle then depends on its size relative to the mesh size. A larger particle will probe the colloidal ensemble in the same way bulk rheology would, while a smaller particle will undergo caged diffusion, probing the viscosity of the interstitial fluid. In such cases, the asymptotic behaviours of the system can be described as nanoscale and microscale viscosities[96]. The nanoscale viscosity will determine the diffusive transport of small molecules within the cell, while the diffusion of macromolecules as well as stress relaxation in the cytoplasm depend on the microscale viscosity.

Consider now a single probe particle suspended within a model complex fluid, consisting of an elastic network embedded in an incompressible viscous fluid. This is the poroelastic model for cells, in which we consider the stress both within the elastic network and the viscous suspension medium. The response function (displacement for a given applied force) of the probe particle provides insights into what microrheology is probing[121]. Within this model several effects cause one particle microrheology measurements to depart from bulk rheology[121–124].
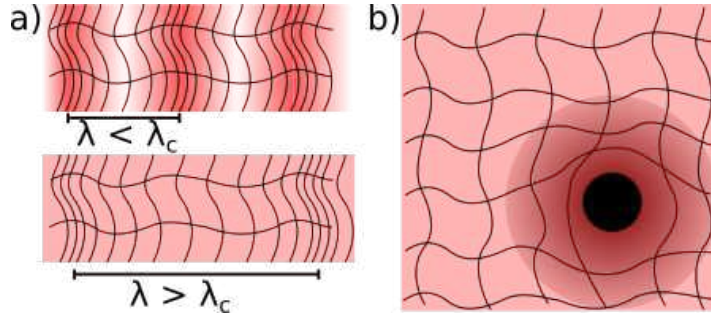
Figure 2.6: Poroelastic model in which the one particle microrheology response function differs from the shear modulus probed by bulk rheology. a) At frequencies above a cut-off, ω_c, or equivalently for strain wavelengths below a cut-off λ_c, viscous stress (red) remains within the interstitial fluid when the complex fluid undergoes deformation. At frequencies below the cut-off, the fluid drains through the network and the viscous stress is uniform. b) Perturbations to fluid (shown as darker colour) by probe particle, causing radial concentration gradient of elastic elements. Figures made to demonstrate key findings from [121, 122].

At low frequencies the model exhibits a lock-in, or cut-off, frequency (termed ω_c), below which the fluid can drain freely while the elastic network undergoes longitudinal deformations. See Figure 2.6a for visualisation. Thus, at low frequencies, microrheology probes the longitudinal modes of the elastic network. At intermediate frequencies the GSER is found to hold true only if the bead size is much larger than the mesh size of the elastic network, and at high frequencies fluid inertial effects influence the response of the bead. For a 1μm bead in a 2 mg/ml actin solution, the intermediate frequency range is 1 MHz $> \omega > 10$ Hz[124].

Furthermore, the presence of probe particles causes local perturbations to the complex fluid[125]. The elastic network is displaced, leading to a concentration gradient in the milieu of the probe particle (shown in Figure 2.6b). Surface chemistry of both the probe particle and the elastic network will affect the perturbation and hence the Brownian motion of the probe. Hence, one-particle microrheology only probes the perturbed fluid, not the "bulk phase"; and changing the probe coating will give different apparent

mechanical properties. Studying the correlation between displacements of nearby particles overcomes the local perturbations and inherent inhomogeneities, hence achieving better agreement with the bulk mechanical properties of complex fluids [125, 126].

2.2.5   Cell Rheology

Considering how the response function for a single particle is affected by both the mesh size and "free draining" modes, the length and time scale over which a measurement probes cell mechanics can be seen to affect the result. High strains (more than a few percent) such as found in deformability flow cytometry and magnetic bead microrheometry, cause cell fluidisation[64]. Thus these techniques are expected to report cells being softer than if they were measured with techniques such as external passive microrheology or intracellular microrheology.

In addition to fluidisation, live adherent cells exhibit aging effects known as rejuvenation whereby cell stiffness is reduced after deformation and recovers slowly following a power-law behaviour[64, 90]. Time-evolving mechanical properties leads to non-ergodicity, meaning a particle tracking experiment considering the ensemble average will yield different results to one considering the time average of a single particle[120]. The strain fluctuations present in living cells may also cause the system to be non-ergodic, and the implications for this in the measurements made are discussed in Chapters 4 and 5.

2.3 Light Scattering

Light scattering is an interaction between light and matter which changes the direction of the propagating light, broadly categorised as either elastic or inelastic. In this thesis, elastic light scattering is used to apply forces in optical trapping (Chapters 3 and 4), enabling microrheology measurements of G^* in water and of live cells. Inelastic scattering is used to probe acoustic fields in phonon microscopy (Chapter 5), allowing measurements of M' in live cells.

Elastic scattering does not change the wavelength of the scattered light (except possible Doppler shift for moving scatterers). Two types of elastic light scattering are particularly important for optical trapping, namely Rayleigh and Mie scattering[127]. These are explained in Section 2.3.1.

To contrast, inelastic light scattering is an interaction where both the direction and wavelength of the incident light may change. Two inelastic light scattering techniques used for study of biological specimens are Raman scattering and Brillouin (or Brillouin-Mandelstam) scattering which are explained in Section 2.3.2.

2.3.1 Elastic Scattering

Rayleigh scattering arises when light interacts with a dielectric particle much smaller than the optical wavelength. Considering a dielectric sphere such a polystyrene microsphere, Rayleigh scattering arises from the dipole induced within the particle by the incident electric field[128]. The scattered field intensity as a function of angle and distance to particle, $I_s(\theta, R)$ can

be calculated as

$$I_s(\theta, R) = I_0 \frac{1 + \cos^2 \theta}{2R^2} \left(\frac{2\pi}{\lambda}\right)^4 \left(\frac{m^2 - 1}{m^2 + 2}\right)^2 a^6, \qquad (2.18)$$

where $m = {n_p}/{n_m}$ is the ratio of refractive index of the particle to that of the medium, a is the radius of the particle, and λ the optical wavelength.

Mie scattering, on the other hand, applies to particles with sizes comparable to the wavelength, and has a scattering spectrum determined by the particle size and dielectric properties[128]. Calculation of Mie scattering is beyond the scope of this thesis, however its application is essential to optical trapping of micron-sized spheres. Considering polystyrene spheres illuminated by a monochromatic source, the angular dependence of the scattered light depends on the ratio ${2\pi d}/{\lambda}$, with larger particles scattering a greater proportion of the light in the forward direction, leading to weaker scattering forces.

2.3.1.1 Optical Trapping

The gradient force optical trap was first proposed by Arthur Ashkin in 1986[129] while researching radiation forces on the micro-scale. Hereafter when I refer to an optical trap, I mean gradient force optical trap unless otherwise stated. Optical trapping has found extensive applications in life sciences and microrheology, for example as a force transducer[8, 127, 130] and to control the position of cells or particles[131–133]. When characterising weak gels or viscous fluids, optical trapping prevents the probe particle from diffusing out of the field of view, allowing faster and longer measurements[115].

An optical trap can be as simple as a tightly focussed laser beam. In mi-

croscopy this is commonly achieved using a high numerical aperture (NA) objective lens, and a continuous wave laser beam collimated at the back focal plane. Overfilling the back focal plane increases the laser power incident at high spatial frequencies which increases the trapping efficiency. To achieve the high NA needed, water or oil immersion objectives are commonplace. A detailed description of how a focussed laser beam exerts a force is in Section 2.3.1.2

In optical trapping, laser powers from a few milliwatts up to hundreds of milliwatts at the sample[134] may be used. The powers used in Chapter 4 are typically less than thirty milliwatts, and exposure to cells is minimal because the trapping laser is turned off for most of the experiment. Despite this, it is worth considering damage to the cells under study. When studying delicate biological systems, damage to the sample is avoided by reduction of laser power and careful selection of wavelength, using a "therapeutic window of transparency" in the near-infrared ($\sim$700 nm - 1200 nm)[127], between absorption bands from proteins in the visible range and from water in the far infra-red. Thus using Nd:YAG trapping lasers at 1064 nm (as I do here) is a common way to avoid unnecessary heating or damage to one's sample, and it has previously been shown that optically trapping T-cells with tens of milliwatts of laser power at 1064 nm for up to an hour has no significant effect on their viability[133].

2.3.1.2 Optical Trapping Forces

The forces applied in optical trapping are generally described as a gradient force and a scattering force, and while these can be rigourously calculated for special cases such as the Rayleigh scattering regime or for weakly focussed beams (beam waist $w_0 \gg \lambda$), they are in general difficult to derive

for micron-sized particles in a tightly focussed beam[127, 135]. Here I will introduce approximations for the trapping forces in the Rayleigh regime, neglecting a full derivation or application of Mie scattering theory as it is beyond the scope of the thesis. The Rayleigh regime is quantitively different to the Mie regime, however gradient and scattering forces arise in both so individual trapped particles behave in a qualitatively similar manner for either regime.

The gradient force arises from the effect of an electric field on the induced dipole of the trapped particle. In the general case of a point dipole within an electromagnetic field, the instantaneous force can be written as

$$\vec{F} = (\vec{p} \cdot \nabla) \vec{E} + \dot{\vec{p}} \times \vec{B} + \dot{\vec{r}} \times (\vec{p} \cdot \nabla) \vec{B}, \qquad (2.19)$$

where $\vec{p}$ is the dipole moment, ∇ the gradient operator. Here the electric $(\vec{E})$ and magnetic $(\vec{B})$ fields are assumed to be unperturbed by the particle. The first and last terms of Equation 2.19 account for the spatial inhomogeneity of the electric field while the second term comes from the magnetic Lorentz force.

Clearly the total force depends strongly on the spatial distribution of the electromagnetic field, and in the case of a weakly focussed Gaussian beam (such that the zeroth order paraxial Gaussian beam approximation is valid) the gradient force for a small displacement of the particle in the $+x$ direction can be written as[135]

$$\vec{F}_g = -\hat{x} \frac{2\pi n_m a^3}{c} \left(\frac{m^2 - 1}{m^2 + 2} \right) \frac{4 \left(x/w_0^2 \right)}{1 + 4 \left(z/w_0 \right)^2}$$
$$\left(\frac{P}{\pi w_0^2} \right) \frac{1}{1 + 4 \left(z/w_0 \right)^2} \exp \left[\frac{2x^2}{w_0^2 + 4z^2} \right], \qquad (2.20)$$

which (for small displacements) scales linearly with the beam power P and

distance from trap centre x. Here n_m and n_p are the refractive indices of the medium and particle, m is the ratio $= {}^{n_p}\!/_{n_m}$, a is the particle radius, w_0 is the beam waist, and x and z are the radial and axial co-ordinates respectively.

Note that the direction of the gradient force is opposite to that of the displacement, enabling us to draw analogy to a Hookean spring, or ideal elastic element. Writing the stiffness $\kappa = {}^{\partial F_g}\!/_{\partial x}\big|_{x=0}$, the complex modulus for an optically trapped bead in water can be written simply as

$$G^*(\omega) = {}^{\kappa}\!/_{6\pi a} + \mathbf{i}6\pi a\eta_w\omega, \tag{2.21}$$

where a is the bead radius and η_w is the dynamic viscosity of water. Note that this is the same as the Kelvin-Voigt model solid in Equation 2.8 with $G' = {}^{\kappa}\!/_{6\pi a}$ and $G'' = 6\pi a\eta_w\omega$.

The scattering force for the same particle can also be derived, and takes the form

$$\vec{F}_s = \hat{z}\frac{n_m}{c}\frac{8}{3}\pi k^4 a^6 \left(\frac{m^2 - 1}{m^2 + 2}\right)^2$$
$$\left(\frac{2P}{\pi w_0^2}\right) \frac{1}{1 + 4\left({}^{z}\!/_{w_0{}^2}\right)} \exp\left[\frac{2x^2}{w_0^2 + 4z^2}\right], \tag{2.22}$$

where I have introduced the wavenumber $k = {}^{n_m\omega}\!/_c$.

To form a stable optical trap, the gradient force must be dominant, exceeding both the scattering force and the thermal energy of the particle ($\sim k_BT$). To aid in assessing this, it is helpful to consider the potential well that arises from the gradient force which can be written

$$U_g = \frac{2\pi n_m a^3}{c}\left(\frac{m^2 - 1}{m^2 + 2}\right)\frac{P}{\pi w_0{}^2}, \tag{2.23}$$

using beam power P, refractive indices n_m and n_p of the medium and particle, m is the ratio $= n_p/n_m$, a is the particle radius and w_0 is the beam waist.

In practical terms, the stability of the trap is ensured by using a tightly focussed beam from a high numerical aperture objective lens to create a strong gradient force in the z direction such that $F_{s,z} < F_{g,z}$. The approximations used to derive the prior equations thus do not strictly hold true as the approximations assume a meak focus. They do, however, serve to demonstrate how optical trapping forces arise and what is required for a stable optical trap.

2.3.2 Inelastic Scattering

Inelastic scattering may be used to probe high frequency vibrations within biological samples. In Brillouin scattering, acoustic phonons typically at GHz frequencies can be used to measure the longitudinal modulus of a sample. Raman scattering probes optical phonons with THz frequencies to determine the chemical composition of a sample. In each, photons of light interact with phonons in the sample and may be re-radiated with longer wavelength (Stokes' shift) or shorter (anti-Stokes' shift). The frequency shift of the scattered light is commonly analysed using a spectrometer.

The first experimental observations were published by Brillouin in 1922[136] and Mandelstam in 1926[137]. Acoustic phonons, the result of inhomogeneities (e.g. density fluctuations) within a material, may be of thermal origin (i.e. spontaneous Brillouin scattering), or generated in a coherent manner such as in Phonon microscopy or stimulated Brillouin scattering.

Raman scattering is the result of the interaction between photons and

the internal vibrations of a molecule[138]. The first published experimental measurements of Raman scattering were by Raman and Krishnan in 1928[139], although Landsberg and Mandelstam also published measurements of the same in 1928[140] along with a more complete theoretical explanation for their measurements. Thus while Raman was awarded the Nobel Prize in 1930, the technique was commonly referred to as "combinatory scattering" within the Soviet Union[138].

2.3.2.1   Brillouin Scattering

Consider a photon incident upon a phonon, whilst maintaining generality in 2D as shown in Figure 2.7a. The phonon acts like a Bragg grating (via the photo-elastic effect); that is to say a periodic variation in the optical properties which gives strong reflectance at certain angles via constructive interference. For incident photon wavelength λ_{k1} and material refractive index n, the Bragg reflection condition requires incident phonon wavelengths λ_{q1} which satisfy

$$2\lambda_{q1} \cos\left(\frac{\theta}{2}\right) = \frac{\lambda_{k1}}{n},$$ (2.24)

where $\frac{\theta}{2}$ is the incidence angle, or half the angle between the incident and scattered photon wavevectors. The cosine term arises from the geometry of the incident wavevectors (shown in Figure 2.7a).

An inelastic scattering event gives rise to either a Stokes shift in the case of the photon losing momentum to a phonon or an anti-Stokes shift in the case of a photon gaining momentum from a phonon. For Stokes scattered light, the wavevectors may be drawn as in Figure 2.7. Consider first the wavevectors of the two interacting particles, followed by the frequency shift
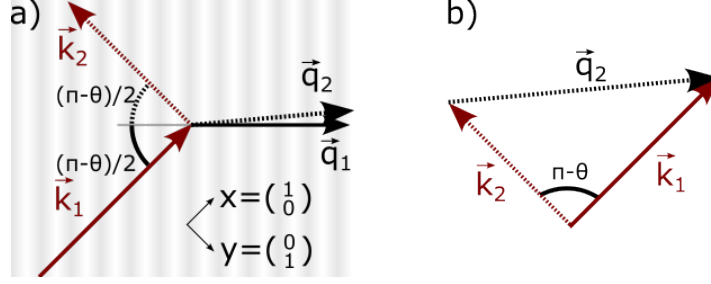
Figure 2.7: Geometry (a) and momentum conservation (b) of a density wave (phonon) Stokes scattering a photon (red). Incident wavevectors are shown as solid lines, and scattered wavevectors are shown as dotted lines. Basis vectors used in the text are defined in (a), thus a wavevector with wavenumber $|k|$ at an arbitrary angle ϕ from the incident photon can be written $\left(\begin{smallmatrix} \cos\phi \\ \sin\phi \end{smallmatrix} \right) |k|$.

and conservation of momentum. The incident photon wavevectors are

$$\vec{k_1} = \left(\begin{smallmatrix} 1 \\ 0 \end{smallmatrix} \right) \frac{2\pi}{\lambda_{k1}}, \tag{2.25}$$

$$\vec{q_1} = \left(\begin{smallmatrix} \cos\left(\frac{\theta}{2}\right) \\ \sin\left(\frac{\theta}{2}\right) \end{smallmatrix} \right) \frac{2\pi}{\lambda_{q1}} = \left(\begin{smallmatrix} 1 \\ \tan\left(\frac{\theta}{2}\right) \end{smallmatrix} \right) \frac{2\pi}{\lambda_{k1}}, \tag{2.26}$$

where the final equality demonstrates that the x component of the incident phonon wavevector is equal to that of the incident photon wavevector. The relations written thus far can be derived from simple geometric arguments when considering Figure 2.7a.

The frequency shift of the scattered photon (relative to the incident photon) is given by the phonon frequency

$$\nu_B = \frac{V}{\lambda_{q1}} = \frac{2n \cos\left(\frac{\theta}{2}\right)}{\lambda_1} \sqrt{\frac{M'}{\rho}}, \tag{2.27}$$

where V is the speed of sound, determined by square root of the ratio of the longitudinal elastic modulus, M' (see Figure 2.2e), to the density, ρ, of the material. Across the second equality I have substituted the phonon wavelength for the incident photon (vacuum) wavelength and refractive index n using Equation 2.24. Note that the scattered and incident optical

44

wavelengths, respectively, are related by

$$\lambda_{k2} = \lambda_{k1} \pm \frac{c}{\nu_B}, \tag{2.28}$$

so to a first-order approximation $\lambda_{k2} = \lambda_{k1}$ as $\nu_B \ll \frac{c}{\lambda_{k1}}$ (GHz shifts applied to THz optical frequencies). Here the $\pm$ arises from the possibility of Stokes or anti-Stokes scattering events.

A key difference between phonon microscopy (and other time-resolved Brillouin scattering techniques, discussed later in Section 5.2.2) and stimulated Brillouin scattering (and most Brillouin scattering techniques) is the acoustic wavenumber probed. For spontaneous Brillouin the acoustic wavenumber is half the optical wavenumber (Equation 2.24). This is not the case for phonon microscopy as the acoustic pulse generated is much shorter ($\sim$80 nm) than the optical wavelength (780 nm), and the scattering interaction is dominated by the higher wavenumber Fourier components. Because the interaction length, l_a, is shorter than the acoustic wavelength PLU-based techniques theoretically probe optoacoustic properties with higher axial resolution than a spontaneous Brillouin scattering experiment. In practice, signal processing limits the axial resolution of phonon microscopy to $\sim$780 nm, while the optical point-spread function limits spontaneous Brillouin microscopy to $\sim$2 µm.

2.4   Context of this work

Decades of study into mechanobiology have revealed that both the elastic properties of cells, and the forces they generate bear studying in order to understand behaviour of single cells. Techniques such as magnetic twisting cytometry and magnetic bead microrheometry exist which can probe the

complex shear modulus of single cells, and the strain due to forces generated within the cell[64, 141], however they cannot make these measurements simultaneously. Additionally these active techniques cause fluidisation and rejuvenation which lead changes in the cell mecahanical properties. Passive techniques such as endogenous tracer microrheology or ballistic injection nanorheology can measure the shear modulus, but are either non-specific or invasive.

Studies using beads adhered to cells using liands which target different receptors, such as integrin or scavenger receptors, have shown that the apparent shear modulus of cells depends on the adhesion target[44]. Despite this, few techniques have studied the time evolution of the mechanics of the binding site, instead choosing to allow cells to reach an equilibrium before starting measurements[50, 64, 69, 90].

In Chapter 4 I demonstrate that by using optical trapping to control the location on the cell surface that a microsphere is bound, and high spatiotemporal resolution video microscopy to perform particle tracking, external passive microrheology can simultaneously determine both the complex shear modulus and the stress generation of individual live cells. This is applied to probe the initial stages of focal adhesion formation after a functionalised bead is bound to the surface ofa cell.

It is revealed that while the strain rate decreases over time (which could have been observed using prior techniques), the stress rate actually increases. Such an experiment would not be possible with other techniques as they are unable to simultaneously measure the elastic modulus and active stress generation of cells. Furthermore, application of external forces would perturb the mechanical properties of the binding site and possibly alter the cell's physiological response to the bead.

Ultrasound has found clinical applications for decades, however the resolution is limited by the frequencies (and hence acoustic wavelengths) that piezo transducers can probe. Brillouin light scattering offers a way to probe gigahertz acoustic waves and biological applications are developing fast, with different techniques suited to different applications. Phonon microscopy offers better axial resolution than other Brillouin scattering techniques due to the short axial length of the coherent acoustic pulse. Previous studies using phonon microscopy have, however, demonstrated limited biocompatibility due to use of ultraviolet pump lasers[2].

Many biomechanical techniques, such as microrheology, may take many seconds to make each measurement; this limits the temporal resolution and hence the rate at which changes to a system can be resolved. While cytoskeletal structure has been studied in cells using fluorescence and mechanical techniques, the changing mechanical properties of single cells has not been resolved during treatment with cytoskeletal targetting drugs. In Chapter 5 I demonstrate phonon microscopy measurements of actin disruption in live cells, reporting the first time-course measurement of single cells' mechanical properties during this process by any technique. Using the superior axial resolution of phonon microscopy compared to other Brillouin and acoustic techniques, the longitudinal modulus of the basal actin cortex is studied and found to not change significantly compared to that of the cytoplasm.

Chapter 3

Microrheology Methods Development

In this chapter, I will detail the practical aspects of my work on microrheology. Much of what is introduced in this chapter will be applied in Chapter 4, in which I demonstrate microrheology measurements of live cells. This will include the experimental setup, both the hardware I used and the software I used and developed. It will also cover the post-processing which I applied to my data, and present experimental results to demonstrate both the capabilities of the system and points of consideration for a microrheologist. Relevant errors are discussed including particle tracking errors and numerical errors and how these affect quantities calculated in microrheology.

Data analyses presented have been implemented in MATLAB and are openly available via a GitHub repository[142]. The rationale guiding this software design can be summarised by two main goals: suitability for exploratory data analysis, and for creation of pipelines for reproducible processing of multiple data sets. The former is to allow examination of data

with minimal preconceptions or expectations for what one will find, while the latter means that once one knows what is probed by given data set, the analysis can be reapplied to many similar datasets such as different experimental samples.

To achieve these two goals, two characteristics were implemented as far as possible: modularity and generalisability of analysis – many different functions which act on the same data structures to homogenise the data analysis experience while reusing code as much as possible; and optimised analysis code – reduce execution times allowing rapid prototyping and exploratory data analysis.

3.1 Background

3.1.1 Measuring Trap Stiffness

When a particle is close to the trap centre, the optical trap acts as a simple, or Hookean, spring. Equivalently it could be called a linear elastic element due to the force applied to the trapped particle,

$$\vec{F}_{trap} = -r_i \kappa_i \hat{e}_i \quad \forall \, i \in \{x, y, z\}, \tag{3.1}$$

being linear with respect to r_i, the displacement from trap centre in the i direction, and κ_i, the trap stiffness in a given direction, where $\hat{e}_i$ is the unit vector in the i direction. Subscripts indicate the total trapping force is a vector summed over all three spatial dimensions. This linear relation makes optical traps ideal force transducers on the nanoscale.

Application of calibrated forces first requires calibration of trap stiffness.

There are several different methods for calibrating trap stiffness, however only one is sample-independent: by appealing to the principle of equipartition of energy, it can be shown that a particle diffusing within the trap will have position variance[115]

$$\frac{1}{2}\left\langle r_i^2\right\rangle\kappa_i=\frac{1}{2}k_BT,\qquad(3.2)$$

where $\frac{1}{2}k_BT$, Boltzmann's constant times absolute temperature, is the thermal energy per degree of freedom and κ is the trap stiffness defined above. This method is commonly used and requires only the ability to trap and track a particle. The sample-independent nature has lead to it being adopted as a calibration step for some active microrheology experiments[143, 144]. The equipartition method is subject to systematic errors as explained in Section 3.3.1, which limits the maximum trap stiffness to which it can be applied.

One alternative method is the drag force method, in which either the sample is moved relative to a stationary trap, or the trap is moved relative to a stationary sample. The displacement from the trap centre ($\vec{r}$) is measured, and for low velocities where the linear approximation is valid, the trapping force is calculated by[145]

$$\vec{F}_{trap}=\vec{F}_{drag}\quad\rightarrow\quad-\vec{\kappa}\vec{r}=-\vec{\nu}\beta=-6\pi a\eta\vec{\nu},\qquad(3.3)$$

where $\vec{\nu}$ is the velocity of the particle relative to the fluid, and $\beta=6\pi a\eta$ is the drag coefficient for a particle of radius a in a medium with dynamic viscosity η.

The drag force method has the principle flaw of the prerequisite knowledge of the medium viscosity and bead size. Secondly, when moving the medium,

inertial effects may mean that the local fluid velocity differs from the stage velocity[146]. Finally, if the medium is a complex fluid, the drag time must be longer than the longest relaxation time of the fluid otherwise the response will not be purely viscous. For these reasons, I do not use the drag force method to calibrate trap stiffness in the work presented herein.

One major advantage of the drag force method is that it can measure the total trapping force, i.e. the force required to escape the trap. A simple experiment to find this is to slowly increase the stage speed until the bead leaves the trap, and to note the speed at which this happens. The total trapping force is not the same as the trap stiffness because the trapping force is only linear with displacement for small displacements.

Another method for calibrating trap stiffness is to measure the characteristic relaxation time of the trap, or its reciprocal, the corner frequency. This method also requires the medium viscosity to be known. If the viscosity is unknown, the relaxation time and trap stiffness can be used to quantify the viscosity, as will be explained in Section 3.2.4.

3.1.2 Optical Trap as Ideal Viscoelastic Material

The system of an optical trap and a viscous fluid can be considered an ideal viscoelastic material. Consider that MSD, and thus also compliance, $J(t)$, monotonically increase for diffuse motion. Hence the longest relaxation time that can be probed using a static optical trap is determined by the time scale at which the trap elasticity dominates the probe motion. This is exemplified in Figure 3.1 where varying the trap stiffness affects only the plateau and the relaxation time, not the short-time diffuse behaviour.

If the suspension fluid can be approximated as Newtonian over the fre-
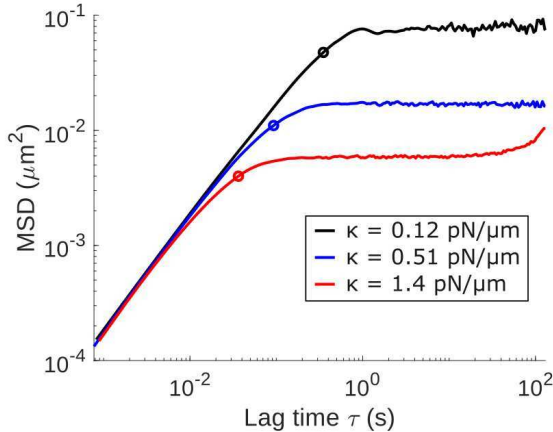
Figure 3.1: Example mean squared displacement for an optically trapped bead measured with three different trap stiffnesses. The short lag time behaviour of each is identical because it is determined solely by free diffusion of the bead. The plateau height decreases with increasing trap stiffness. Characteristic relaxation times are marked with circles.

quency range probed, the compliance can be modelled as a Kelvin-Voigt material (i.e.: the model viscoelastic material in Figure 2.3c). The characteristic relaxation time, t_c, is therefore the time at which the compliance of the trap equals the compliance of the fluid:

$$t_c = \frac{6\pi a \eta}{\kappa},\tag{3.4}$$

with η, the dynamic viscosity of the fluid, bead radius a, and trap stiffness κ. This relaxation time is also known as the corner time, hence the subscript. For 2.5 µm-radius sphere in water, held with trap stiffness $\kappa =0.1$ pN/µm, the trap relaxation sets the low-frequency limit of the bandwidth to 2 Hz.

Here I have neglected the Faxén's law correction to translational viscosity[145],

$$\eta_e = \frac{\eta}{1 - \frac{9}{16}\frac{a}{h} + \frac{1}{8}\frac{a}{h}^3 - \frac{45}{256}\frac{a}{h}^4 - \frac{1}{16}\frac{a}{h}^5}\tag{3.5}$$

which describes the change in effective viscosity, η_e, when the particle is at a

height h above a no-slip boundary (e.g. the coverslip). As a guide for when this is needed, the effective viscosity is 5% higher than the actual viscosity when the radius is one twelfth of the height. By performing all viscosity measurements with the trapped particle at least 12 radii (i.e. 60 µm) from the nearest surface, the Faxén's law correction is negligible.

3.2 Methods

3.2.1 Optical Setup

Optical trapping and microrheology measurements were performed on the same instrument, based around a Nikon Eclipse ti inverted microscope body with a brightfield illumination module fitted. The optics are shown in Figure 3.2. For optical trapping, a 3 W 1064 nm Nd:YAG laser is expanded to fill the working face of a spatial light modulator. The reflected light is then imaged via a periscope onto the back focal plane of the microscope. Overfilling the back focal plane of the microscope approximates uniform illumination at all spatial frequencies, creating the brightest focal spot and hence greatest trap stiffness for a given power. The high numerical aperture (NA) needed for optical trapping is provided by a Nikon Plan Fluor 100 x (1.30 NA) oil immersion objective lens.

Illumination for brightfield imaging was via a Nikon dia illumination unit containing both a halogen lamp and condenser optics housed above the sample plane, making it trivial to perform imaging with transmitted light. The condenser was set up in Köhler illumination to maximise contrast and hence minimize localisation, or static, error in microrheology experiments. Fluorescent imaging during microrheology and optical trapping
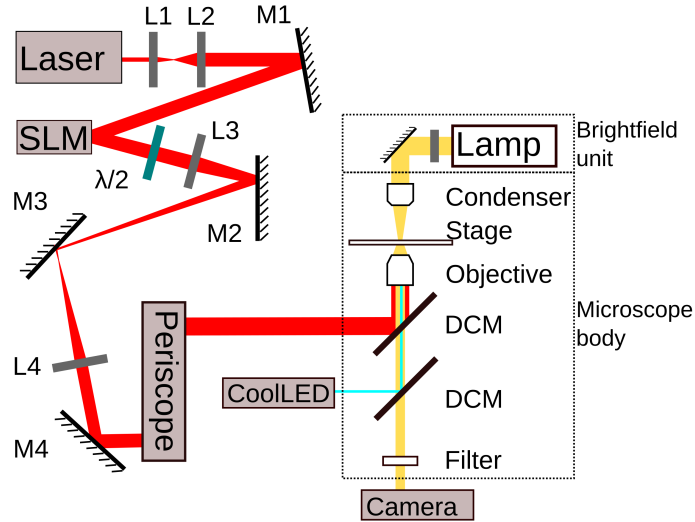
Figure 3.2: Optics diagram for optical trapping and microrheology measurements. L1/L2: Beam expander to overfill SLM. L3/L4: Telescope to image SLM onto back focal plane of objective. M1-4: Steering mirrors. SLM: Spatial light modulator. $\lambda/2$: Half-wave plate. LED: CoolLED fluorescence illumination unit. DCM: Dichroic mirror.

experiments used a CoolLED LED illumination unit and dichroic mirrors mounted within the microscope filter wheel.

For microrheology experiments, I adjusted beam collimation by removing lens L1 from the system. To do this, first the system was fully aligned using a pair of apertures to align each optical element, and then L1 was removed and the alignment of two steering mirrors (M4 and the second mirror in the periscope) was fine-tuned to produce a symmetric focal spot in the sample plane.

The divergent beam was coupled into the objective less efficiently, but the maximum power available at the sample was still more than enough for optical trapping. The advantage it brought was that the equilibrium position for a trapped bead was a couple of microns above the imaging plane, i.e.: the focal plane of the lens was not coincident with the centre of the bead. I attempted to move L1 axially to produce the same effect,
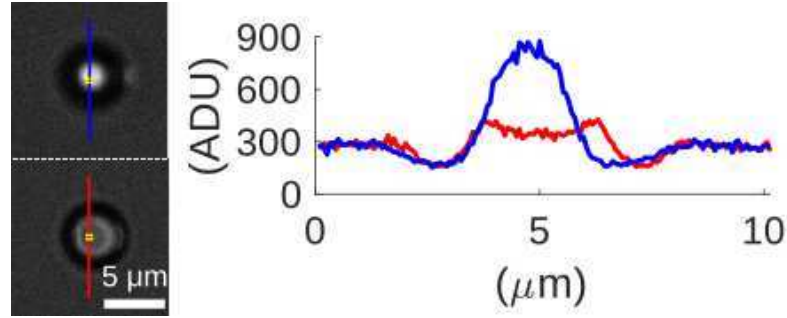
Figure 3.3: Images of bead trapped without (top, blue line) and with (bottom, red line) lens L1 in place, and line plots across the centre of the beads as indicated. The shift in the bead equilibrium position relative to the focal plane of the objective causes the bead image to change as seen.

but was not able to achieve the same image contrast while L1 was in the system.

The defocus, coupled with lensing effects from the bead, meant that the image of an optically trapped bead had a bright centre with a Gaussian profile as shown by the inset to Figure 3.3. This meant trapped beads could be tracked with ease using thresholding and a centroid algorithm (Equation 3.6). Otherwise the low contrast would increase static error as will be demonstrated in Section 3.3.1.

Microrheology experiments presented here used an OptiMOS sCMOS camera (QImaging, Canada). This sCMOS sensor has two features particularly well suited for microrheology. Firstly the pixel values are read out at 16-bit resolution, meaning they fall between 0 and 65,535 analogue-digital units (ADU). Secondly the acquisition frame rate can be increased by selecting a small region of interest (ROI) as shown in Figure 3.4, in which case only part of the full field of view image is collected. Higher frame rates increase the maximum frequency probed in microrheology as expected by Nyquist-Shannon sampling theory.

The optical system also includes a spatial light modulator (SLM) and half-
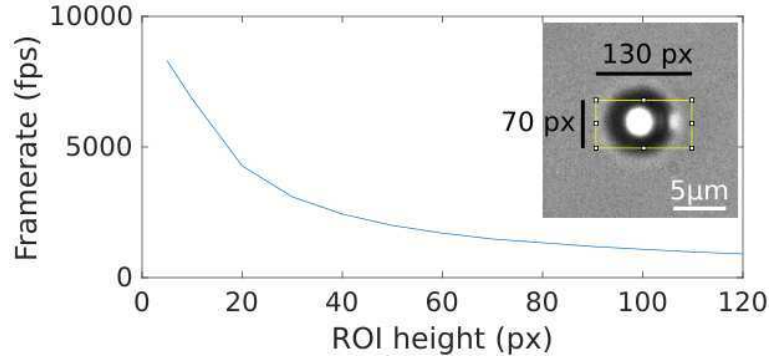
Figure 3.4: Acquisition frame rate for OptiMOS sCMOS camera depends on the number of rows in the ROI (e.g. rectangle selected in inset image of trapped bead) selected for acquisition. Faster acquisition can be achieved with a smaller ROI.

wave plate. These are present for experiments using holographic optical trapping, which was not performed in this thesis. I will explain it nonetheless for curiosity value: A hologram, analogous to a diffraction grating, is calculated and displayed on the SLM, which selectively retards the phase of the reflected light. The SLM pattern is imaged onto the back focal plane using lenses 3 and 4, and hence the Fourier transform of the SLM pattern is projected onto the sample plane. The half-wave plate allows rotation of the beam polarisation, supporting experiments which require a particular polarisation such as exciting nanoplasmonic structures.

3.2.2 Data Acquisition

To perform the particle tracking microrheology experiments reported here, I have developed an acquisition and processing script in Micro-Manager[147] using the built-in scripting interface and written in Beanshell, a language based on Java. The script, explained in Appendix A, handles control of the hardware, collecting images via a sequence acquisition on the camera. Position time data is saved to disk along with a small portion of the ROI images and two full field-of-view images (before and after the acquisition).

During the sequence acquisition, the camera runs on its own internal clock, so the time between each image is consistent and can be calculated using the time between the first and Nth images. This section describes the rationale behind this data acquisition methodology.

The first practical challenge of microrheology is the large amounts and rates of data that need handling: the OptiMOS sCMOS camera I used for microrheology experiments runs at up to 1500 frames per second with ROI dimensions of 200 pixels × 100 pixels and 16-bit depth. These parameters, typical for a single particle tracking experiment, generate 60 MB/s of image data; this is comparable to the maximum data write speed one can expect from a hard disk drive, assuming raw data is written to disk.

A short experiment may run for 5 minutes and result in 18 GB of image data, which is enough that (unless you write to disk while collecting the data) memory management is a challenge even for modern computers. Thus, a day of experiments may easily require hundreds of GBs of storage. Processing this data after the fact will require reading it back from the hard drive, substantially increasing the time required to perform said processing.

To overcome this, image data can be processed on-the-fly and only the result needs saving. In this case, the challenge is to process the image quickly enough not to create a backlog. In the scenario described above, each image must be processed in only 0.6 ms, thus limiting the complexity of any processing algorithms. The resultant data rate, around 6 kB/s, can easily be written to PC storage while the acquisition is running allowing arbitrarily long measurements to be performed.

Due to the nature of Beanshell as an interpreted language, steps such as indexing into arrays are slow; this led to me adapting the ImageJ source

code[148] for centroid calculations in Java:

$$C_x = \frac{\sum_{x=1}^{N_x} \sum_{y=1}^{N_y} (I_{xy} - T)x}{\sum_{x=1}^{N_x} \sum_{y=1}^{N_y} (I_{xy} - T)}, \tag{3.6}$$

with the X centroid C_x given by a sum of the pixel intensities, I_{xy}, after subtracting threshold value, T, weighted by their co-ordinates (x, y) across the width and height of the image N_x and N_y, respectively. Pixel values $I_{xy} < T$ are considered background and are not included in the centroid calculation. A second significant speed-up to the experimental workflow was to develop Java code for saving the output position-time data in binary formats. In both cases, the Java code is pre-compiled by installing it as an ImageJ plug-in, thus substantially reducing the processing time required.

3.2.3 Post-Processing

Data saved from experiments mostly consists of position-time data which is processed after the acquisition has concluded; the different processing steps and outcomes have been summarised in Figure 3.5 to help the reader understand how the different processing steps are related. Methods I have implemented include co-ordinate transforms, digital filters to de-noise, and calculation of the increment distributions. To elucidate mechanical compliance, the Mean-Squared Displacement (MSD) is calculated, and post-processing I have implemented for the MSD includes finding corner times, measuring pseudo-diffusion parameters, sample viscosity and trap stiffness, and numerical Fourier transforms to estimate viscoelastic moduli. With the exception of the MATLAB msdanalyzer class[149], all processing has been implemented in MATLAB by me, and all code (including my modifications to the msdanalyzer code) are available on GitHub[142] under the GNU GPL v3 license.
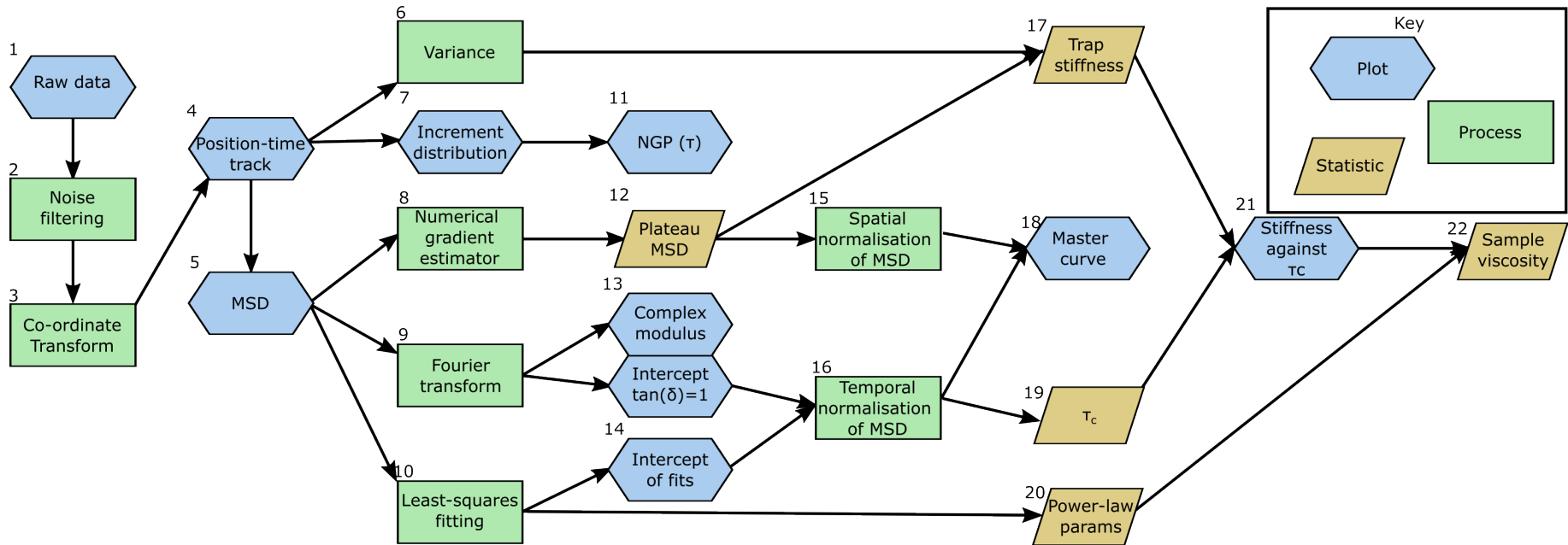
Figure 3.5: Flowchart to guide the reader through data processing implemented for microrheology analyses. Boxes are coloured according to the classification of the step. Raw data is acquired as described in Section 3.2.2. The processes from boxes 1 to 4, 4-5, 4-6-17 and 4-7-11 (NGP: non-Gaussian parameter, Equation 3.14) are described in Section 3.2.3. The flows through boxes 8-12-15-18, and 10-14-16-18/19, and using either power-law parameters (boxes 10 and 20) or stiffness and corner time τ_c (box 21) to measure viscosity is discussed in Section 3.2.4.1. The flow through boxes 9-13/14-16 is explained in Section 3.2.4.2. Box 18 can be seen as the inset to Figure 3.11a), while box 21 can be seen as the inset to Figure 3.11b)

3.2.3.1   Noise Filtering

Experimental noise is inevitable. Overhead lights introduce optical noise at frequencies determined by the harmonics of the mains electricity, and to avoid this experiments were performed in the dark. In a lab environment with many electrical devices, there is electronic noise which is less easy to isolate. For this reason, it is useful to be able to identify and remove noise from position-time data.

Several recurrent sources of noise were identified in position-time data, and a digital bandstop filter was used to remove this noise when handling position-time data in MATLAB. The filter was applied directly to the position-time data with up to three narrow-band ($<1\,$Hz) stop filters. Figure 3.6 shows the Fourier spectrum of a position-time trace obtained using the FFT algorithm. Clearly visible are noise peaks at 92, 124 and 151 Hz. The peaks at 93 and 124 Hz are inherent to all experiments on the optical trapping rig, suggesting they arise from an electrical device in the lab. The noise peak at 151 Hz is only present when the laser power supply is turned on.

After applying the bandstop filter, the Fourier spectrum can be seen to be broadly the same except for "gaps" at the stop band. The effect on the MSD is readily apparent in Figure 3.6b: the raw MSD is higher at all delay times and exhibits a characteristic "ripple" which is not present in the filtered MSD. The inset shows that the raw MSD is roughly $1.2\times$ greater than the filtered MSD.
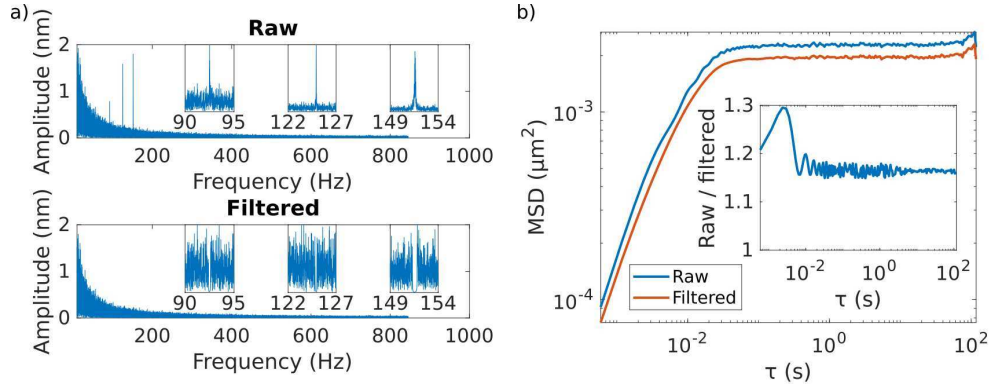
Figure 3.6: a) Fourier spectrum of trapped bead position, comparing raw and filtered spectra. Noise peaks visible in the raw spectrum at 92, 124 and 151 Hz have been removed by a bandstop filter. Insets show the spectra close to the peaks. b) MSD curves comparing raw and filtered. Note that in addition to the increase in MSD at all times, there is also a "ripple" effect at short times caused by the noise. Inset shows the ratio of raw to filtered MSD where the "ripple" is more prominent.

3.2.3.2   Co-ordinate Transforms

After de-noising, position-time data may be subjected to a co-ordinate transform. Two transforms were implemented for different purposes. For optical trapping data, a weaker trap allows broader bandwidth passive microrheology measurements. As laser alignment is never perfect, the trap strength is anisotropic leading to an elliptical position distribution. Position-time data may therefore be transformed to place the major axis of the position distribution (hence weak trap direction) along the X direction, giving the broadest measurement bandwidth possible.

To measure trap anisotropy, a histogram-based method was developed and tested using manually transformed experimental data. The transform used was to scale the Y data by a factor of 0.75 before rotating the data by $45°$ to simulate a highly anisotropic trap. The histogram-based method is as follows: first, the 2D position-time data is binned. Next, an ellipse is fitted to the 2D probability distribution using the MATLAB function
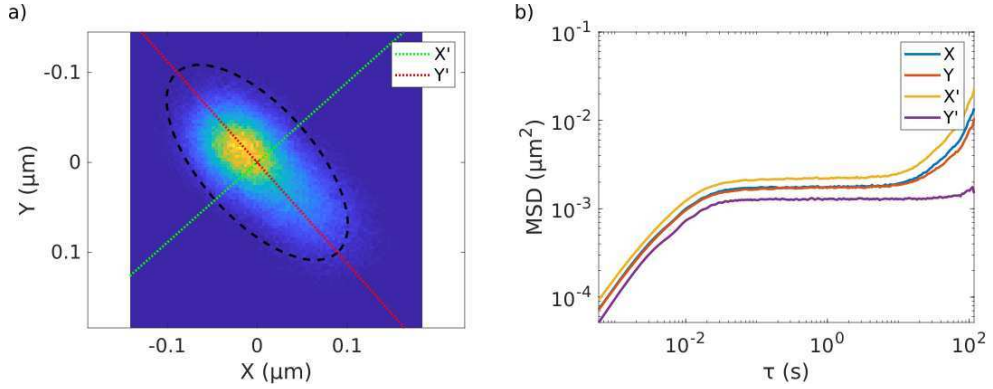
Figure 3.7: a) Heatmap of bead position for optically trapped bead in anisotropic trap. Fitted ellipse and major (X') and minor (Y') axes shown as dashed lines. b) MSD curves for original data (X and Y) and transformed data (X' and Y').

regionprops. Both steps are shown in Figure 3.7a where image colours map to bin counts and fitted ellipse is shown with transformed axes. Note that the shape of the distribution is more important than the centre - the centre of the ellipse need not be at the point where the probability density is highest. The orientation of the ellipse major axis relative to the X direction is extracted and finally, the data is transformed using

$$X' = X \cos(\theta) - Y \sin(\theta) \tag{3.7}$$

$$Y' = X \sin(\theta) + Y \cos(\theta) \tag{3.8}$$

where θ is the orientation of the major axis relative to the X direction. The transformed data is then used for further analyses such as calculating the MSD as shown in Figure 3.7b. Comparing the two, it can be seen that despite almost equal trap stiffnesses in X and Y, the trap stiffnesses are quite different in X' and Y'.

For data taken from beads affixed to cells, the direction normal to the cell surface (henceforth referred to as radial) encodes the mechanical information of the cell. Thus it is desirable to view the motion in radial and tangential directions, rather than X and Y. In the transformed co-ordinates, the

cell is modelled as a tall cylinder, such that vertical displacements (which are not measured but can sometimes be seen from before and after images) are independent of radial displacements. A more complete 3D model of the cell would require 3D imaging of each cell before microrheology measurements, and 3D particle tracking (e.g.: Matheson et. al.[150]). The model assumptions are discussed in detail in Chapter 4.

The transformation used is

$$(x, y) \rightarrow (r, r \cdot \theta) : \tag{3.9}$$

$$r = \sqrt{(\rho_x + C_x - R_x)^2 + (\rho_y + C_y - R_y)^2}, \tag{3.10}$$

$$\theta = \tan^{-1}\left(\frac{\rho_y + C_y - R_y}{\rho_x + C_x - R_x}\right). \tag{3.11}$$

where the tangential co-ordinate is $r \cdot \theta$ in order to have dimensions of length. This is shown schematically in Figure 3.8. The centroid calculation (Equation 3.6) uses co-ordinates within the ROI, denoted ρ_{xy}, which can be related to the co-ordinates of the full field of view image using the ROI position, R_{xy}, from the image metadata. Determining the cell position, C_{xy}, is somewhat more complicated. For many of the cells, there is sufficient contrast that a circle finding algorithm could be employed. Not all cells, however, are perfectly round. Instead, I visually inspected the images of the bead bound to the cell and drew a circle which approximates the edge of the cell where the bead contacts the cell.

3.2.3.3 Increment Distributions

A characteristic of Brownian motion is the increment series,

$$\Delta r(t)_\tau = r(t + \tau) - r(t), \tag{3.12}$$
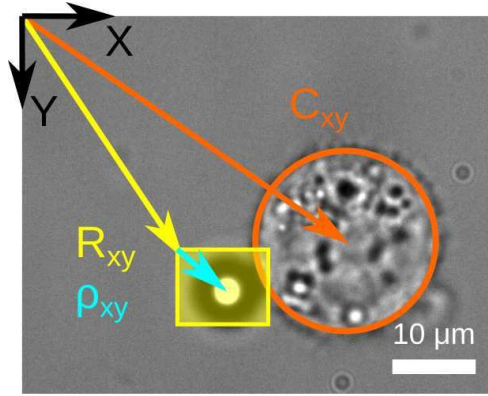
Figure 3.8: Geometry definitions used to convert from Cartesian co-ordinates to cylindrical polar (Equation 3.11). The ROI is shown in yellow, the co-ordinates saved during acquisition are shown in cyan, and the cell is circled in orange.

for a position-time series $r(t)$ and delay time τ. The increments are drawn from a normal distribution with mean 0, and autocorrelation given by a Dirac delta function $\langle \Delta r(t) \Delta r(t') \rangle = \delta(t - t')$.

To determine whether a given position-time series, $r(t)$, is driven by an equilibrium process or not, I first consider the normalised increment series,

$$z(t)_\tau = \frac{\Delta r(t)_\tau - \overline{\Delta r(t)_\tau}}{STD(\Delta r(t)_\tau)}, \tag{3.13}$$

with $\overline{\Delta r(t)_\tau}$ denoting the mean and $STD(\Delta r(t)_\tau)$ the standard deviation. An example normalised increment distribution from an optically trapped bead is shown in Figure 3.9a, along with a normal distribution. The experimental data shows good agreement with the normal distribution out to $|z| \simeq 4$. There are observations of larger increments, appearing as broad tails, but it is worth noting that the number of observations of each increment $|z| > 4$ is less than 10, compared to hundreds of thousands at $z = 0$.

I now consider the effects of static and dynamic error on the increment distributions. An example of each is also shown in Figure 3.9 (using the same

data as Figures 3.14 and 3.15), where the respective datasets are labelled "2350 ADU" and "100 ms". Both static and dynamic errors cause the central peak of the distribution to be sharper and the tails to be broader than the normal distribution. Notably, the static error causes a noisier increment distribution, while dynamic error affects the shape of the distribution without adding noise. Further discussion of these particle tracking errors can be found in Section 3.3.1.

To characterise the closeness of z to a normal distribution, I have used the non-Gaussian parameter introduced by Rahman[151] and since applied to studies of colloidal systems[152] and cytoskeletal rearrangements[90]. Rahman defined a series of parameters, however I have only used the second order parameter,

$$NGP(\tau) = \frac{\langle z_\tau{}^4 \rangle}{3\langle z_\tau{}^2 \rangle^2} - 1,\tag{3.14}$$

where $\langle z_\tau^4 \rangle = \sum_{z=-\infty}^{z=\infty} z^4 p(z)$ denotes the mean of the z^4 distribution and similarly for z_τ^2.

Now I will examine the statistics of diffusion and whether there are enough observations of a given delay time for the MSD to accurately represent the motion. Figure 3.9b shows the NGP as a function of lag time for increasing observation duration, T. Examining a given lag time (say $\tau = 10^{-3}$ s), it can be seen that for $T > 100\tau$, the NGP is close to 0 and hence the observation duration is adequate to say that the motion is Brownian on that time scale.

This has implications for determining observation duration in microrheology studies: if the experimenter wishes to measure the creep compliance, $J(t)$, at a given maximum time, they will need the experimental observation to be 100 times that time. In other words, if you wish to measure the stiffness of a gel at $t = 1$ s, an observation of 100 s is required to have good
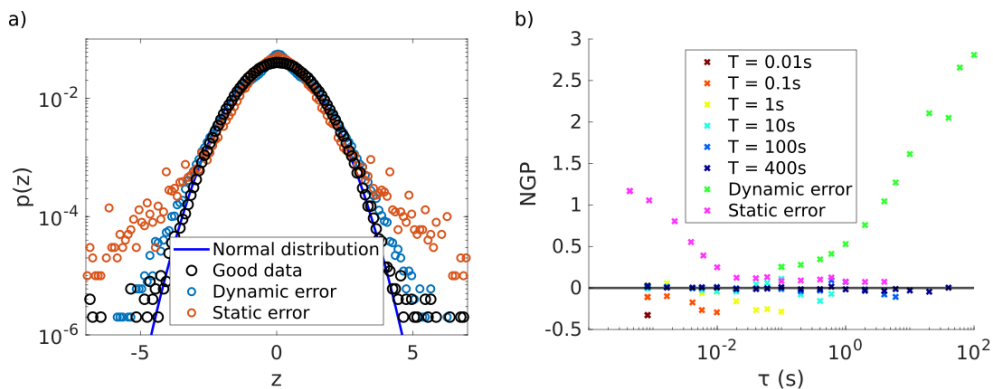
Figure 3.9: a) Increment distributions at the shortest delay time (around 1ms) for optically trapped beads in water, comparing "good" data with 400s of observations to data with extreme dynamic or static errors. A normal distribution is shown to guide the eye. b) NGP as a function of lag time showing the effects of observation duration, T, and tracking errors.

Gaussian statistics. This is considered in terms of random errors in Section 3.3.2.

Figure 3.9 also shows the effects of static and dynamic error on the non-Gaussian parameter. As may be expected, the static error only affects the NGP on timescales where the actual motion is less than the static error, i.e.: the shortest times where the apparent MSD exhibits an up-tick. Dynamic error, on the other hand, causes the increment distribution to depart from normality at all time scales, with increasing NGP at longer times.

3.2.3.4 MSD Calculation

Here is a short explanation of the code I use to calculate Mean-Squared Displacement (MSD, introduced in Section 2.2.2), which is defined as

$$MSD = \langle \Delta r^2(\tau) \rangle = \langle (r(t) - r(t + \tau))^2 \rangle_t = 2nD\tau. \qquad (3.15)$$

Post-processing large volumes of data can also be challenging, especially if you want the processing to occur in reasonable timescales. Most of my

analysis of particle tracking microrheology data is via the MSD statistic; this was calculated using code adapted from Tarantino's[149] msdanalyser class in MATLAB. Tarantino's original code is both elegant and robust to position-time tracks of varying durations where observations may be irregularly spaced or missing, but these features mean it is inefficient for experimental data consisting of long tracks of observations spaced uniformly in time.

Several important modifications were made to suit my purposes: Instead of calculating all possible delay times within each track, I check that each track in a batch of processing has the same uniform time spacing and then select logarithmically spaced delay times. This dramatically reduces the processing required as the MSD is then only calculated at these delay times; while I would like to give a measurement of the speed-up achieved, the original code would take days to calculate the MSD for a track of 1 million observations while my modified version runs in a few seconds.

3.2.4   Quantifying Viscoelastic Properties

Following the Generalised Stokes-Einstein Relation (GSER), if the motion of a particle is dominated by thermal driving forces, the MSD is equivalent to the creep compliance of the particle's environment. The MSD can be analysed in the time domain, or it can be used to calculate the complex modulus of the material and further analysed in the frequency domain. First it was calculated using code adapted from Tarantino's[149] msdanalyser class in MATLAB. Tarantino's original code is both elegant and robust to position-time tracks of varying durations where observations may be irregularly spaced or missing, but these features mean it is inefficient for experimental data consisting of long tracks of observations spaced

uniformly in time.

Several important modifications were made to suit my purposes: Instead of calculating all possible delay times within each track, I check that each track in a batch of processing has the same uniform time spacing and then select logarithmically spaced delay times. This dramatically reduces the processing required as the MSD is then only calculated at these delay times; while I would like to give a measurement of the speed-up achieved, the original code would take days to calculate the MSD for a track of 1 million observations while my modified version runs in a few seconds.

For an optically trapped bead in a fluid such as water, the creep compliance can be approximated using Kelvin-Voigt ideal viscoelastic model (henceforth referred to as K-V model) as discussed in Section 3.1.2. The two parameters of the K-V model are the stiffness and the characteristic relaxation time. The stiffness is the optical trap stiffness, measured using either the position variance or the MSD plateau. The characteristic relaxation time is measured using two methods I have developed, one time domain method and one frequency domain method, both of which will be described below.

3.2.4.1 Time Domain Analysis

Least-squares fitting was used qualitatively and quantitatively, with interpretation by inspection of MSD curves aided by estimation of the gradient using a "rolling fit" method: applying a least-squares fit to a small number of points in the curve (normally 5 or 10) to reduce the noise in the estimated gradient. To speed this up, an algebraic least-squares estimator [111] was used, resulting in a 300-fold speed-up compared to using MATLAB's curve fitting toolbox. The result can be seen in Figure 3.10i, where the rolling-fit

method has been used to estimate local power-law exponents (equivalent to gradient on a log-log plot).

Different regions on the MSD curve indicate the compliance of different physical processes. In the ideal case, the MSD of an optically trapped bead exhibits an extended plateau where the power-law exponent is 0. Experimental data, on the other hand, typically has a noisy plateau and may also exhibit an up-tick at long times due to drift in the system. The noisy plateau can be seen in Figure 3.10Bi, while both the noise and the up-tick can be seen in Figure 3.6b.

To calculate the trap stiffness, the variance could be used, but this is sensitive to any long-time up-tick caused by drift, in which case it will underestimate the trap stiffness. Instead, the power-law exponent can be used to identify a time range for the plateau, and the mean MSD over this time range can be taken to be the plateau MSD.

The characteristic relaxation time for an optically trapped bead is the time at which the short-time (viscous dominated) compliance is equal to the long-time (elastic dominated) compliance. Measured and predicted relaxation times are shown for both simulated data (column A) and experimental data (column B) in Figure 3.10. The time domain method is explained below, while the frequency domain method is explained in the next section.

The time domain method is demonstrated in Figure 3.10ii: Two time ranges are chosen manually, and a linear fit is performed to data from each range in the form $\log(\tau)$ against $\log(MSD)$. The intercept time of the fits is calculated algebraically and taken to be the characteristic relaxation time.

In the situation of a trapped bead in a Newtonian fluid, the time domain method is exact. For experimental situations such as a bead trapped in
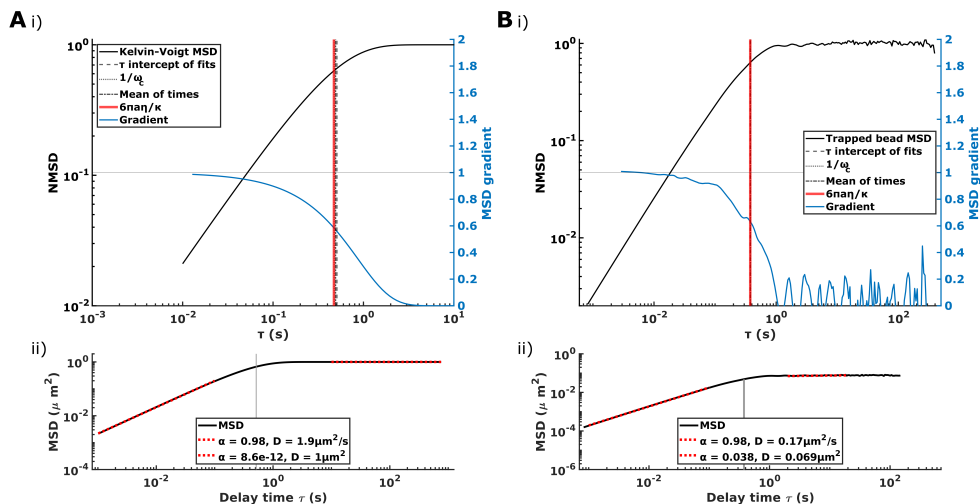
Figure 3.10: Validating corner time finding for (a) simulated NMSD data from a Kelvin-Voigt model and (b) real NMSD data from an optically trapped bead in water. i) MSD curves (black) with MSD power-law exponent (blue). Theoretical corner time (red), measured corner times from the time-domain method (grey dashed), frequency-domain method (grey dotted), and the mean of the two (grey dash-dot). The overlap demonstrates good agreement between the methods. ii) Time domain method showing two fits and τ_c, the corner time (intercept of fits).

water, the fluid is sufficiently close to being a Newtonian fluid over the experimentally accessible time range that it can be approximated as such. The time domain method is based upon the observation that the short-time MSD is given by the time-invariant viscosity and the long-time MSD is given by the trap stiffness:

$$MSD(\tau \ll \tau_c) = \frac{k_B T}{3\pi a} \frac{\tau}{\eta}, \tag{3.16}$$

$$MSD(\tau \gg \tau_c) = \frac{2k_B T}{\kappa}, \tag{3.17}$$

where $k_B T$ is the thermal energy, a the bead radius, τ_c the corner time, η the Newtonian viscosity, and κ the trap stiffness. As long as the experimental systems is well described by the K-V model, extrapolation beyond the fitting range is valid and the intercept time of the two fits gives the characteristic relaxation time.

From the two equations above, the viscosity of the fluid can be inferred by using the corner time and the trap stiffness as per Equation 3.4. This follows from the viscous compliance at the corner time being equal to the time-invariant compliance of the trap. Thus the viscosity of a sample can be measured with minimal assumptions and sensitivity to noise. I refer to this method as the Kelvin-Voigt (K-V) method as it is derived from the optical trap acting as a Kelvin-Voigt viscoelastic solid.

Alternatively, viscosity could be calculated using the Stokes-Einstein relation, Equation 2.14. The experimental MSD curve can be analysed to find the diffusion coefficient, D, and hence the solvent viscosity, η. I refer to this method as the Stokes-Einstein Relation (SER) method.

To measure the diffusion coefficient, I have investigated two possibilities. The first is least-squares fitting to a power-law equation,

$$log(MSD) = log(2D) + \alpha log(\tau), \tag{3.18}$$

with power-law exponent α. Fitting has the advantage that the power-law exponent can reveal rheological properties of the system such as the loss tangent, indicating whether the behaviour of the system is viscous, elastic, or viscoelastic at a given timescale.

Alternatively, the diffusion coefficient can be defined as a function of lag time,

$$D(\tau) = MSD(\tau)/\tau, \tag{3.19}$$

which has two advantages: firstly, it is less sensitive to errors affecting the power-law exponent; secondly it is insensitive to the lag time being analysed. The second point is important as power-law fitting finds D using the y-intercept of the best-fit line. Clearly if the time range being analysed

is far from 1s, a small change in α will lead to a large change in D.

It is also possible to calculate the viscosity using the Fourier Transform (FT) of the MSD. Recall that the loss modulus $G''(\omega) = \eta\omega$, and thus the imaginary part of the complex modulus can be used to calculate η. Several methods for optimising the SNR on the FT are discussed in Section 3.3.3, and the viscosity calculated by two of these has been included here.

For comparison, I present the results of each method when applied to the same data of an optically trapped bead. Figure 3.11 shows a set of MSD curves taken with different trap stiffnesses controlled by varying the laser power, and the viscosities calculated by each method. As can be seen, the K-V method provides substantially better agreement with theory than the SER method. The non-fitting SER method is less noisy, but both SER methods systematically overestimate the viscosity relative to the expected value and the K-V method. Each of the Fourier transform methods overestimates η by approximated a factor of π; the possibility of a numerical error in the Fourier transform has been ruled out as my implementation and one from Smith et. al.[153] have been compared and give exactly the same results.

The K-V method also has another conceptual advantage: By plotting $\kappa/6\pi a$ against η_{water}/τ_c, the viscosity of a multiple measurements in a sample can be quickly compared, both to each other and to the viscosity of water. This is shown as the inset to Figure 3.11b. The data agrees well with the predicted viscosity of water over a wide range of trap strengths, while an increase in viscosity would place data points below the dashed line.

72
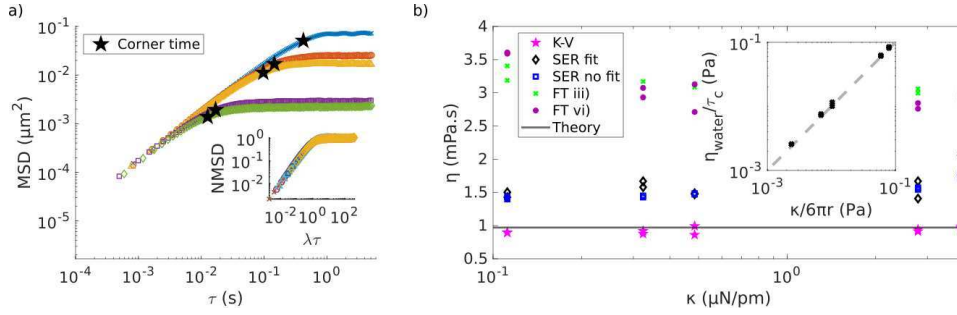
Figure 3.11: a) Experimental MSD curves for an optically trapped bead in water, varying trap stiffness. Inset: Curves normalised spatio-temporally using the empirically measured trap stiffness and corner time. b) Viscosities calculated for each set, using K-V, SER and FT methods. Theoretical viscosity for water at 298 K (0.97 mPa·s) also shown. Inset: Inverse stiffness against inverse corner time plot, with viscosity of water shown as dashed line.

3.2.4.2   Frequency Domain Analysis

Performing a Fourier transform on rheological data is non-trivial due to non-convergence of the Fourier transform integral and truncation errors introduced by numerical transforms. To this end, I implemented the method proposed by Evans et. al.[109] and the improvements proposed by Tassieri et. al. [117, 153], as discussed in Section 2.2.3. Key to this method is accurate numerical inversion over a wide range of frequencies. Characterising and minimising the numerical error in the inversion process is discussed later in Section 3.3.3.

Equivalent to the characteristic relaxation time, the characteristic relaxation frequency, or corner frequency, of an optical trap can be used to find the viscosity of the suspension fluid. This is the frequency at which the elastic and viscous moduli are equal, shown with a dashed line in Figure 3.12 A and B i). To simplify the numerical approach, I considered the loss
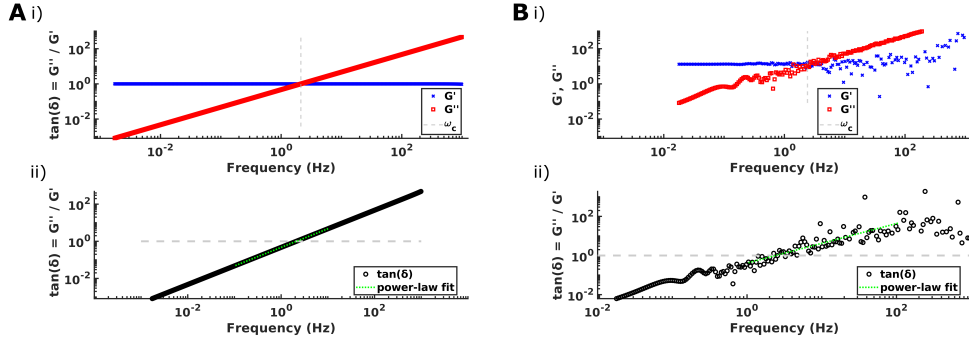
Figure 3.12: Validating characteristic relaxation frequency measurement for (a) simulated NMSD data from a Kelvin-Voigt model and (b) real NMSD data from an optically trapped bead in water, both shown in Figure 3.10. i) Complex modulus with intercept frequency, ω_c, marked. ii) Frequency domain method showing fit to $\tan(\delta)$ and ω_c, the frequency where fit intercepts $\tan(\delta) = 1$.

tangent,

$$\tan(\delta(\omega)) = \frac{G''(\omega)}{G'(\omega)}, \tag{3.20}$$

$$\tan(\delta(\omega_c)) = 1, \tag{3.21}$$

and use least-squares fitting to a power-law,

$$\log\left(\tan\left(\delta(\omega)\right)\right) = A\log(\omega) + \log(B), \tag{3.22}$$

where A and B are free parameters for the fit. Thus the frequency where $\tan(\delta) = 1$ can be found by

$$\omega_c = \exp\left(\frac{\log(B)}{A}\right). \tag{3.23}$$

The fitting and result in the frequency domain are shown in Figure 3.12 for simulated and real MSD. The fit results are compared to prediction and the time domain method in Figure 3.10i, where they are found to be in excellent agreement.

3.3 Discussion

Clearly no experimental system is ideal however simple models can still aid in understanding them. For example, the model of the optical trap as a Newtonian fluid in parallel with a Hookean spring allows for easy and accurate quantification of fluid viscosity, and this approach maintains its validity when applied to more complex systems. The experimental system exhibits small departures from ideal behaviour however these are negligible compared to either the random errors associated with observing stochastic processes for finite time durations, or the numerical errors introduced in data processing as shown in Figure 3.17.

3.3.1 Systematic Errors

There are three main sources of systematic error in particle tracking experiments: external noise and the two particle tracking-specific errors identified by Savin and Doyle[154, 155] as static and dynamic error. External noise comes from various lab sources, which have been eliminated where possible such as by turning off the overhead fluorescent lights in the lab. Interference from other electronic devices, such as the power supply for the trapping laser, cannot be avoided but has been characterised as shown in Figure 3.6. These noise sources systematically increase the MSD at all lag times but can be removed with a narrowband stop filter as described in Section 3.2.3.1.

3.3.1.1 Static Error

Static error is caused by the contrast to noise ratio of the images, placing a limit on the smallest displacement it is possible to track. This has the consequence of limiting the minimum compliance that can be accurately measured by passive microrheology. It can be modelled by relating true position, x, to apparent position $\hat{x} = x + \mathcal{N}(\epsilon^2)$, using $\mathcal{N}(\epsilon^2)$ to denote a random variable drawn from a normal distribution with variance ϵ^2. Accounting for static error, the apparent MSD can be written as

$$\langle \Delta \hat{r}^2(\tau) \rangle = \langle \Delta r^2(\tau) \rangle + \epsilon^2, \tag{3.24}$$

where ϵ^2 is the magnitude of the static error. While static error introduces a random error on the apparent position, it causes a systematic increase in the apparent MSD. Hence if the true MSD is not much greater than the static error there will be significant overestimation of the MSD.

I characterised this error in the optical trapping system when imaging $5\,\mu m$ diameter polystyrene beads in transmission by drying polystyrene beads onto a $170\,\mu m$ thick coverslip and then attaching the coverslip to a $2\,mm$ microscope slide for imaging such that the beads were sandwiched between the coverslip and microscope slide.

To separate the displacement due to vibrations in the system from the apparent displacement due to static error, I imaged two beads simultaneously and calculate the difference between the bead co-ordinates. While the measured position of each bead individually is affected by both vibrations and static noise, the vibrations are the same for both beads and the apparent difference is given by $\delta \hat{x} = \delta x + \sqrt{2}\mathcal{N}(\epsilon^2)$. Thus the difference between the measured bead positions allows a direct estimation of the magnitude of the
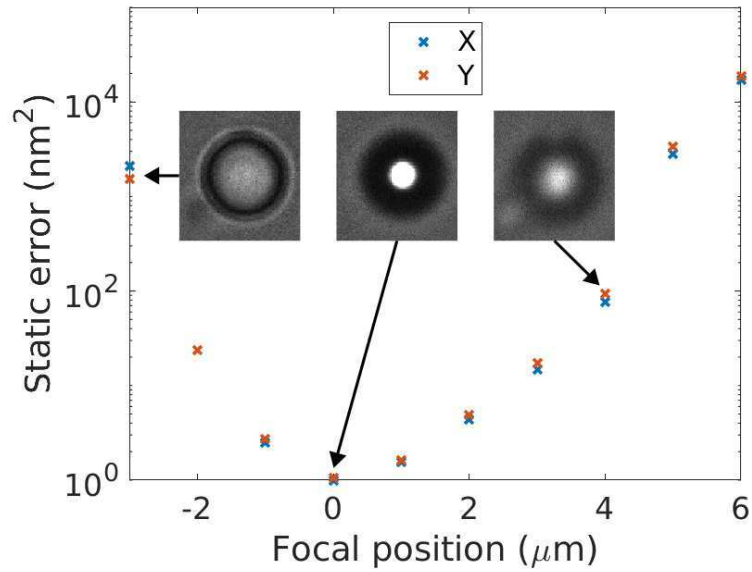
Figure 3.13: Static error for beads attached to coverslip measured for different focal positions. Inset are images of a bead from three different focal positions showing a 9 μm field of view. Note that saturation in the central image is due to the display contrast, not camera saturation.

static error.

Figure 3.13 shows how static error varies with focal position. This variation comes from the differing contrast at different focal positions. With this imaging setup, it is possible to obtain static error as low as $1\,\mathrm{nm}^2$. During microrheology measurements using with optical tweezers, however, the bead will be free to move in z, and thus static error will be higher. For this reason, when considering experimental data, MSDs below $100\,\mathrm{nm}^2$ are treated cautiously.

The effect of static error on the MSD of an optically trapped bead can be seen in Figure 3.14, where I artificially reduced the spatial resolution by increasing the threshold value in the image processing. At the shortest delay times, high threshold values cause the apparent MSD to depart from the true value. At lag times such that the bead displacements are much greater than the static error, the experimental MSD is almost unaffected.
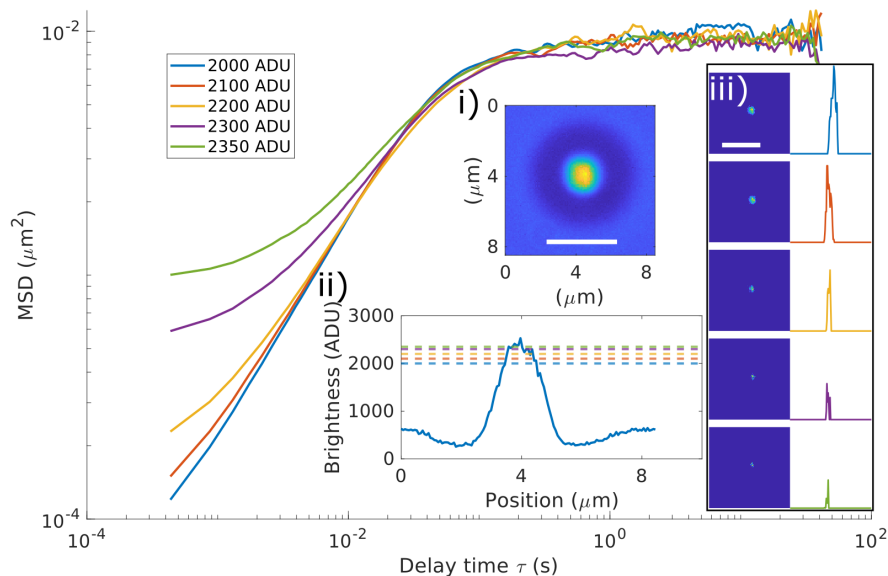
Figure 3.14: MSD curves taken from a single trapped bead (shown in inset i) with different acquisition parameters demonstrating the effect of static error on MSD with varying contrast (artificially induced here by changing the threshold level, shown as dashed lines on inset ii). Background subtracted images are shown in inset iii, along with line plots through the background subtracted images. Scale bars are 4 μm.

This can be verified using the non-Gaussian parameter as shown in Figure 3.9: static error only affects the increment distribution at short lag times, allowing a cutoff lag time to be determined above which the MSD has insignificant influence of static error.

In optical trapping experiments, static error is minimised by changing the axial position of the trap equilibrium via removal of lens L1 (Figure 3.3) along with use of a bright halogen lamp configured in Köhler illumination. For cell and bead experiments, the z-position of the bead is determined by the cell, allowing a focal position to be chosen to minimise static error.

3.3.1.2 Dynamic Error

Dynamic error is caused by bead motion during the exposure time, and limits the shortest timescale over which it is possible to accurately track the bead position; in general this is difficult to quantify and depends on both the exposure time and the rheology of the sample (see [155] for more detail). The exact time-scale over which dynamic error has significant effect depends on the power-law exponent of the MSD at time equal to the exposure time, with a lower exponent (to a minimum of 0) causing dynamic error to have an effect at longer time-scales relative to the exposure time[155]. In all cases, dynamic error causes underestimation of the MSD.

For a micron-sized bead optically trapped in water, the timescales affected by dynamic error will depend on the stiffness of the trap. If the trap relaxation time is much longer than the exposure time, dynamic error will have an effect at lag times up to a few times the exposure time, hence causing an overestimation of the viscosity; if the trap relaxation time is similar or shorter than the exposure time, the dynamic error will cause underestimation of the MSD at all lag times, causing an overestimation of trap stiffness. These effects are seen clearly in Figure 3.15, where it presents on MSD curves as super-diffuse motion in the shortest delay times. That is to say, power-law exponent $\alpha > 1$ as demonstrated by the dashed lines. Here, dynamic error is causing an underestimation of the mean-squared displacement of the particle being tracked.

As the exposure time approaches the trap relaxation time, the effect of dynamic error increases at the shortest lag times. In the case of the 10 ms exposure time, there is no time scale where the diffuse motion of the bead is accurately measured. When the exposure time exceeds the trap relaxation time, the apparent plateau height (elastic compliance) is significantly
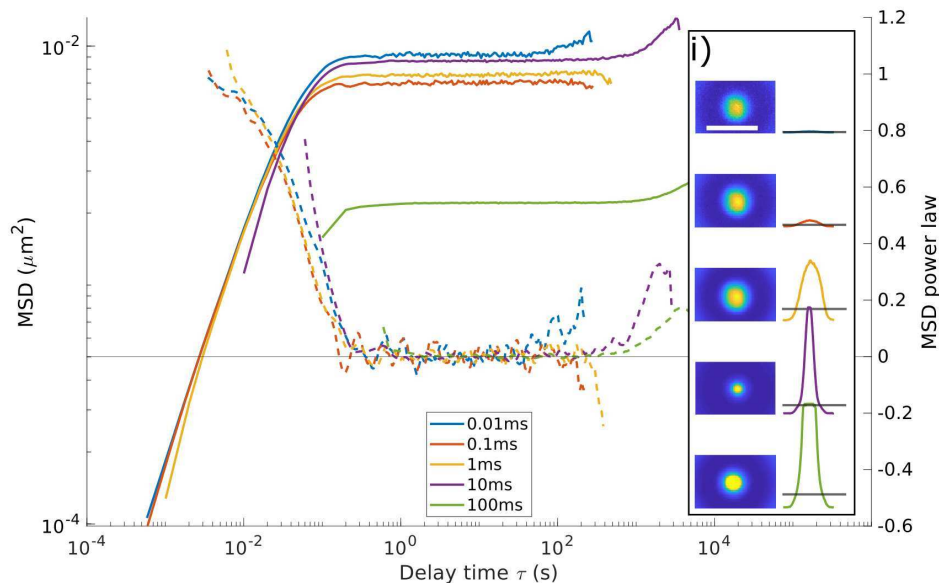
Figure 3.15: MSD of an optically trapped bead in water showing the effect of dynamic error on MSD (solid lines) and power-law scaling (dashed lines) with varying exposure time. Inset i: representative images and line plots. Scale bars in insets are $4\,\mu m$.

reduced and no diffuse motion is seen. This can be seen with the $100\,ms$ exposure time. To understand the effect, consider the diffusion of the bead within the trap. During the $100\,ms$ exposure time, the bead has diffused across the entire length scale of the trap, and the image acquired is an average of all positions the bead occupies. Thus the MSD between sequential frames ($100\,ms$ apart) will be much lower than expected.

While estimating dynamic error is non-trivial, minimising it is not. As dynamic error is the effect of motion blur on particle tracking, it can be simply seen that minimising the exposure time will minimise dynamic error. I have used exposures times of 100 to $250\,\mu s$ even when increasing exposure time would not slow down acquisition, whilst ensuring there is plenty of light to keep static error low. In other words, if the ROI is such that the camera would run at 1,000 fps, an exposure time of up to $1\,ms$ would not slow the acquisition. In this case, I would still use an exposure of $100\,\mu s$ because this minimises dynamic error.

I also disregard the first few points of the MSD from quantitative analysis, based on the MSD power-law exponent. This is justified by Figure 3.15, where the power-law exponents have an increase at the shortest times which is caused by dynamic error. While the effect of dynamic error while probing water (with sensible image acquisition parameters) is small, the effect of dynamic error when probing cells or other viscoelastic materials can be much larger. Thus I chose to err on the side of caution and if there is an increase in power-law exponent at the beginning of an MSD curve, I exclude those time points.

The reader may notice that the bead image from the $100\,\mathrm{ms}$ exposure time is saturated (Figure 3.15 inset bottom row). By a simple geometric argument it can be seen that image saturation has no effect on the centroid calculation: The centroid for a discretely sampled distribution (e.g. a Gaussian image of a bead) is the same as the first moment of that distribution, and equal to the integral of the distribution multiplied by the position co-ordinate, normalised to the area under the peak. Or, in 1 dimension,

$$C_x \equiv \frac{\int_0^\infty xp(x)dx}{\int_0^\infty p(x)dx}, \tag{3.25}$$

where C_x is the centroid (or first moment) and $p(x)$ is the distribution in question. Note that the first moment, centroid, and centre of area are all equivalent.

Consider now a Gaussian distribution and a truncated Gaussian distribution, where values above some truncation value are instead set equal to that truncation value. These are good approximations of the bead image and saturated bead image. The symmetry of the distribution suffices to show that image saturation has no bearing on dynamic error. It will, however, have an effect on static error: the precision of the first moment calculation

is proportional to the area between the threshold and the truncation value so increasing illumination brightness beyond saturation will increase static error.

3.3.2 Random Errors

A practical challenge of microrheology is one shared by all studies of stochastic processes: How long do you need to watch a sequence of random events for the time-average to accurately represent the process behind the events? In passive microrheology, one could consider the number of independent observations of the MSD for a given delay time. If the experimenter wishes to probe the MSD with at a delay time of up to $10\,\mathrm{s}$, consider that $100\,\mathrm{s}$ of experimental data will have only 10 independent samples at this delay time.

To demonstrate the importance of adequate sampling, a single position-time recording, consisting of 500,000 samples collected at $1.214\,\mathrm{kHz}$, was truncated to varying durations. Figure 3.16 shows MSD curves, trap stiffness, κ, and diffusion coefficient, D, calculated using between 10 and 500,000 samples. When viewing the MSD curves, especially notice the change at the highest τ of each one, where statistics are poorest. Diffusion coefficients were calculated by fitting the short lag-time MSD to

$$MSD = 2D\tau^{\alpha}, \tag{3.26}$$

where D is the diffusion coefficient and α is the power-law exponent.

To assess random error with varying sample number, trap stiffness and diffusion coefficient were compared to the values found using all 500,000 samples. Brownian dynamics simulations were performed following the
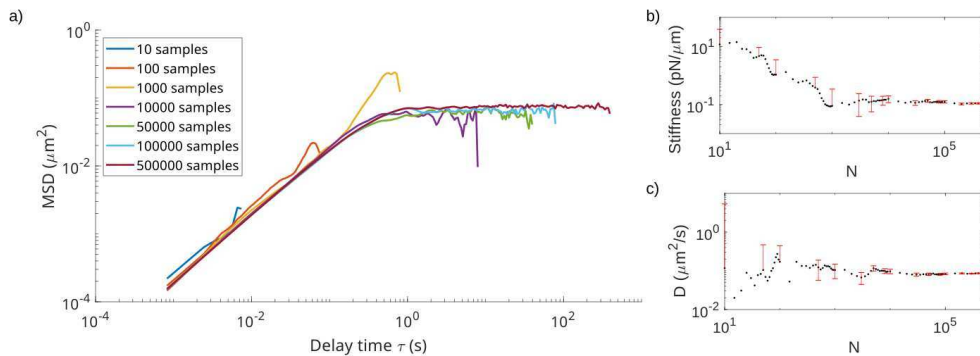
Figure 3.16: a) MSD estimate improving with increasing number of samples. b) and c) Trap stiffness calculated using Equation 3.2 and diffusion coefficient D by fitting to Equation 3.26, for increasing number of samples, N. Error bars indicate random error estimates frp, Brownian dynamics.

method of Volpe[156], using the same parameters as the experiment. For each number of samples plotted in Figure 3.16, 1,000 trajectories of that length were generated and the trap stiffness and diffusion coefficient were quantified. The standard deviation of these 1,000 simulated measurements was used to estimate the random error for the experiment, shown as error-bars on panels b) and c).

To achieve an accurate measure of trap stiffness, using 160 s or 200,000 samples will give a relative error of 7%, however this will depend on the trap stiffness as a less stiff trap will have a longer relaxation time and 160 s will contain fewer independent observations at lag time equal to the trap relaxation time. Diffusion coefficient, on the other hand, requires fewer samples and reaches 9% relative error for 24 s or 30,000 samples. This is because the analysis used here (Equation 3.18, $log(MSD) = log(2D) + \alpha log(\tau)$) utilises MSD data from the shortest lag times to calculate the viscosity, and the shortest lag times have the best statistics as there are more independent observations.

3.3.2.1   Image Analysis

Position-time data has thus far been acquired using video microscopy and centre-of-mass tracking, with real-time image acquisition and processing enabling longer observation durations. The centre-of-mass particle tracking relies upon the bead image having a bright centre, and no other features brighter than the threshold in the region of interest (ROI) used for image acquisition. It is easy to ensure this in the case of optically trapped beads in transparent solutions, or beads attached to cells, because there are few features visible and a small ROI is used. In samples where this is not the case, a more advanced image analysis may improve ease of use and reduce errors on particle tracking.

One possibility is to use the cross-correlations of subsequent image frames in order to calculate the displacement between subsequent frames, or between the first and Nth frames. In either, an image kernel containing the bead is convolved with a subsequent image to find the position of the bead within the image, and hence the displacement between the two images. Considering the image and the kernel as matrices M_{ij} and k_{ij} of pixel intensities, the cross-correlation can be written

$$C_{xy} = \sum_{i=x}^{x+w} \sum_{j=y}^{y+h} M_{ij} k_{ij}, \qquad (3.27)$$

where w and h are the width and height of the image kernel, respectively. The greatest value in the cross-correlation matrix corresponds to the kernel position closest to the bead position in that image, i.e. the bead position to the nearest pixel. The bead position can be found with greater precision by calculating the centroid of the cross-correlation.

The cross-correlation analysis could be implemented using MATLAB's *xcorr*

function, however this would require every image acquired to be saved and processed after the experiment. To avoid the additional challenges brought by storing such volumes of data, this could be implemented in Java and run by Micro-Manager during data acquisition. The implementation would need to be tested for performance, both in terms of computation time and static error. Using image cross-correlations would reduce static error when tracking particles against noisy backgrounds, allowing accurate microrheology study of samples such as tissues. It would also allow particles to be tracked over a wider axial range as the analysis would no longer rely on a central bright spot.

3.3.3   Optimising SNR for Complex Moduli

Firstly, the MSD data must be as clean as possible - experimental noise should be removed as described in Section 3.2.3.1. Optimal SNR could be achieved by fitting MSD data to an analytical equation such as the K-V model ($NMSD = 1 - e^{-\lambda \tau}$), from which an analytical expression exists for the Fourier Transform. Use of fitting models, however, is limited to data for which a preconceived fit exists; perhaps more importantly, it does not distinguish between the noise which one wishes to remove and the system's departure from model behaviour.

For example, one may fit the K-V model to data from a bead suspended inside a gel, expecting a viscous short-time response and an elastic long-time response. If the gel actually exhibits sub-diffusion on short times, or a time-dependent elasticity on long times, the model will not reflect this and the resulting Fourier transform and complex modulus will be incorrect. Hence I have avoided fitting models to my experimental data, instead focussing on how to optimise the processing for best SNR.

In Figure 3.17 I demonstrate different methods to improve the SNR of the resulting viscoelastic modulus for an optically trapped bead in water. Since water can be approximated as a Newtonian fluid over the relevant time scales, the viscoelastic modulus should be well described by the Kelvin-Voigt model, with a constant storage modulus given by the trap strength and a loss modulus depending on frequency, $G''(\omega) = 0.97\omega$ mPa. The 6 methods have been denoted by Roman numerals, and the raw MSD data is shown as an inset. At long lag times, the MSD exhibits an up-tick due to pointing instability of the laser. For all methods, as described in Section 2.2.3, the MSD is interpolated before using the Fourier transform as described by Evans et. al.[109]. This interpolation pushes the high-frequency truncation errors beyond the bandwidth of the experiment.

Method i) is to simply use the entire MSD curve. This gives good SNR for frequencies where the viscous behaviour dominates, but poor SNR for the elastic plateau due to the slight gradient, as can be seen by the non-smooth behaviour on the loss modulus at frequencies below 100 Hz. At the lowest frequencies, the up-tick in MSD causes both storage and loss moduli to depart from expected behaviour.

Method ii) is to truncate the data at the gradient minima. This causes a large improvement to the SNR at low frequencies, however it also reduces the lowest frequency represented in the moduli. Method iii) is to truncate at the gradient minima, and replace the truncated data with a linear fit of the same gradient. Because the long-time behaviour of the experimental MSD is non-smooth, replacing with a smooth fit improves the SNR, but because the fit has a non-zero gradient, the loss modulus departs from expected behaviour at low frequencies.

Method iv) is to truncate the data, and replace with a smooth line of

gradient 0. As can be seen, this gives good SNR for the loss modulus across the whole frequency range probed, but poor SNR to the storage modulus at frequencies where the viscous behaviour dominates. While this is physically justified by the expected behaviour of a trapped bead, it constitutes replacing experimental data with a preconceived model for said data.

Method v) is to use a low-pass filter to smooth the MSD before interpolating and transforming the data. It provides good SNR to the storage modulus across the full frequency range due to the smoothness of the data, while the loss modulus still exhibits departure at low frequencies due to the gradient on the plateau. Again, this is physically justified by the expectation of a smooth MSD curve, but is doctoring experimental data based on preconceived models.

Finally, method vi) is to empirically measure the plateau height and corner time, and to simply replace the experimental MSD with the prediction of the K-V model. The numerical transform produces the expected storage and loss moduli across the entire range of frequencies due to the smoothness of the model data.

The above comparisons demonstrate that if one is to replace their data with a preconceived model, it is better to be in for a pound than in for a penny. For this reason, when handling microrheology data from live cells in the next chapter, I have avoided any filtering, fitting or data replacement methods, instead opting to have non-perfect Fourier transforms and viscoelastic moduli which are valid yet noisy representations of the experimental data.
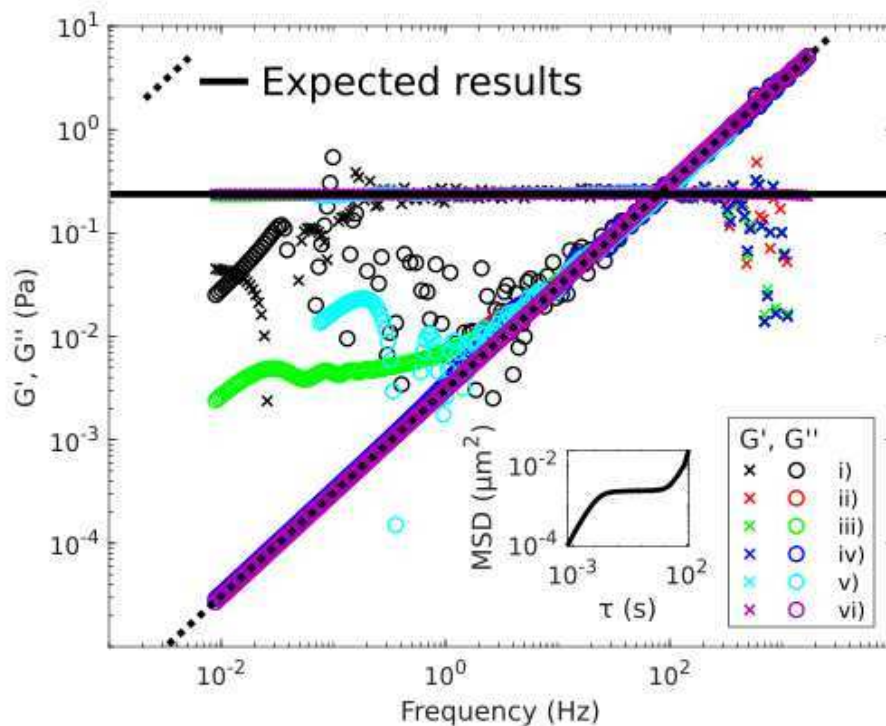
Figure 3.17: Storage (crosses) and loss (circles) moduli for a single dataset from an optically trapped bead (MSD curve inset). The key point of comparison is the frequency range over which each method coincides with the predictions. 6 different methods for improving SNR are demonstrated with varying efficacy. This figure serves to qualitatively demonstrate the range over which different numerical methods reproduce the expected results which are shown as solid and dashed lines to guide the reader. Each method is explained and discussed in detail in the text. Summary descriptions of the methods follow: i) Raw data, minimal pre-processing; ii) Short-time MSD only, truncated at gradient minimum; iii) Truncate and extrapolate at constant gradient; iv) Truncate and extrapolate with zero gradient; v) Low-pass filter MSD; vi) Replace MSD with K-V fit.
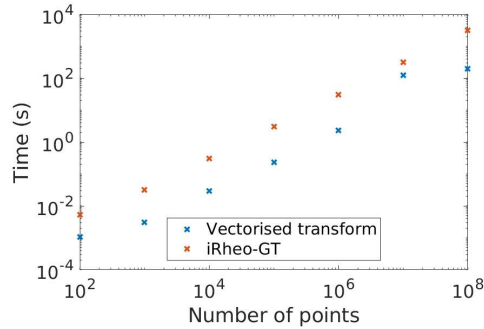
Figure 3.18: Average runtime for the rheological Fourier transform was measured for datasets of increasing size, comparing my vectorised implementation with a non-vectorised implementation[153]. The anomalous point at N=10^7 is discussed in the text.

3.3.3.1 Code Optimisation for Fourier Transform

Finally, I will now explain my code optimisation for the rheological Fourier transform algorithm. Due to the large datasets required to minimise errors (at least hundreds of thousands of points after interpolation), this is a necessity. Calculating the summation term in Equation 2.17 is the rate limiting step, with computation time proportional to the number of points. Due to the independence at different frequencies, it is possible to parallelise the calculation. In MATLAB this means writing the calculation as vector arithmetic instead of using a *for* loop.

The only limitation here is the additional memory requirement, however it is possible to perform the calculation on datasets comprising over 10^6 points using a desktop PC with only 16 GB of RAM. The runtime for my vectorised implementation is compared to the implementation provided by Smith et. al.[153] in Figure 3.18 where it can be seen that vectorisation provides roughly 10× speed-up.

To improve the robustness of the Fourier transform, and avoid crashes due to out-of-memory errors, my vectorised implementation uses an adaptive

method for array assignment. First it checks if there is enough memory to run fully vectorised, as this would give the best speed-up (largest array requires $2N \times N_f \times 8$ bytes, for N input time points and N_f output frequencies). If it is not possible, instead it will run "semi-vectorised". This leads to a parallelisation factor which is dependent on the memory available. In the worst performance scenario, the system memory is enough to store the array but the operating system needs to move data to the swap partition to make RAM available, leading to the anomalously poor performance seen at $N = 10^7$.

Chapter 4

External Passive Microrheology of Cellular Adhesion

4.1 Introduction

This chapter contains the major results obtained while working on this thesis.The results within this chapter have been published in *Acta Biomaterialia* under the title "Living Cells as a Biological Analog of Optical Tweezers – a Non-Invasive Microrheology Approach" [79]; many of the figures included here are reproduced from the paper (and are of my own creation), while the discussion here goes beyond that in the published work.

A version of the analytical framework and modified Generalised Stokes-Einstein Relation (GSER) were originally published by Warren et. al. without quantitative analysis of cell results[1], I include it here and build upon the analogy to optical trapping. Novel work presented here includes

novel quantitative analysis through the framework of the GSER, new quantification of non-equilibrium dynamics and observation of active strain fluctuations. This includes the first simultaneous observations of cell stiffness and strain fluctuations, allowing the effects of cytoskeleton-targetting drugs to be better understood.

The chapter is structured as follows: a brief introduction containing specific biological context, followed by the experimental method in detail, including considerations for minimising the effects of particle tracking errors which were discussed in Chapter 3. Next, an analytical framework building upon Section 2.2.2. The results section presents an interpretation of the Mean-Squared Displacement (MSD) for a bead in a typical cell measurement, followed by results from the analyses developed in Chapter 3. Finally the work is discussed in the context of the field of single cell mechanobiology, with reference to prior results which were presented in Chapter 2.

4.2 Experimental Methods

The experimental method was to use the optical trap to affix a functionalised bead to the surface of a live cell, and then to make passive microrheology measurements of the cell by recording the position of the bead over several minutes. The experiment is summarised in Figure 4.1 and the setup and rationale are explained in more detail below. Rheological data was acquired as described in Section 3.2.2 using the script described in Appendix A. Data were analysed in MATLAB as previously described in Section 3.2.3. I will now describe the preparation and execution of cell microrheology experiments.
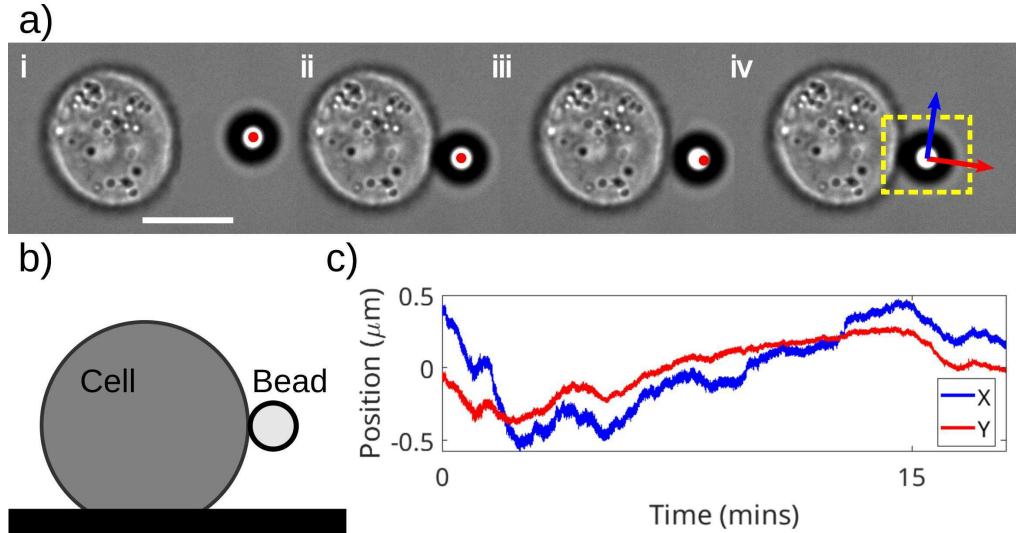
Figure 4.1: Experimental procedure for microrheology of live cells. a) i: First, the optical trap (red dot) is used to position a bead on a cell. ii: The bead is held in place to allow time for binding, iii: which is tested by pulling the bead away from the cell, iv: before turning off the laser and recording video with a small region of interest (yellow). Bead co-ordinates were post-processed to find radial and tangential components (red and blue arrows). Scale bar: 10µm. b) Side view of the cell showing ideal bead position on the equatorial plane of the cell. c) X-Y Position-time trace before co-ordinate transform acquired from bead attached to cell. Figure reproduced from Hardiman et. al.[79]

4.2.1 Cell Preparation

Hela S3 (ATCC CCL-2) cells were grown in Dulbecco's Modified Eagle Medium, supplemented with 10% (v/v) Fetal Bovine Serum (Merck: F9665), 1% (v/v) L-glutamine (Merck: G7513), 1% (v/v) Penicillin-Streptomycin solution (Merck: P0781) and 1% (v/v) Non-essential Amino Acid Solution (Gibco:11140-050); these were grown in a T75 flask using the same protocols as for adherent cells. A portion of the cells were adhered to the flask but remained visibly rounded at any time, and these cells were used for microrheology experiments and confocal imaging, while the cells which remained in suspension were used to continue the cell line.

Before microrheology experiments, 10^4 cells per well were seeded into either
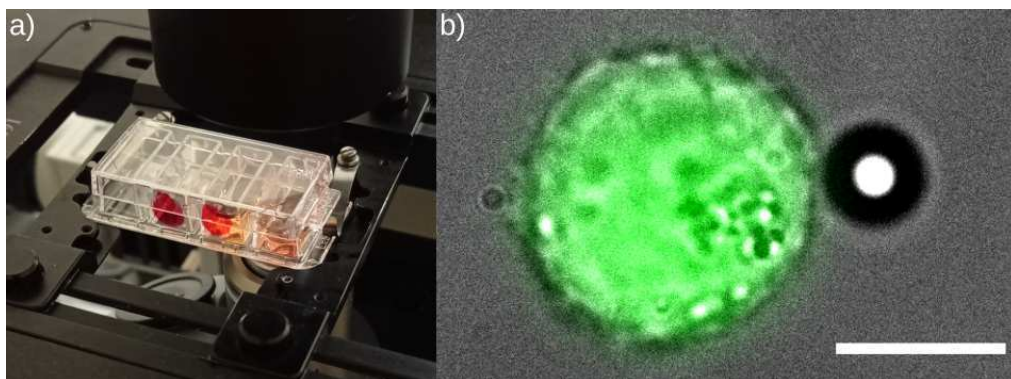
Figure 4.2: a) 4-well microslide mounted on microscope stage. b) Merge of brightfield (grey) and Calcein-AM fluorescent (green) images of a cell with bead attached. Fluorescent illumination was with the LED shown in Figure 3.2 and imaging with the same camera as brightfield imaging. Scale bar: 10µm

4 or 8 well microslide (Ibidi, Germany, 80427/80827; Figure 4.2a) with 500 µL of growth media as above. Cells were incubated overnight at 37°C with 5% CO_2, and 2 hours before experiments the media was changed for 200 µL of serum-free Minimum Essential Medium Eagle (Merck: M2279) supplemented as for the growth media (with the exception of FBS) and 5µg Calcein-AM (ThermoFisher, USA, C3099) for cell imaging. An example fluorescent image is shown in Figure 4.2b, where esterase enzyme activity within the live cell activates the fluorophore.

4.2.2   Microrheology Measurements

Streptavidin-functionalised polystyrene beads (5µm diameter, Spherotech: SVP-50-5) were rinsed and centrifuged per the manufacturer's instructions. Beads were re-suspended in serum free media at 10,000 times dilution and added in 10µl increments. The trapping laser was blocked when adding beads because the scattering force causes beads to precipitate out away from the current field of view. Once some beads had sedimented near a chosen cell, the trap laser was unblocked.

The optical trap was used to manoeuvrer a bead to a chosen cell (Figure 4.1a i), and then the correct focal position was judged by eye and controlled using the microscope focus dial. The aim was to stick the bead where the cell surface is vertical so the direction normal to the cell surface lies in the imaging plane.

The angle of the cell surface at the point of contact can be inferred from the change in bead equilibrium position in three dimensions when moving the trap towards the cell. If the surface of the cell is vertical, the displacement of the bead will be purely horizontal. When the surface of the cell is not vertical, there will be vertical displacement of the bead, and the profile of the bead image changes (e.g. the bright central maximum is diminished). Thus angle of the cell at the point of contact can be qualitatively evaluated when sticking the bead.

The bead was held in place (Figure 4.1a ii) using a weak trap (κ =1pN/µm) for a minute before trying to pull the bead away from the cell (Figure 4.1a iii); this allowed me to be sure that the bead had adhered specifically. The weak trap would be strong enough to break non-specific binding, but not strong enough to pull a membrane tether from the cell.

The laser was turned off once the bead was adhered, and a region of interest was selected for the measurement (Figure 4.1a iv) by drawing a box on the Micro-Manager preview window. The acquisition script uses this region for particle tracking and is described in detail in Appendix A.

The Hela S3 cell line was chosen as they adhere to glass coverslips but remain rounded (see Figure 4.3), allowing the bead to be placed where the cell surface is normal to the imaging plane, as shown in Figure 4.1b. Confocal imaging was performed by treating the cells with Latrunculin B (or control treatment) as described in Appendix B, and provided confirma-
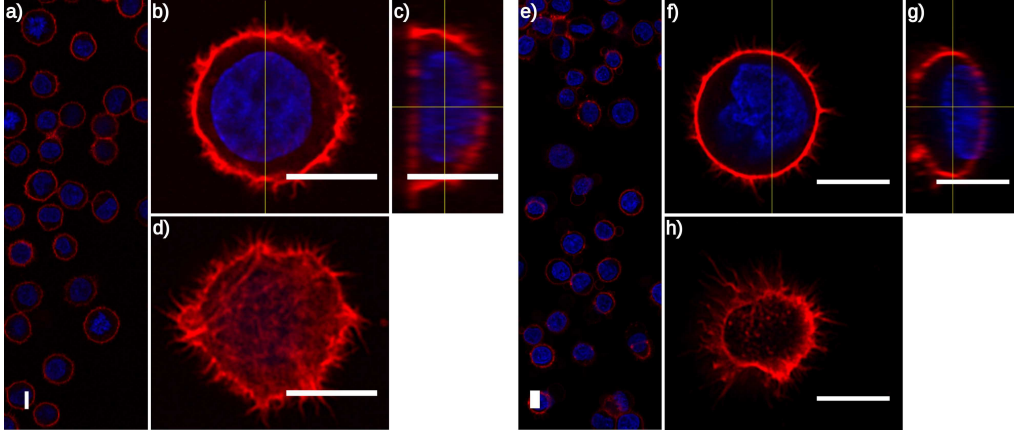
Figure 4.3: Actin cytoskeletons (red: phalloidin-rhodamine) and nuclei (blue: Hoescht 33342) for HeLa S3 cells in a-d) control conditions and e-h) after incubation in Latrunculin B for 15 minutes. Changes in actin distributions are, in summary, a thinner cortex around the cell, fewer filamentous protrusions (b and f), and a less dense basal cortex (d and h). Additionally the cell shape is closer to spherical (c and g). Immunofluorescence method described in detail Appendix B. Briefly, cells were grown overnight before fixing and staining. Images were acquired with a Zeiss Airyscan 2 confocal laser scanning microscope. Scale bar is 10µm. Figure reproduced from Hardiman et. al.[79].

tion that the cells remain rounded up after growing on coverslips and that Latrunculin B affects the actin cytoskeleton.

Adhesion to the coverslip is essential to prevent Brownian motion of the whole cell during the experiment. Cavity microslides (shown in Figure 4.2a) provided potential for running several independent experiments in parallel. Slides with 170 µm thickness were essential for optical trapping of beads because the choice of high-NA objective lens ($100\times$, 1.3 NA, 0.17 mm working distance).

Experiments consisted of repeated measurements of the same cell-bead pair, providing internal controls. If the cell-bead geometry (i.e. size and shape of cell, contact area between bead and cell) is invariant, changes in the MSD of the beads attached to cells, at short and intermediate lag times reflect

changes in the mechanical properties of the cells; this will be considered in more detail in Sections 4.3 and 4.4.

The experimental paradigm is shown graphically in Figure 4.4. After an initial measurement, either Latrunculin B was added to a final concentration of 1 μM or no change was made (control condition), and a second measurement was made around 40 minutes after the first. Measurement duration varied from 200,000 frames (110 seconds) to 3,380,000 frames (1,800 seconds), with a mean of 800,000 frames (466 seconds). Variation in length of measurement was caused by halting some acquisitions if the bead reached the edge of the acquisition region (yellow box on Figure 4.1). Various parameters are quantified for each measurement, and then the results are compared and changes are calculated.

Figure 4.4: Timing of measurements for change-over-time experimental paradigm. After the first measurement, a drug may be added, and a second measurement is made 40 minutes after the first. Figure reproduced from Hardiman et. al.[79].

Several considerations for performing these experiments are as follows: firstly, considering the biological system being studied. Since the cytoskeleton inside a cell develops internal stress after adhering to a surface, cells were grown overnight to allow them to equilibrate. Similarly, a biological response is expected when changing to serum-free media so this was changed at least 2 hours before the experiment to allow equilibration time.

Secondly, considering static error, the localisation error introduced in Section 3.3.1.1; this limits the minimum displacement it is possible to measure and hence the stiffest material that can be measured in microrheology. When sticking beads to cells, one could use a strong trap to push the bead

against the cell with a high contact force; this would almost guarantee bead adhesion. However the contact area between bead and cell will be higher and displacements at a given lag time will be lower, likely causing static error to dominate measurements. Also note that before taking a recording, static error can be minimised by focussing to have the brightest centre of the bead image.

Finally, considering dynamic error, the effect of bead movement during the exposure time which was discussed in Section 3.3.1.2. In general, the exposure time should be kept as short as possible to minimise dynamic error – I typically used 100µs for results reported in this chapter. At the same time, one should be careful not to use too much light when compensating for the short exposure time as the cells may be photosensitive. Here again the bead-cell contact area is important; greater contact area will cause the corner time to decrease analogously to the characteristic relaxation time described in Section 3.2.4. If the contact area is too great, the corner time will be comparable to or shorter than the exposure time, and dynamic error will mean the measured elasticity is greater than the true value.

4.3 Analytical Framework

To interpret the pseudo-Brownian motion of the bead *relative to the binding site* on the cell surface, a Generalised Langevin Equation describing its acceleration, $\vec{a}(t)$, could be written:

$$m\vec{a}(t) = \vec{f}_G(t) - \int_0^t [\zeta_c(t-\tau) + \zeta_s(t-\tau)]\vec{v}(\tau)d\tau, \qquad (4.1)$$

where m is the mass of the bead, $\vec{f}_G(t)$ the Gaussian white noise term, and the integral represents total damping force on the bead. By the superposi-

tion principle, the damping is described by two memory functions, $\zeta_c(t-\tau)$ and $\zeta_s(t-\tau)$, represent the viscoelastic response functions of the cell and solvent respectively. These can be written as

$$G_c^*(\omega) = \frac{i\omega\hat{\zeta}_c(\omega)}{\beta} \tag{4.2}$$

$$G_s^*(\omega) = \frac{i\omega\hat{\zeta}_s(\omega)}{6\pi a}, \tag{4.3}$$

with a hat (ˆ) denoting the Fourier transform, and β being a constant of proportionality with dimension of length[1]. Note that β may vary for different cell-bead pairs as it depends on (i) the cell radius, (ii) the number and the dynamics of the chemical bonds between the bead and the cell, (iii) the contact area between the cell and the glass coverslip, and (iv) the relative position of the bead with respect to both the cell's equatorial plane and the glass coverslip.

Interpreting this Langevin equation analogously to that for a bead in an optical trap (Equation 2.10), a version of the Generalised Stokes-Einstein Relation can be written in terms of the Fourier transformed NMSD, $\hat{\Pi}(\omega)$,

$$\frac{G_c^*(\omega)}{G_0'} = \frac{1}{i\omega\hat{\Pi}(\omega)} + \frac{m\omega^2}{\beta G_0'} - \frac{6\pi a G_s^*(\omega)}{\beta G_0'}, \tag{4.4}$$

where $\beta G_0' = \lim_{\omega\to 0}(G_c^*(\omega))$. The following assumptions simplify Equation 4.4: firstly, for micron-sized polystyrene beads, the inertia term $m\omega^2$ is negligible for frequencies up to MHz; secondly, for Newtonian solvents with constant viscosity η_s (e.g. water), $G_s^*(\omega) \equiv i\omega\eta_s$, and the final term is negligible for the experimental range of frequencies. The simplified form is

$$\frac{G_c^*(\omega)}{G_0'} = \frac{1}{i\omega\hat{\Pi}(\omega)}, \tag{4.5}$$

allowing the viscoelastic properties of the cell (normalised to G_0') to be

interpreted. Considering again the Generalised Stokes-Einstein Relation (GSER, Equation 2.14), the analogy between the bead attached to the cell and optical trapping microrheology can be seen. Attachment to the cell is analogous to optical trapping in that it limits the pseudo-Brownian motion of the bead to within an elastic trap.

The maximum frequency over which this is applied is the Nyquist limit, half the acquisition rate of the camera. High frequency data is, however, subject to errors in the numerical Fourier transform[16, 153]. The minimum frequency where the GSER is applicable is not determined by the observation duration (length of video recording in seconds) but by the cytoskeletal reorganisations within the cell causing the binding site of the bead to move. This movement, which is interpreted in Section 4.4.4, is why Equation 4.1 was stated as describing movement *relative* to the binding site.

4.4 Results

External passive microrheology control measurements were made on 11 HeLa cells and drug treatment measurements were made on 10 HeLa cells. The results from these experiments are structured as follows: first, interpretation of the MSD curves is considered with different processes attributed to the three distinct regions of the MSD curve visible in Figure 4.5. Secondly, the short-time (< 0.1s) dynamics are considered: by analogy to optical trapping the viscosity of HeLa S3 cells is found to be invariant under the experimental conditions. Intermediate time (~ 1s) dynamics are treated as elastic properties, while consideration of the increment distribution demonstrates the non-equilibrium nature thereof. Finally long time (> 10s) dynamics are quantified equivalently to either strain, or stress gen-
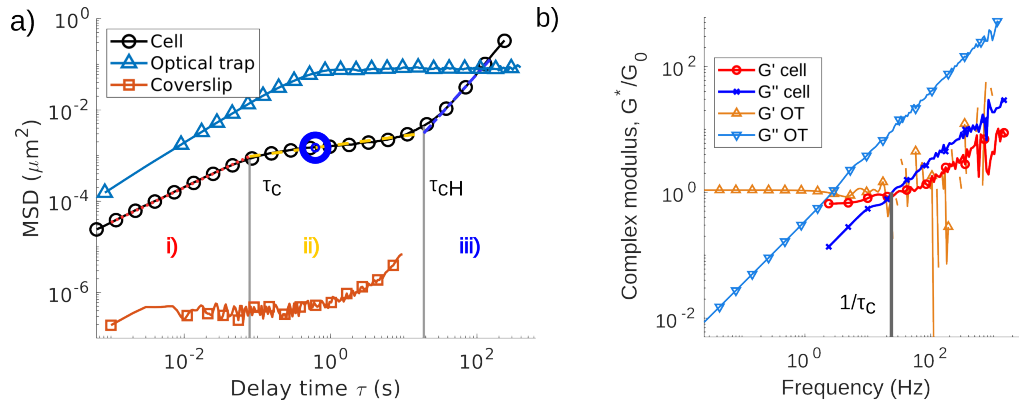
Figure 4.5: a) Example MSD and b) normalised complex moduli for bead attached to cell and optically trapped bead in water. Example MSD for a 5µm bead attached to a coverslip is included to demonstrate the noise floor of the system. Interpretation of the MSD, including the three regions labelled i-iii, is discussed in the text. Complex moduli are found using Equation 4.5. Figure reproduced from Hardiman et. al.[79].

eration by considering variation in elastic stiffness of the cells.

4.4.1 MSD Interpretation

Figure 4.5 shows an MSD curve representative of data acquired as described in Section 4.2; the MSD was calculated as described in Section 3.2.3.4. Also shown are MSD curves for an optically trapped bead in water and a bead attached firmly to a coverslip, demonstrating that the cell is less compliant than water but not too stiff for passive microrheology measurements. I will consider now the different time-scales and their characteristic dynamics, including quantitative analysis applying the methods demonstrated in Chapter 3. Values quoted here were taken from 33 measurements of beads attached to untreated cells.

At the shortest timescales within the experimental window, typically from $\sim 1\,\text{ms}$ to $\sim 50\,\text{ms}$ and labelled i) on Figure 4.5a, bead motion is sub-diffuse. Viscoelastic screening causes high frequency stress to dissipate

over shorter distances, thus shorter timescales probe relaxation over shorter length scales, i.e. locally to the adhesion site.

The mean power-law exponents (± standard deviation), found by fitting to Equation 3.18, were $\alpha = 0.6\pm0.2$ and 0.80 ± 0.09 in the radial and tangential directions, respectively. Noting the similarity between that and the expected power-law exponent of a semi-flexible polymer, $\alpha = 0.75$[157], the short-time MSD is assumed to probe molecular relaxation around the binding site, likely that of the cell membrane and actin cortex. Also note that for a Newtonian fluid (e.g. water), $\alpha = 1$.

At intermediate timescales, around 1s and labelled ii on Figure 4.5a, bead motion exhibits a weaker power-law scaling. By applying a 15-point rolling fit to the MSD curve (the mean number of points in the MSD curves for data presented here was 235), the lag time dependent power-law exponent, $\alpha(\tau)$ was estimated. A minimum in $\alpha(\tau)$ was typically observed at or around 1s with mean (± standard deviation) values of 0.2 ± 0.1 and 0.1 ± 0.1 in radial and tangential directions respectively. The minimum is circled in blue on Figure 4.5a. Noting now the prediction that micro-rheology probes longitudinal elastic modes at low frequencies[121, 124], and the prior experimental observation that the cytoskeleton exhibits a weak power law response typical of soft, glassy materials[23, 50]. The elastic plateau observed is thus assumed to probe relaxation of the cytoskeleton as a whole.

At long timescales, typically greater than 30 s and labelled iii) on Figure 4.5a, bead motion is super-diffuse. Superdiffusivity indicates non-thermal origins of the forces driving bead motion and a departure from Equation 4.1. Noting now both prior experimental observations of beads adhered to cell surfaces moving superdiffusely, and endogenous tracer motion being dominated by active strain fluctuations. The bead motion is assumed to

originate in cytoskeletal reorganisations coupled to the integrin receptors to which the bead has bound.

4.4.2 Viscosity and Elasticity

Now I consider quantifying the viscosity and elasticity probed at short to medium timescales (regions labelled i) and ii) on Figure 4.5). Recall the Kelvin-Voigt model for the optical trap as a viscoelastic solid in Section 2.2. Similarly the bead bound to the cell undergoes *pseudo*-Brownian motion and can be analysed using the same methods. Numerical analysis was performed as described in Section 3.2.4. The results are interpreted for Latrunculin-B treated cells compared to control cells, considering the viscoelastic properties of the cells.

By considering $\alpha(\tau)$, the elastic stiffness, $\beta G_0'$ (Equation 4.5), is taken to be reciprocal to the MSD at the minimum $\alpha(\tau)$. The characteristic relaxation time, (labelled τ_c on Figure 4.5) is found using both the time domain and frequency domain methods, and the average of the two values is used.

Figure 4.6a and b show the changes over a 40 minute window in the stiffness and relaxation times, respectively, for beads affixed to cells. Changes to the median of the drug treated group vs the control group are found to be significant with a Mann-Whitney u-test. The geometric stiffness, $\beta G_0'$, of control cells increased in almost all cases (median $\pm$ half inter-quartile range: $2\pm5\,\text{N/m}$,), while the drug treated cells become softer in almost all cases ($-4\pm5\,\text{N/m}$).

Considering Equation 3.4, I scale the reciprocal of the measured corner time, τ_c, by the viscosity of water, η_{water}. I scale the geometrical stiffness, $\beta G_0'$, by $6\pi a$, the standard geometric factor for a bead of radius a[117]. The
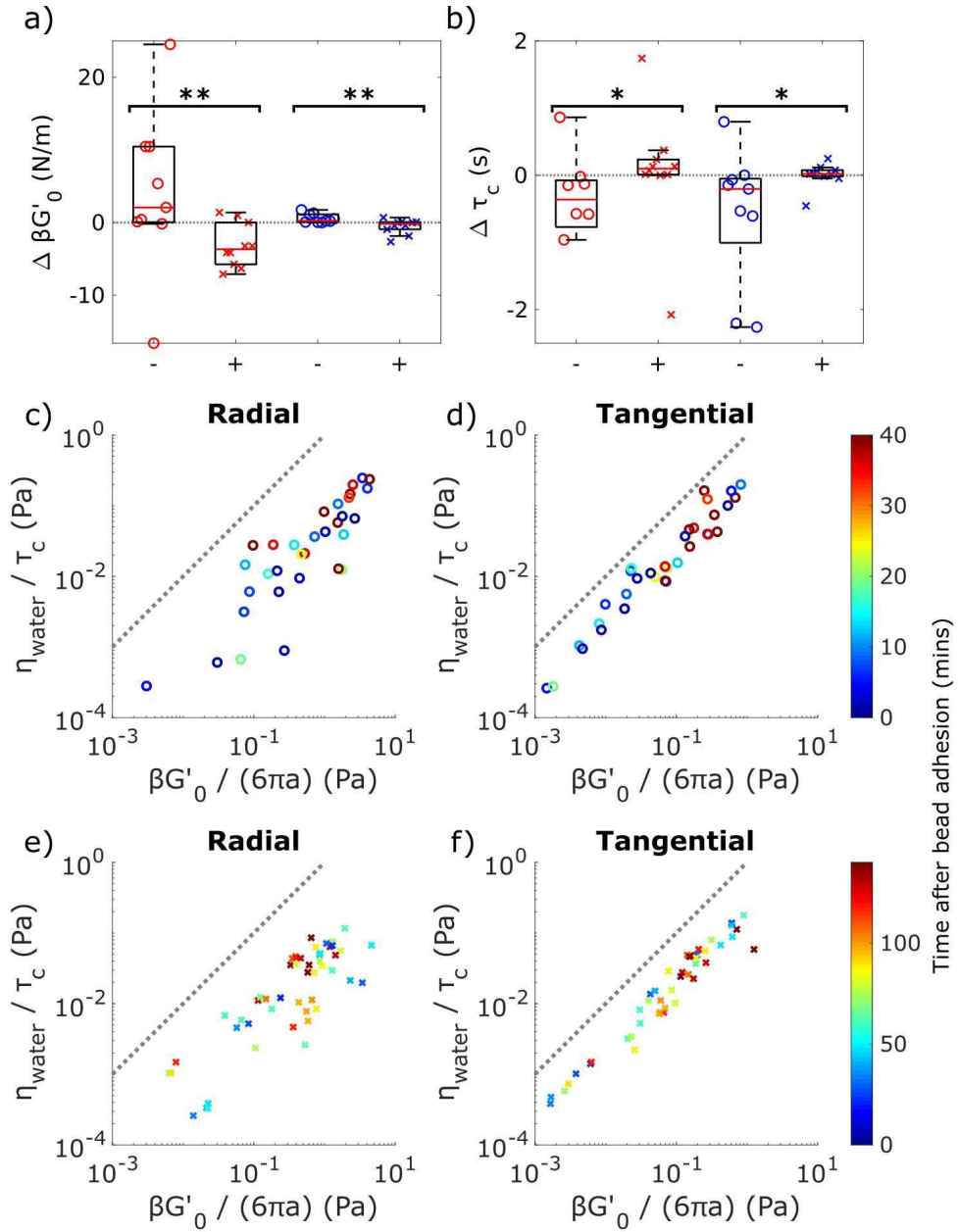
Figure 4.6: a,b) Boxplots of change over 40 minutes in geometric stiffness, $\beta G_0'$, and characteristic relaxation time, τ_c, respectively. Changes marked $*$ and $**$ are significant to $p \leq 0.05$ and 0.01, respectively, with a Mann-Whitney test. c-f) Scatter plots of geometric stiffness against characteristic relaxation time with scale factors as described in the text. Dashed lines are a guide showing the viscosity of water, with high viscosities appearing further below the dashed line. Note the different colour scales for the time after bead adhesion. Figure reproduced from Hardiman et. al.[79].

scaled corner time and geometric stiffnesses are plotted as the ordinate and abscissa, respectively, on Figure 4.6. Scaling the data thusly means that both axes have units of Pascals, analogously to the inset of Figure 3.11b. The prediction for corner time for a bead in water has been included as a dashed line, while an increased viscosity will shift the data points further below the prediction.

Figure 4.6 c-f show that both drug treated and control cells have the same constant viscosity. In the radial direction this is $23\,\eta_{water}$, and in the tangential it is $4\,\eta_{water}$. It can be seen clearly in the control case that measurements from later time points have a higher stiffness (further right), but do not diverge from the same viscosity. This observation strengthens the interpretation that the short time-scale probes molecular relaxation locally to the bead: even after the cytoskeleton has rearranged or been perturbed within the cytoplasm, up to microns away from the bead, the mechanical properties in the bead's millieu are unchanged.

4.4.3 Equilibrium Nature of Bead Motion

Increment distributions and the non-Gaussian parameter (NGP), as detailed in Sections 2.2.4 and 3.2.3.3, are useful to determine whether motion at a given time scale is an equilibrium process or not.

Accumulating data from different cells presents a challenge due to the discrete sampling of the time series: only lag times which are integer multiples of the frame time can be observed. (N.B. frame time is time between subsequent frames, or the reciprocal of frame rate. It is not necessarily the same as exposure time.) Thus for observations with different frame times there need not be any lag times in common.
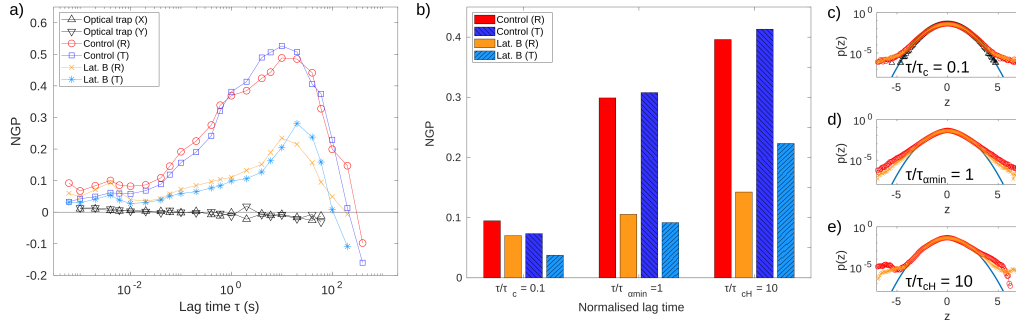
Figure 4.7: a) Non-Gaussian Parameter (NGP) as a function of lag time for control and Latrunculin B treated cells, and an optically trapped bead for comparison. The increment distributions transition from near-Gaussian at short lag times, to distinctly broad-tailed around $\tau = 10s$, indicates the contribution of non-equilibrium processes to bead motion. b) Bar graph of NGP for three select normalised lag times: one tenth the characteristic relaxation time τ_c, the plateau time $\tau_{\alpha min}$, and ten times the characteristic relaxation time τ_{cH}. Differences between the control and drug treated cells demonstrates the contribution of the actin cytoskeleton to the bead motion. c-e) Normalised increment distributions comparing the radial direction for control and drug treated cells at each of the three normalised lag times plotted in b). Figure reproduced from Hardiman et. al.[79].

To overcome this, I defined a single list of lag times common to all data sets. The increment distribution was calculated for each data set at the closest lag times to those in the common list. Even considering the first lag time, the difference between the true lag time and the lag time in the common list was less than 1% for almost all data sets.

Once the increment distributions were calculated, they could simply be added before being normalised to the total number of observations within each distribution to find the probability density as a function of normalised increment, $p(z)$. The accumulated increment distribution was then analysed to find the NGP as a function of lag time, shown in Figure 4.7a; included are control cells, drug treated cells, and an optically trapped bead for reference.

The NGP can be seen to be near-zero for both cell conditions at short

lag time. This indicates that the bead motion is thermally dominated with some contribution from nonequilibrium behaviour such as molecular motors or the glassy rheology of the cytoskeleton.

At lag times between 1s and 100s, the NGP for control cells diverges from that of drug treated cells. In both cases, the NGP indicates a broad-tailed increment distribution. At the longest lag times, the NGP drops sharply; this could be due to either the motion being dominated by a Gaussian-distributed force provided by molecular motors. Alternatively, the number of independent observations of each lag time may be inadequate for the NGP to accurately describe the bead dynamics.

The MSD curves, as discussed earlier, exhibit varying characteristic times for the crossover at short times (τ_c) and at long times (τ_{cH}). To better compare increment distributions for a given part of the MSD curve, three normalisations were employed before the increment distribution was calculated. The NGP using these normalised lag times is shown in Figure 4.7b, and increment distributions for these are shown in Figure 4.7c-e.

To inspect the short time data, τ_c was used as a normalisation factor, and the NGP at lag time equal to one tenth the corner time was considered. This reveals that control and drug treated cells have similar dynamics on the shortest time scales.

For the glassy plateau, the lag time of the gradient minimum, $\tau_{\alpha min}$, was used as a normalisation factor, and the NGP at lag time equal to the plateau time was considered. In control cells, the motion is dominated by the glassy rheology of the cytoskeleton, leading to a large value of the NGP. In cells where the actin cytoskeleton was disrupted, the NGP is only slightly increased compared to at short times indicating the alteration to the glassy rheology by disrupting the actin cytoskeleton.

Super-diffuse motion onsets at lag time equal to τ_{cH}, so this was used as a normalisation factor and the NGP at lag time equal to 10 times this onset time was considered as representative of the super-diffuse motion. Again this revealed a stark difference between the control cells and actin-disrupted cells (Figure 4.7b).

4.4.4 Active Strain Fluctuations

Active strain fluctuations were quantified by fitting to Equation 3.18. Only the tangential direction was analysed to prevent cell swelling or shrinking from affecting the measurement. Figure 4.8 shows results for control and latrunculin-treated cells.

The power law exponents, here named α_H to avoid confusion, are shown for the second time-point in Figure 4.8a. The change over 40 minutes in pseudo-diffusion coefficient, denoted ΔD_H, is shown in Figure 4.8b. This is interpreted as the strain rate of cytoskeletal reorganisation decreases in the control case and is roughly constant in the drug case.

Normalising the MSD curve to the plateau stiffness before fitting to Equation 3.18 yields the normalised pseudo-diffusion coefficient, denoted D_{GH}. Change over 40 minutes is shown in Figure 4.8c. The trend for control vs drug is now reversed, with control cells showing an increase over 40 minutes in D_{GH} while drug treated cells show a decrease.

To aid in interpreting this final result, recall that cells exhibit a slowly-evolving internal prestress (Section 2.1). Assuming linear elasticity with modulus G, the stress rate, $\dot{\sigma}$, is given by

$$\dot{\sigma} = \frac{\dot{\epsilon}}{G},\tag{4.6}$$

108
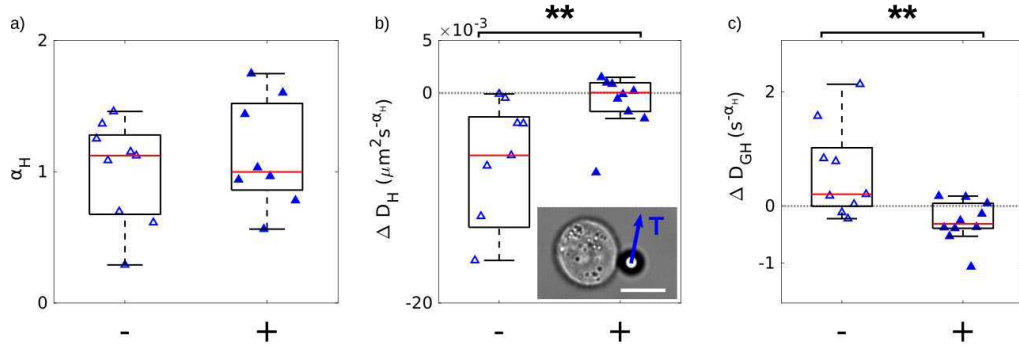
Figure 4.8: a) Long lag time power-law exponent, α_H, for second measurements (i.e. measurement 2 on Figure 4.4) of control and drug treated cells shows super-diffuse motion in most cases. b) Change in pseudo-diffusion coefficient for superdiffuse motion, D_H, shows a decrease in the control case and a median of no change in the drug treated case. c) Change in normalised pseudo-diffusion coefficient for superdiffuse motion, D_{GH}, shows an increase in the control case and a decrease in the drug treated case. Interpretation of these is discussed in the text. $**$ denotes changes are significant to $p \leq 0.01$ with a Mann-Whitney test. Inset: Image of cell with tangential direction labelled, $10\,\mu$m scale bar. Figure reproduced from Hardiman et. al.[79].

where $\dot{\epsilon}$ is the strain rate. Using this, the normalised pseudo-diffusion coefficient is interpreted as the stress rate of cytoskeletal reorganisation. In the case of control cells, the stress rate increases because integrin binding leads to cytoskeletal reorganisation. When the actin cytoskeleton is disrupted, the stress rate decreases. This interpretation is addressed further in the Discussion section.

4.5 Discussion

Work presented in this chapter has demonstrated, by analogy to optical trapping, the extension of passive microrheology to a bead chemically affixed to the surface of a cell. The MSD statistic and increment distributions were examined and interpreted, allowing quantification of live cells'

viscoelasticity over several hours.

Cell microrheology and active force generation of the cytoskeleton have previously been performed using beads adhered to cells[50, 69, 141], however these studies were designed to minimise the effect of binding site maturation on the measurements. This cellular response has, however, been studied using fluorescent microscopy[158], although there were no accompanying mechanical measurements.

Using the optical trap to carefully affix beads to the cells, and a fast camera to record bead position at over 1kHz, allows us to probe the viscoelastic properties at timescales down to 1ms; thus revealing the invariance in short-time viscosity of the cells under experimental conditions. By performing multiple measurements of changes to individual cells, each series has an internal control from the first measurement. This allows changes of cell mechanics over time to be examined in a way that is not possible for population measurements. The inherent low dose of laser light, coupled with the low powers use (tens of milliwatts) and choice of wavelength (1064 nm) ensure the biocompatibility of the method, necessary for such extended measurements.

4.5.1   Cellular Adhesion to Beads

Streptavidin-functionalised beads adhere to the cells via integrin receptors[159–161], a class of membrane proteins essential for mechanotransduction[38, 44]. The bead response function, or relation between applied force and bead displacement, depends on the receptor that is targetted[44, 50, 162, 163].

Binding beads to receptors such as integrins, which couple to the actin cytoskeleton, results in a characteristic strain-stiffening response[50, 162,

163]. Targetting integrins can be achieved by functionalising beads with fibronectin[69], the tri-amino acid sequence arginylglycylaspartic acid (commonly referred to as RGD)[50, 64, 141, 164], or streptavidin[159].

Beads functionalised to bind to scavenger receptors have also been used to investigate cell mechanics[50, 64], in which case the cell does not display the characteristic strain-stiffening response or actively driven motion. The receptor-dependent response is indicative of the coupling between integrin receptors and the cytoskeleton. Thus if the aim of the study is to probe the component of the cell which regulates mechanical properties and responds to mechanical stimuli[45], targetting integrin receptors is a good start.

It is known from cellular biochemistry that cells respond to ligands binding to integrins by recruitment cytoskeletal filaments such as vimentin and actin[36–38]. Beyond simply mechanical properties, it has recently been reported that binding micron-sized beads to cells results in cytoskeletal structures forming around the beads[158]. Images from this paper are shown in Figure 4.9, where three different cytoskeletal filaments have been imaged after a 3 hour incubation with the beads. The cytoskeleton has partially enveloped the beads, and 3D rendering of a confocal microscopy image stack (Figure 4.9b) highlights this. In the milieu of the beads, the microtubules have formed structures which stand out from the rest of the cell.

The study goes beyond simply imaging cells, and quantitative analysis reveals that the formation of these structures depends on the stiffness of the substrate that the cells were grown on and whether the beads were coated or not[158]. The authors comment that microrheology of these structures would be interesting, but do not report any such results.

Here I have measured changes in cell viscoelasticity following adhesion of streptavidin-functionalised beads to integrin receptors; this is inherently
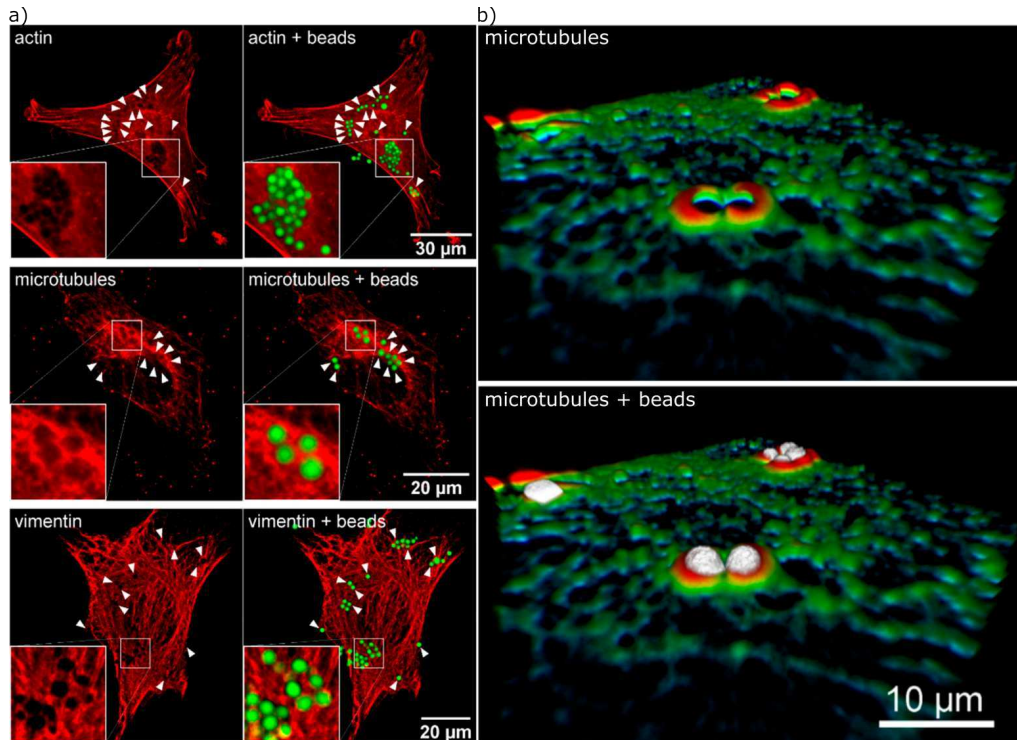
Figure 4.9: a) Mouse Embryonic Fibroblast cells were incubated with 2µm beads (green) before fixing and staining (red) for cytoskeletal filaments actin, microtubules, and vimentin. The cytoskeletal filaments can be seen to be more dense in the areas surrounding the beads. b) 3D rendering of microtubules coloured according to height (blue→green→yellow→red : low→high). Microtubule "cup" structures can be clearly seen enveloping the beads (white). Figure reproduced from [158].

either a physiological or pathological response depending on the exact circumstances under which the cell adheres to something. I posit that the bead adhesion will trigger the same signalling pathways as integrin-mediated adhesion of the cell to a surface such as a functionalised polymer or extracellular matrix. While Adamczyk used 3T3 murine fibroblasts[158] and I used HeLa human epithelial cells, each are naturally adherent cells and integrins are a highly conserved group of proteins[165]. Thus I posit that the physiological response to integrin binding will be similar.

Applying this prior knowledge of cellular, specifically cytoskeletal, behaviour suggests that focal complex formation is a possible mechanism for the stiff-

ening observed in the control case. This interpretation is reinforced by the increase in cytoskeletal activity seen from the active strain fluctuations. The cell softening, decrease in cytoskeletal activity, and trend towards Gaussian increment distributions seen when the actin cytoskeleton is disrupted therefore demonstrates the contribution of actin to the processes regulating these.

4.5.2   Analytical Framework

Quantitative analyses presented take the work beyond prior results published by Warren et. al.[1]. These prior results include verification of the analytical framework whereby a bead was bound to a polydimethylsiloxane (PDMS) cylinder (30 µm height, 15 µm diameter). The known geometry allowed the MSD to be related to the Young's modulus which was found to be in good agreement with literature values.

Prior passive microrheology studies have also reported cytoskeletal rearrangements causing super-diffuse motion ($\alpha_H > 1$) of beads bound to integrin receptors[64, 89, 90, 141]; these studies, however, did not report displacements over lag times less than a second and so could not quantify mechanical properties from passive measurements. Some studies have used the same beads to study both cytoskeletal rearrangement and cell viscoelasticity, however they were unable to do so simultaneously[50, 90, 141].

An increase in β, the geometric term relating the cell's microscopic memory function its shear modulus (Equation 4.3), corresponding to "tighter" bead binding would result in bead displacements being below the noise floor on millisecond timescales. A number of experimental datasets acquired has been disregarded due to this being the case. The criteria I used to discard

data was that the MSD at $\tau = 1s$ was less than $10^{-4}\mu\text{m}^2$ because this indicated that static error likely impacted the short-time data.

Notably, the unknown geometry means that we cannot quantify absolute value of elasticity, making it difficult to compare the elasticity probed to that reported by other techniques. Despite this, study of changes in viscoelastic properties and cytoskeletal activity over time is useful to develop greater understanding of cellular interactions with functionalised surfaces, and the interplay between the cytoskeleton, mechanical properties and endocytosis.

4.5.3 Cell Viscosity

Invariant viscosity of cells under treatment by various cytoskeleton-targetting drugs was previously reported by Fabry et. al.[166]. The values stated there, typically 1000 η_{water}, are clearly quite different from the values reported here (23 η_{water}). The cell shapes in either case are drastically different, with the HeLa S3 cells here shaped almost like water drops (shown by 3D confocal imaging in Figure 4.3), whereas the cells studied by Fabry are all "fried egg" spread out, adherent cells. Differences in cell morphology reflect differences in cytoskeletal organisation and prestress, but also mean that Faxén's law (Equation 3.5) may be needed to account for edge effects.

Comparative analysis of the internal viscosity of cells allows designation of two effective viscosities, which dominate depending on the length scale of the diffusing particle[96]. For particles smaller than the mesh size of the cytoplasm, a microscopic viscosity dominates, while larger particles are affected by a bulk viscosity. The value reported by Kalwarczyk for the bulk viscosity of HeLa cells, ~ 25 η_{water}[96], is similar to the viscosity reported

here, $23\ \eta_{water}$.

4.5.4 Cell Elasticity

Bead motion was interpreted through the framework of passive microrheology by applying the fluctuation-dissipation theorem, i.e. under the assumption the cell-bead system is in thermal equilibrium. Clearly this is not the case and life is a far-from equilibrium state. Previous studies, however, have shown that passive and active microrheology can yield the same modulus in active systems at sufficiently high frequencies[23, 167] ($\sim$10Hz for actin-myosin gels[167]).

Furthermore, inspection of position increment distributions reveals that motion is thermally dominated at the shortest times (< 0.1s), while the MSD power-law exponent, α lies in the range expected for a semi-flexible polymer network. At intermediate times (~ 1s), the non-equilibrium nature of the increment distributions and the weak power-law scaling of the MSD display characteristics of the glassy rheology of the cytoskeleton [23, 50]. Thus this technique probes mechanical properties on frequencies down to the onset of super-diffuse motion.

The elastic properties of the cytoskeleton likely derive from its organisation as a prestressed network, or tensegrity structure[3, 168–171]. Coupled with the concept of the soft glassy rheology (introduced in Section 2.1), a possible origin of the broad-tailed nature of the increment becomes apparent. Prestressed fibres with temporary cross-links (such as motor proteins) will relax in a non-continuous manner. Each time a cross-link "breaks", the filament undergoes a short, sharp relaxation – equivalent to hopping between potential wells in the glassy model. The distribution of these hops, driven

by stresses which are non-thermal in origin, gives rise to the increment distribution observed.

Consider now the transition from the glassy plateau to super-diffuse motion, and interpretation of active strain fluctuations. Recall that in a passive microrheology experiment, the MSD is proportional to the shear creep compliance, $J(t)$, in a step-stress experiment. In such an experiment, the strain is proportional to the creep compliance because the stress is constant. Now considering the cell results, for timescales where the glassy response dominates, the strain as a function of lag time can be written

$$\epsilon(\tau) = \sigma_t \; J(\tau) = \sigma_t \; \frac{\tau^\alpha}{\beta G_0'}, \tag{4.7}$$

where σ_t is the stress due to thermal fluctuations and α is the power-law exponent for the glassy plateau. For timescales where the cytoskeletal rearrangements dominate, the strain can be written

$$\epsilon(\tau) = \sigma_C(\tau) \; J(\tau) = \sigma_C(\tau) \; \frac{\tau^\alpha}{\beta G_0'}, \tag{4.8}$$

where $\sigma_C(\tau)$ is the time-dependent stress generated within the cytoskeleton.

At the characteristic timescale, defined as being when the strains of the two processes are equal, the thermal stress and cytoskeletal stress must also be equal. Reorganisations in the cytoskeleton may, however, change the cytoskeletal stress generation and the elastic modulus G_0'. Thus by normalising the MSD by the plateau height, which is reciprocal to the geometric stiffness $\beta G_0'$, the effect of changing stiffness can be removed. The normalised pseudo-diffusion coefficient for super-diffuse motion, D_{GH}, is therefore interpreted as being proportional to the stress rate within the cytoskeleton.

Now consider the implicit assumption of ergodicity in the derivation from the generalised Langevin Equation (Equation 4.1) to the generalised Stokes-Einstein Relation (Equation 4.5) used here. Ergodicity is typically defined as the convergence of ensemble-averaged and time-averaged MSDs, arising from spatio-temporal homogeneity. As demonstrated by the change over 40 minutes in elastic properties of the cell, the cell-bead system does vary over time.

The variation in mean-squared displacement over the duration of the video recordings used here is sufficiently small so as not to significantly effect the time-averaged MSD. This is exemplified in Figure 4.10, where a 10 minute long measurement (black line) has been broken up into 10 second windows before calculating the MSD of each individually and coloured according to the time they started at. Of the 63 short-time window MSDs, most are in good agreement with the long-time averaged curve. Also visible is the transient nature of some experimental noise, creating a ripple at the shortest times on the first two MSD curves (dark blue).

4.6 Conclusion

In this chapter, I have explained the microrheology method and analytical framework developed to probe live cells. Data were collected from a control condition and after disrupting the actin cytoskeleton by addition of latrunculin B. The MSD was interpreted and quantified by analogy to optical trapping and application of the methods developed in Chapter 3.

Using an optical trap to position beads on the surface of cells allows for some control over the geometric factor, β, which includes the adhesion strength. This, in turn, allows us to probe the complex modulus and cytoskeletal
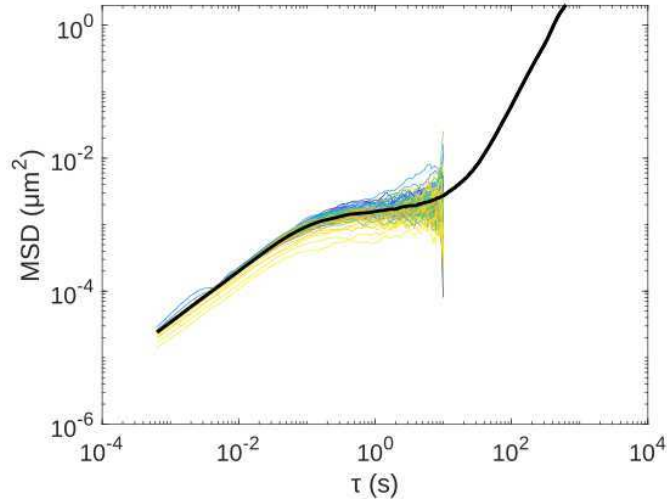
Figure 4.10: Black: MSD calculated from a single ten minute long video recording. Coloured blue to yellow: MSD calculated from ten second segments of the same data. Good agreement is seen between most of the MSD curves at short lag times where statistical significance is best, implying the system is near-ergodic over the ten minute recording.

rearrangements of the cell over a wider range of frequencies than have been previously reported from passive measurements with extracellular probes[1, 90].

Cell stiffening in the control case is interpreted as the effect of cytoskeletal activity in response to bead binding. Softening after treatment with Latrunculin B is interpreted as the effect of disrupting the actin cytoskeleton. In either case, the viscosity probed was found to be invariant. At intermediate timescales, examination of the increment distributions confirms the hypothesis that this technique probes the previously reported glassy rheology of the cytoskeleton[23, 50].

Interpretation of particle tracking statistics was discussed, including the issues of applying the fluctuation dissipation theorem and the effects of non-ergodicity in probing living systems. Again by consideration of the increment distributions, I show that short lag times are dominated by

thermal motion and thus the fluctuation dissipation theorem is applicable. Considering the variation in the MSD over a ten minute recording, I show that non-ergodicity is of little concern when probing these slowly-evolving systems. This opens the way for more living cell microrheology study, something which has previously been described as *"not an option"* because the observation times required for good statistics are sufficiently long that cell active motion dominated[172]. Here I have shown that living cell microrheology *is an option* because while the bead motion is dominated by active strain fluctuations at the longest lag times, the viscoelastic properties dominating motion at short timescales are vary slowly enough for a time-average to give a good indication of their values.

Strain due to cytoskeletal rearrangement was seen to decrease in the control and increase in drug treated cases. Using the elastic modulus to normalise the MSD data allows us to show, for the first time, that the converse is true for cytoskeletal stress generation. That is, the stress generation increases in the control case and decreases in the drug treated case. This finding would not be possible with other techniques as they are limited to either observing the active strain fluctuation or the elastic modulus, not both simultaneously. The technique, and interpretation of surface-attached rheology results, shows promise for application to studying a variety of interesting biological questions such as the dense extracellular matrix in some tissues or the interaction of cells with chemically functionalised surfaces.

Chapter 5

Phonon Microscopy

5.1 Introduction

Phonon microscopy, a form of time-resolved Brillouin scattering (Section 2.3.2.1), offers imaging of opto-acoustic properties with optically limited lateral resolution and axial resolution limited by acoustic wavelength. The temporal resolution for cellular changes is limited by the scanning protocol. This allowed study of cellular elasticity with greater spatial and temporal resolution than the microrheology results presented in Chapter 4.

The technique was developed by Pérez-Cota et. al.[2, 173, 174] using a femtosecond pulsed laser to excite a coherent strain pulse from a thin film transducer, and a second laser pulse to detect the strain pulse as it travels through the sample. The use of a coherent strain pulse increases scattering efficiency when compared to spontaneous Brillouin scattering; this means thermal phonons do not contribute to the signals collected.

Prior live cell study with phonon microscopy has been limited by poor bio-compatibility. Previous publications report using UV pump beams, giving

better signal to noise ratio and lateral resolution[2, 94], but phototoxicity and heating effects limited long-term live cell imaging. Results presented here consist the first biocompatible phonon microscopy measurements of live cells, including my demonstration of a lethal dose study which was also published in the *Journal of Applied Physics* as part of the publication "Picosecond Ultrasonics For Elasticity-Based Imaging And Characterization Of Biological Cells"[67].

The goal of the work in this chapter was to study cytoskeletal perturbations in live cells, with both spatial and temporal resolution. The cytoskeleton regulates mechanical properties of the cell and different cytoskeletal components follow different spatial distributions; this in mind, I aim to address the question: do cytoskeletal perturbations cause changes in mechanical properties localised to subcellular regions?

This chapter first details the experimental setup and analytical methods used for phonon microscopy. This includes summaries of signal processing methods which were developed and implemented by other members of the Optics and Photonics Research Group[2, 174, 175]. Methods I developed here are the Gaussian mixture model analysis, the live cell scanning protocol and analysis method for fluorescent determination of cell death.

5.2 Methods

5.2.1 Setup

The phonon microscope is built around an inverted microscope body to improve ease of use. Measurements are performed in a transmission geometry, as shown in Figure 5.1, which sets it apart from other picosecond
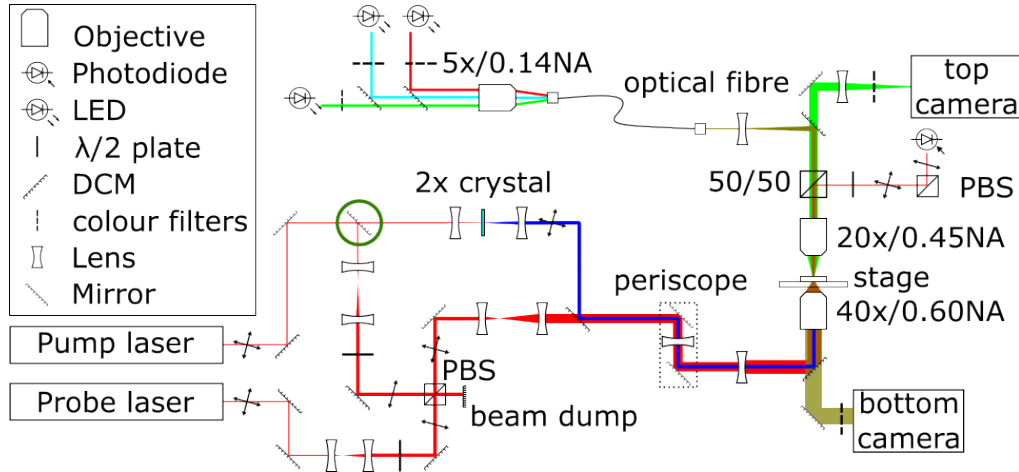
Figure 5.1: Phonon microscope optics diagram described in detail in the text. Briefly, the two lasers are overlapped and focussed to a point within the sample, which is moved relative to the beams. Laser polarisation shown with arrows. Transmitted signals are collected by a photodiode. LEDs allow for bright-field and fluorescent imaging. PBS: Polarising beam splitter. DCM: Dichroic mirror.

laser ultrasound techniques. This has the advantages of not needing to align counter-propagating beams and is made possible by the semi-transparent transducer[93]. Each beam has independent power controls before being delivered to the sample via a common path for ease of alignment. Cameras above and below the sample can capture brightfield images, and the top camera can be configured to capture fluorescent images.

The signal generation optics consist of two pulsed lasers ($\lambda =$780 nm, pulse duration 150 fs, MENLO Systems GmbH, Germany) are configured as described in Section 5.2.1.1. Each beam passes through beam expanders and half-wave plates before being combining with orthogonal polarisations at a polarising beam splitter (PBS), allowing independent control of the two beam powers. The pump beam may alternatively pass through a doubling crystal to create a $\lambda =$390 nm beam which is combined with the probe at a dichroic mirror, which is re-imaged onto the back focal plane of the 40× objective by a 4f system.

The optical setup has been designed to ensure ease when changing from "red-red" mode with both pump and probe at 780 nm, and "blue-red" mode with 390 nm pump and 780 nm probe simply by removing a mirror, circled in dark green. Blue-red mode has better transverse resolution due to the smaller focal spot of the pump laser[174], however UV radiation transmitted through the transducer makes it less suitable for live cell imaging.

The 40× objective focuses both laser beams to a diffraction-limited spot in the sample, typically in the sample holder described in Figure 5.2, which sits on a motorised X-Y stage for raster scanning. A 20× objective lens above the sample collects transmitted laser light and a polarising beam splitter delivers the probe light to a photodiode for detection.

Fluorescent imaging has allowed for lethal dose studies in live cells, and could also be used to localise sub-cellular structures such as the nucleus. Illumination is provided by LEDs, each spectrally filtered before combining at a low-NA objective which couples the light into a multimode optical fibre. The fibre delivers light to the overhead optical rack (Figure 5.2) where it couples to an objective above the sample for epifluorescence imaging. A multi-band dichroic and a separate multi-band emission filter prevent excitation light from reaching the top camera. Optical transmission images can be taken simultaneously using the bottom camera.

5.2.1.1 Pump-Probe Technique

Phonon microscopy falls into the broad category of pump-probe optical techniques; such techniques are often used to study ultra-fast physical phenomena[176, 177]. Sweeping the delay between the two pulses allows dynamics to be studied with picosecond resolution.
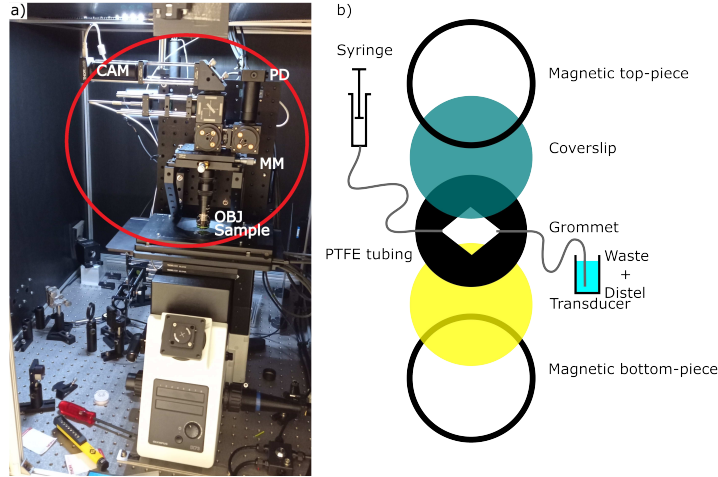
Figure 5.2: a) Phonon microscope, built around inverted microscope body with motorised sample stages. Circled in red is the overhead optics rack mounted on 3-axis micrometers (labelled **MM**) containing top objective (**OBJ**), photodiode (**PD**), fluorescent camera (**CAM**) and LEDs (mounted on the back of the rack, out of sight). b) Schematic of sample holder consisting of two magnetic rings which hold together two 25 mm coverslips separated by a rubber grommet. Tubes can be connected to syringes to deliver cell media and/or drugs and take outflow to a beaker containing distel for decontamination.

Two 150 fs duration pulsed lasers in Figure 5.1 are configured with relative timings locked in a setup known as AsynchronouS OPtical Sampling (ASOPS). The pulse repetition rates are ~100 MHz, locked with a difference frequency of 10 kHz. The delay between a pump pulse and a probe pulse is thus swept through a 10 ns range every 100 μs.

In other words, at $t = 0$ the pump and probe pulses are coincident; the second pump pulse arrives at $t = 10$ ns, while the second probe pulse arrives at $t = 10.001$ ns; thus the 10^4th pump pulse is also coincident with a probe pulse. To achieve a the 10 ns time window used here using a free space delay line would need 1.5 m of travel. Thus using ASOPS allows data acquisition rates that would be impossible with a delay-line based technique which requires mechanical parts to scan the delay time.
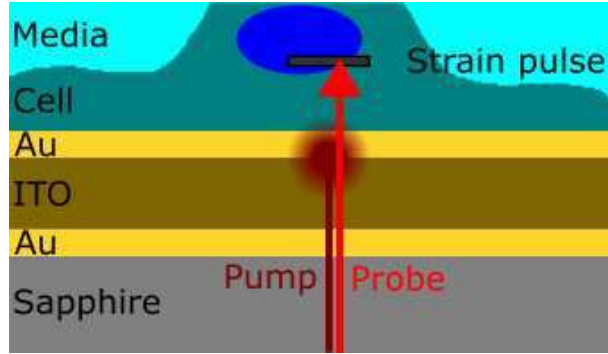
Figure 5.3: Experimental Setup for Phonon Microscopy
A multilayer thin-film transducer, coated onto a sapphire substrate, is excited by a pump laser pulse. The induced strain pulse travels through the sample where it is detected by a probe laser pulse. Pump and probe shown with lateral offset for clarity.

5.2.1.2 Opto-Acoustic Transducers

All results presented here were obtained using sapphire as the substrate for coating the thin-film transducer, which was deposited by sputter coating. Sapphire was chosen as its thermal conductivity is over $50\times$ that of glass. Finite element modelling of phonon microscopy has predicted that the temperature rise at the focal spot of a transducer on glass is roughly $60\,°C$, compared to $30\,°C$ for a transducer on sapphire[93].

The transducer design was selected, based upon published models[175], to be an optical cavity with metal and dielectric layers (gold-indium tin oxide (ITO)-gold), as shown in Figure 5.3. Transducer dimensions are a trade-off between thinner transducers with better transmittivity, and thicker transducers which are more robust and can be fabricated more reliably. Thicker transducers absorb more of the pump light, and hence generate greater sound amplitudes but also more heat.

Transducers were fabricated by me using sputter coating and verified by white light spectroscopy. Details of the methods are not included within this chapter as they do not comprise my own work. Instead, they have

been included in Appendix C for completeness. The dimensions used have varied between experiments but are listed in Table 5.2.

5.2.2   Time-Resolved Brillouin Scattering

Picosecond laser ultrasonics (PLU) is the study of coherent acoustic pulses (CAPs) generated by pulsed laser. In onesuch technique called time-resolved Brillouin scattering (TRBS), the CAP is interrogated using a second laser pulse. This may appear similar to stimulated Brillouin scattering due to the use of coherent phonons, however the interaction volume of Phonon microscopy is limited by the axial lengh scale of the CAP, leading to greater contribution from higher wavenumber phonons than in stimulated Brillouin scattering.

To generate CAPs, a pulsed laser is typically focussed onto a metallic film in contact with the sample. Absorption of the laser pulse leads to thermal expansion, and a strain pulse is launched into the sample. Use of short laser pulses limits the effects of relaxation processes (e.g.: thermal and electron diffusion), allowing higher amplitude, shorter duration strain pulses[178]. The bandwidth of the CAP is determined by the damping of the transducer resonance, typically on the order of a hundred gigahertz. After excitation with a laser pulse, the transducer resonance will contribute to the signal for the first few hundred picoseconds to nanosecond.

To detect CAPs, a time-delayed laser pulse is used, hence interacting with the CAP after it has had time to propagate within the material. Consider a CAP propagating within an isotropic and homogenous half-space, and an incident pulse of light, shown schematically in Figure 5.4a.

The strain wave acts like a weak mirror due to the photo-elastic effect,
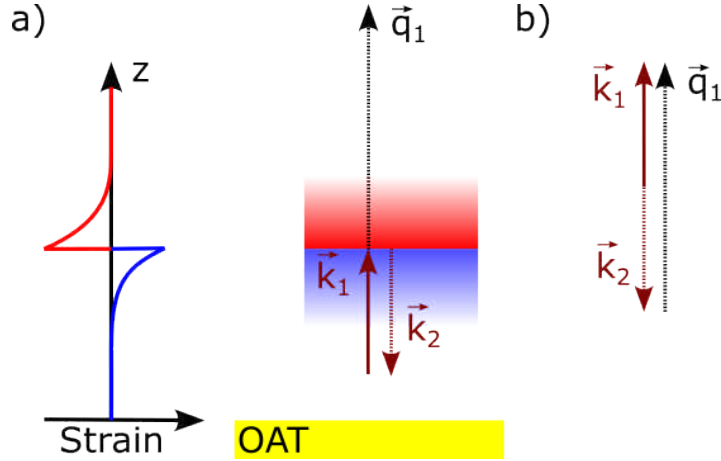
Figure 5.4: a) Spatial profile of strain pulse shown as a graph and as background colour. The opto-acoustic transducer (OAT) has launched a strain pulse which acts as a weak mirror. Incident and reflected light wavevectors are denoted $\vec{k}_1$ and $\vec{k}_2$, and phonon wavevector is denoted $\vec{q}_1$. b) Momentum conservation requires creation of a phonon travelling in the z direction with $\vec{q}_1 = \vec{k}_1 + \vec{k}_2$.

whereby material strain causes perturbations in the electric field permittivity[179]. The interaction between the probe light and strain results in transient changes in the electric field reflectivity,

$$\frac{dr(t)}{r} = -iC \int_0^\infty \epsilon(t, z) e^{i2kz} dz, \tag{5.1}$$

where $\epsilon(t, z)$ is the strain in the z direction, which may vary in space and time, and k is the complex wavenumber of the probe light in the medium. The constant term outside of the integral, C, is a sample-dependent complex constant proportional to the acousto-optic interaction strength[180, 181], related to the photelasticity tensor[179]. The bandwidth of the CAP, or equivalently the Fourier amplitudes of $\epsilon(t, k)$, is determined by the damping of the transducer resonance, typically on the order of a hundred gigahertz. After excitation with a laser pulse, the transducer resonance will contribute to the signal for the first few hundred picoseconds to nanosecond.

From Equation 5.1, it can be seen that transient changes in reflectance give information about the time-evolution of the strain pulse. Considering the velocity of the light relative to the strain pulse, the interaction can be described as quasi-static; that is, the time-evolution of the strain pulse is much slower than the duration of the interaction. For CAPs propagating linearly, as is the case in phonon microscopy, the shape of the spatial profile does not vary as the CAP propagates and attenuates[182].

The length scale of the CAP, l_a, is determined by the limiting factor out of the optical absorption depth, $\zeta_0(\lambda)$, and the thickness of the metallic film, and the pulse duration of the pump light. For short pulses such as used here the effect of pulse duration can be ignored. For a pulse of $780\,\mathrm{nm}$ light incident on a $21\,\mathrm{nm}$ gold film[183], the absorption length scale can be approximated as $l_a \sim 2\pi\zeta_0 \sim 80\,\mathrm{nm}$[178].

Consider now the optical paths of light incident upon the strain pulse shown in Figure 5.5. The scattered beam, reflected by the strain pulse, is then reflected again by the transducer[184]. Due to the weak reflectance of the strain pulse, light multiply reflecting and scattering between the strain pulse and transducer (dashed line in Figure 5.5) can be neglected.

When both reference and scattered light are focussed on a detector (e.g. photodiode), they will interfere due to their phase difference,

$$\Delta\phi = 2k\Delta z \ = 2kV\Delta t, \tag{5.2}$$

which depends on Δz, the "length of flight" of the strain pulse, or equivalently $V\Delta t$, the speed of sound in the medium multiplied by the time of flight. In both cases, λ is the wavelength of light in the medium. This
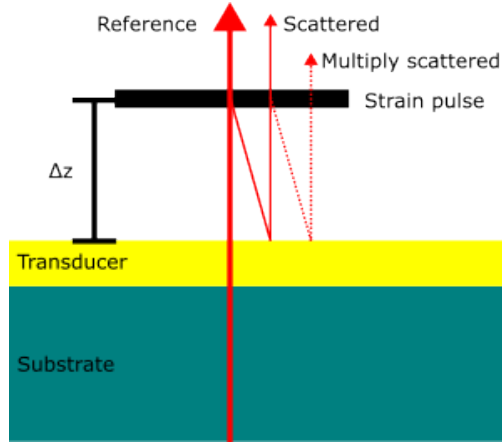
Figure 5.5: Beam paths in phonon microscopy. A strain pulse causes partial reflection of the probe beam, and the reflected light (shown with lateral offset for clarity) will arrive at the photodiode with a phase difference relative to the reference light giving rise to interference. The low reflectivity of strain pulses means multiple scattering events (dashed line) can be ignored.

phase difference varies in time according to

$$\frac{d\Delta\phi}{dt} = 2kV = 2\pi\nu_B,\tag{5.3}$$

thus intensity at the photodiode will oscillate at a frequency determined by the Brillouin frequency ν_B (Equation 2.27).

5.2.3   Signal Processing

The light intensity at the photodiode is converted into an electrical signal comprised of a near-constant (DC) component and a time-varying (AC) component. The DC signal is simply the transmission of the probe light through the sample, and can be considered similarly to an optical image. It is also used to calculate the modulation depth by dividing the AC signal by the DC signal, in which case the amplitude of the Brillouin oscillations give an indication of the amplitude of the strain pulse and the photoelastic constant.

The AC signal, meanwhile, has several components arising from different mechanisms. An example raw trace is shown in Figure 5.6a, with the following features visible: i) coincidence peak caused by light-electron interactions; ii) thermal decay; and iii) Brillouin oscillations. Digital signal processing is performed in MATLAB using the code developed for prior published works[2, 173] to extract the Brillouin oscillations, resulting in the time trace shown Figure 5.6b.

For detection, the electrical signal is divided into an AC and a DC component using a highpass filter, and the two are digitised separately. The DC signal is connected to an analogue-to-digital card (NI-PCI 6221), while the AC signal is connected to a digital oscilloscope (Teledyne Lecroy) which performs both digitising and averaging before sending the voltage-time signal to the PC for storage and later analyses.

The processing comprises of first finding the coincidence peak by searching for points exceeding a threshold value. Next, a user-set number of points after the peak are discarded (90 in this example). Then a user-set number of points are taken for further processing (2100 in this example).

A digital low-pass filter is then used to remove high frequency noise. In this example I have used $8.5\,\mathrm{GHz}$ as the stop frequency because the signal of interest is between 5 and 6GHz. Finally the trace is fitted to a low-order polynomial to remove the thermal response.

The signal as shown in Figure 5.6b encodes the instantaneous phase shift of the scattered light from a depth of roughly $6\,\mathrm{\mu m}$, assuming a homogenous sound velocity of $1.5\,\mathrm{\mu m/ns}$ (the speed of sound in water). This signal is manually cropped in the time domain according to the lifetime of oscillations seen in a given experiment. In this case, I would crop at 3ns for further processing, but have included the noisy tail of the signal for
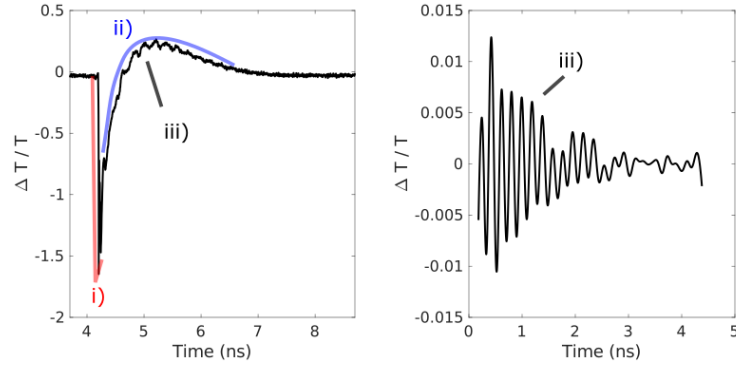
Figure 5.6: a) Raw AC signal from water comprised of i) coincidence peak, ii) thermal response with iii) Brillouin oscillations overlaid. b) Brillouin oscillations extracted from trace by digital signal processing.

illustrative purposes.

From the Brillouin oscillations, the basic processing is to use a Fast Fourier Transform to calculate the dominant frequency within the trace. This is equivalent to taking the weighted average frequency through the depth of the cell, weighted by the signal amplitude (which is maximum at the beginning of the trace).

5.2.3.1 Axial Reconstruction

The theoretical axial resolution of time-resolved Brillouin scattering is limited by the length scale of the acoustic pulses; practically it is limited by the signal processing. To recover axial information from a PLU time trace, a wavelet transform was first demonstrated by Dehoux et. al.[185]; the wavelet transform is used here as demonstrated by Smith et. al.[174]. I shall now summarise the analysis method in order to consider the achievable axial resolution.

To achieve axial resolution, a measure of the Brillouin frequency as a function of z is required. Assuming a constant sound velocity, this is equiva-
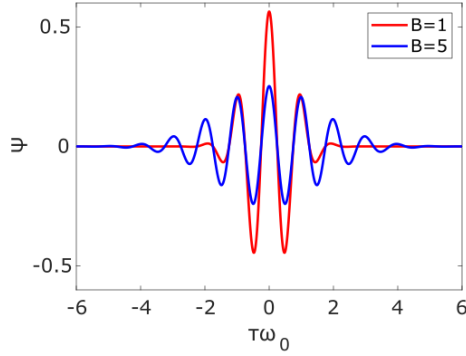
Figure 5.7: Magnitude of Complex Morlet wavelet defined in Equation 5.5 plotted against dimensionless time $\tau\omega_0$, for bandwidth parameter $B = [1, 5]$.

lent to resolving the Brillouin frequency in the time domain which can be achieved using continuous wavelet transforms, available from the Wavelet Toolbox in MATLAB. The transform can be written as a convolution of the signal, $T(t)$,

$$W_\psi(a, b) = \frac{1}{\sqrt{a}} \int_{-\infty}^{\infty} T(t)\psi\left(\frac{t - b}{a}\right) dt, \tag{5.4}$$

with the mother wavelet, $\psi(\tau)$, as a function of dimensionless time τ. Here a and b are the dilation and shift of the wavelet, respectively. The wavelet transform of a one dimensional signal such as a time series is a two-dimensional map of the amplitude, W_ψ, at a given frequency (or dilation a) as a function of the signal time (or shift b). From this, the frequency with maximum amplitude is extracted for each time in the trace.

For results presented here, the mother wavelet used was a the complex Morlet,

$$\psi(\tau) = (\pi B)^{-1/2} \; e^{2i\pi\omega_0\tau} \; e^{-\tau^2/B}, \tag{5.5}$$

where ψ is the value of the wavelet with wavenumber ω_0 and bandwidth B evaluated at non-dimensional time τ. The wavelet is shown for bandwidths $B = [1, 5]$ in Figure 5.7.

The resolution of the axial reconstruction is dependent on the bandwidth of the wavelet used. A higher bandwidth means there are more cycles before the wavelet has decayed - this essentially performs temporal averaging of the signal. The result is better frequency precision, but worse axial resolution.

5.2.4 Interpretation of Brillouin Frequency

Once a spatial map of the Brillouin frequency (a 2D image by basic processing or a 3D volume with axial reconstruction) has been determined, it can be interpreted in terms of the opto-acoustic interaction. This allows comparison with other techniques. The nanosecond time scales probed are around 6 orders of magnitude less than those probed by microrheology – at gigahertz frequencies, both cells and water behave as elastic solids. The Brillouin frequency can be thought of as analogous to an elastic stiffness, with stiffer materials having higher Brillouin frequencies, although it is actually more akin to compressibility.

Recalling the definition of Brillouin frequency for a homogenous material, Equation 2.27, it can be shown that

$$M' = \left(\frac{\nu_B \lambda}{2n}\right)^2 \rho, \tag{5.6}$$

where ν_B is Brillouin frequency, λ is vacuum wavelength of the probe light (780 nm), n is refractive index, and ρ is mass density of the medium.

For Hela cells, the cytoplasm has $n = 1.3716$, while the nucleus has $n = 1.3554$[186]. The density of cytoplasm is around $1050 \, \text{kg/m}^3$[187].These are comparable to the values for water ($n = 1.33$, $\rho = 1000 \, \text{kg/m}^3$), so for all conversion between Brillouin frequency and longitudinal modulus, the

values for cell are used - thus the longitudinal moduli reported for cells should be accurate, while the values reported for water will be higher than the actual values by $< 2\%$.

5.2.4.1   Role of Cellular Heterogeneity in Brillouin Scattering

The cytoplasm (shown in Figure 5.8), far from being a homogenous viscoelastic fluid, contains many structures such as mitochondria, endosomes and filamentous cytoskeletal proteins[4]. Each in isolation can be expected to exhibit its own distribution of Brillouin frequencies due to acoustic resonances of the structure. Individual reconstituted proteins exhibit glassy relaxation, characterised by slow collective modes known as α-relaxations and faster local dynamics known as β-relaxations. While the former are largely independent of intermolecular interactions, the latter are strongly influenced by hydrogen bonding and macromolecular crowding[188–190]. To better understand the role of molecular relaxation on Brillouin frequency measurements, one can turn to mode-coupling theory which describes how collective motion of macromolecules depends local deformations exploring the conformational space[191]; this framework has been extensively applied to glass formers and other non-equilibrium soft matter[192].

The glassy relaxation of individual macromolecules bears striking resemblance to the glassy rheology of whole live cells when subjected to small strains. In fact, it has been shown that the glassy rheology of the cytoplasm is intrinsic to its crowded nature and not limited to live cells[97, 193]. This model describes stress relaxation of cells for timescales of microseconds to whole seconds[23, 63, 88, 166], much greater than that of the β-relaxation which is on the order of picoseconds for reconstituted protein at room temperature[189]. This can be slowed by dehydration or cooling, in which
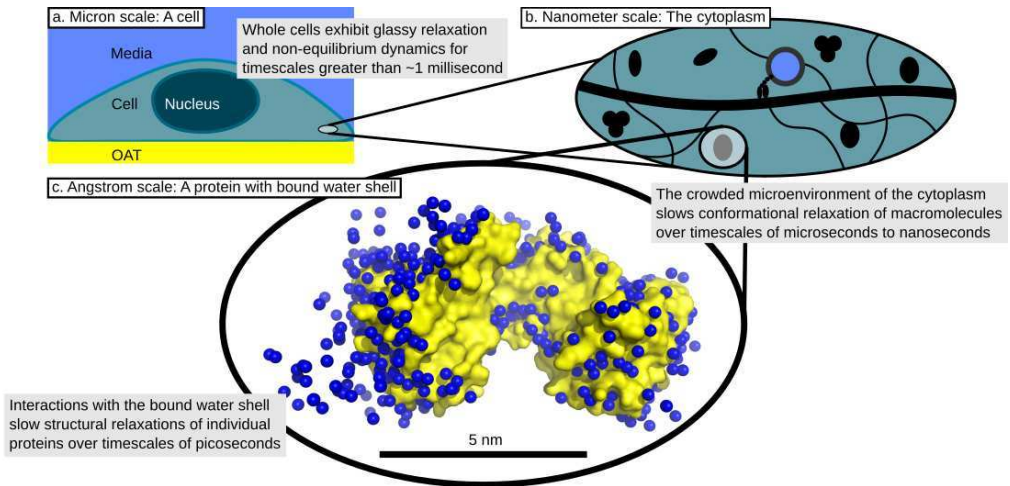
Figure 5.8: Multi-scale schematic of stress relaxation within living cells. For length scales greater than a few nanometres (i.e. a. and b.) stress relaxation is slow and glassy, predominantly being determined by macromolecular crowding. c. Individual proteins (yellow) also exhibit faster local relaxation driven by interactions with nearby water molecules (blue).

case the Brillouin frequency may exhibit a phase transition[108].

The gigahertz Brillouin frequencies reported here for live cells fall in the regime where α-relaxation dominates. The optical setup and signal processing employed in phonon microscopy essentially performs spatial averaging of the opto-mechanical properties across a lateral dimension determined by the optical spot size ($\sim 1\,\mu m$) and axial dimension determined by the acoustic wavelength ($\sim 400\,nm$), thus giving higher resolution than External Passive Microrheology. Variations in both density and refractive index of cells are small, with the cytoplasm having refractive index $\sim 2\,\%$ greater than that of the nucleus[186]. Since Brillouin frequency variations are larger than this, the contrast in phonon microscopy originates from differences in longitudinal modulus of the cell, itself determined by the glassy relaxation of the cytoplasm.

5.2.5 Gaussian Mixture Model

Quantifying contributions to the overall frequency map of the cell from different material components is possible with the use of Gaussian mixture models (GMM)[194, 195]. The model assumes each sample comprising the signal is randomly sampled from a finite number of normal distributions, and these distributions can be estimated by fitting a composite probability distribution to the observed distribution.

A Gaussian probability distribution function is defined below in Equation 5.7, and for a 2-GMM the composite probability distribution function is defined in Equation 5.8:

$$f(\nu|\mu,\sigma) = \frac{1}{\sqrt{2\pi\sigma^2}} e^{-\frac{(\nu-\mu)^2}{2\sigma^2}}, \qquad (5.7)$$

$$P(\nu|p,\mu_i,\sigma_i) = f(\nu|\mu_1,\sigma_1)p + f(\nu|\mu_2,\sigma_2)(1-p), \qquad (5.8)$$

where $f(\nu|\mu,\sigma)$ is the probability density, at frequency ν, for a Gaussian distribution with mean μ and standard deviation σ, and p is the mixing fraction for a two-Gaussian mixture model parametrized by $\mu_i = \binom{\mu_1}{\mu_2}$, $\sigma_i = \binom{\sigma_1}{\sigma_2}$. Similarly, an n-Gaussian mixture model can be defined for modelling a signal with n different components.

5.2.6 Lethal Dose Study Design

Understanding the biocompatibility of phonon microscopy was a key step towards live cell study. This section details scanning protocol and use of fluorescent dye to track cell death. The scan protocol was designed with the motivation of maximising the data collected from a single sample of cells while reducing exposure to avoid damaging the cells. Due to the long
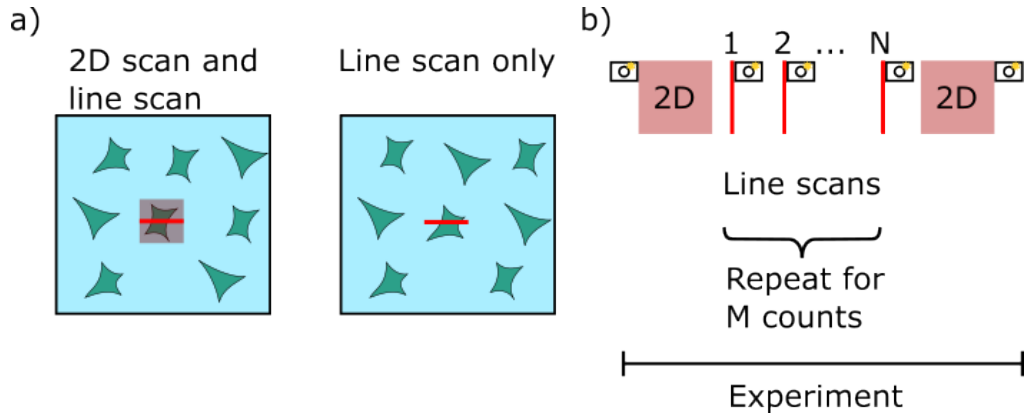
Figure 5.9: Live cell protocol: First, N cells are chosen for scanning which are sufficiently far apart that the fields of view on the fluorescent imaging do not overlap. a) One cell is subject to both 2D imaging and line scanning, the rest are only subject to line scanning. b) The scan timeline starts with a 2D image of cell 1, before repeating line scans of all the cells for a number of counts. Finally a 2D image of the first cell is taken again. At the beginning of the experiment, after every line scan, and at the end of the experiment, a fluorescent image is taken (denoted by the camera picture).

acquisition times (>1 s per pixel), live cells do not show many high-contrast internal features on phonon microscopy, so I opted to perform line scans on most cells to reduce exposure. This also reduces the time to scan each cell, meaning the temporal resolution of the experiment (defined as the time between successive line scans on a given cell) is typically 10 minutes.

Figure 5.9 shows a schematic of the protocol. A number of cells are chosen for scanning (denoted N), and the co-ordinates recorded. The scan begins with a 2D image of one cell, before doing a line scan of each cell chosen. The line scans are repeated for a number of counts (denoted M), before a 2D image of the first cell is collected.

To measure cell death, I used calcein-AM to indicate live cells; it is a cell-permeant dye, only fluorescent after being activated by esterase activity within the cytoplasm. Before the first 2D scan, after every line scan and after the final 2D scan, a fluorescent image was taken.
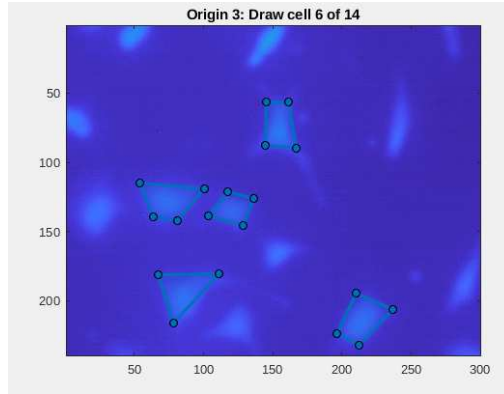
Figure 5.10: Calcein-AM fluorescent image of live cells on the phonon microscope with axis labels in microns, showing the manual segmentation process.

The signal to background ratio for a live cell steadily decreases due to photobleaching, while cell death is characterised by a sharp drop in fluorescence intensity. Thus fluorescent images enabled quantification of death time so the Brillouin frequencies of live and dead cells could be distinguished.

To analyse the fluorescent images first they were manually segmented as shown in Figure 5.10. Quite simply the cell positions were judged by eye and polygons were drawn around the cells. A polygon was also drawn for a background region. The polygons were used to create masks and the average fluorescent intensity of each region (i.e. each cell and the background) were calculated. The cells only moved and changed shape a small amount during the experiments so each field of view only needed manually segmenting once.

The camera used for fluorescence has an auto gain feature that cannot be turned off, leading to variable background brightnesses. To overcome this, the signal to background ratio was used for further analysis - I will refer to this as fluorescent intensity. When a cell is alive, the fluorescent intensity decays exponentially; when the cell dies, the fluorescent intensity has a sharp drop, followed by another slow decay. These are all visible on the

fluorescent trace in Figure 5.14a.

5.3 Results

5.3.1 Fixed Cell Results

Fixed HeLa cells were prepared as detailed in Appendix B and experiments were performed to investigate the effects of cytoskeleton-targetting drugs on HeLa cells. Two drugs were trialled: Cytochalasin D, an actin polymerisation-inhibiting drug, and Nocodazole, a microtubule depolymerizing drug. For each condition, 6 cells were scanned. All cells imaged were well spread indicating they were healthy before treatment and fixation. Optical images before and after scanning confirmed that there was no damage to cells due to heating. Representative phonon microscopy images from each treatment are shown in Figure 5.11.

Histogram based analysis was performed using Gaussian mixture models as described in Section 5.2.5. Figure 5.12 shows the histograms and fitted distributions. The fit parameters are shown in Table 5.1. The values for longitudinal elastic modulus, M', are within the range of values previously reported in literature for control cells, and Cytochalasin D and Nocodazole treated cells.[2, 34, 173, 196].

The control population appears to have a bimodal distribution, while the drug treated cells all have trimodal distributions. Thus a sum of two Gaussian distributions was fitted to the control and three for the other conditions. This is interpreted as distinct parts of the cell, such as nucleus and cytoplasm, which have different mechanical properties. To compare distributions, the area under the curve is proportional to the area of the
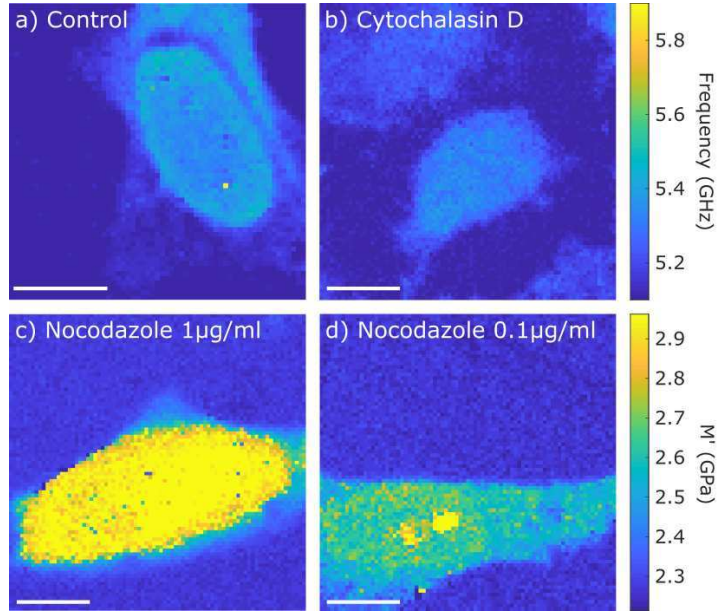
Figure 5.11: Representative phonon microscopy images from fixed HeLa cells subjected to different treatments. Colour scale is the same for all images, and labelled in terms of both Brillouin frequency and longitudinal elastic modulus (M'). Scale bars are $10\,\mu$ m.

Treatment	Background (GHz)	Distribution 1 (GHz)	Distribution 2 (GHz)
Control	5.12 ± 0.03	5.4 ± 0.1	N/A
Cyt D $1\,\mu$M	5.12 ± 0.02	5.18 ± 0.02	5.21 ± 0.05
Noco $3\,\mu$g/ml	5.19 ± 0.03	5.30 ± 0.08	5.8 ± 0.2
Noco $0.3\,\mu$g/ml	5.17 ± 0.03	5.4 ± 0.1	6.0 ± 0.3

Table 5.1: Mean $\pm$ standard deviation values for distributions shown in Figure 5.12. In each case, background refers to the red fit, distribution 1 refers to the blue fit, and distribution 2 refers to the green fit where there is one.
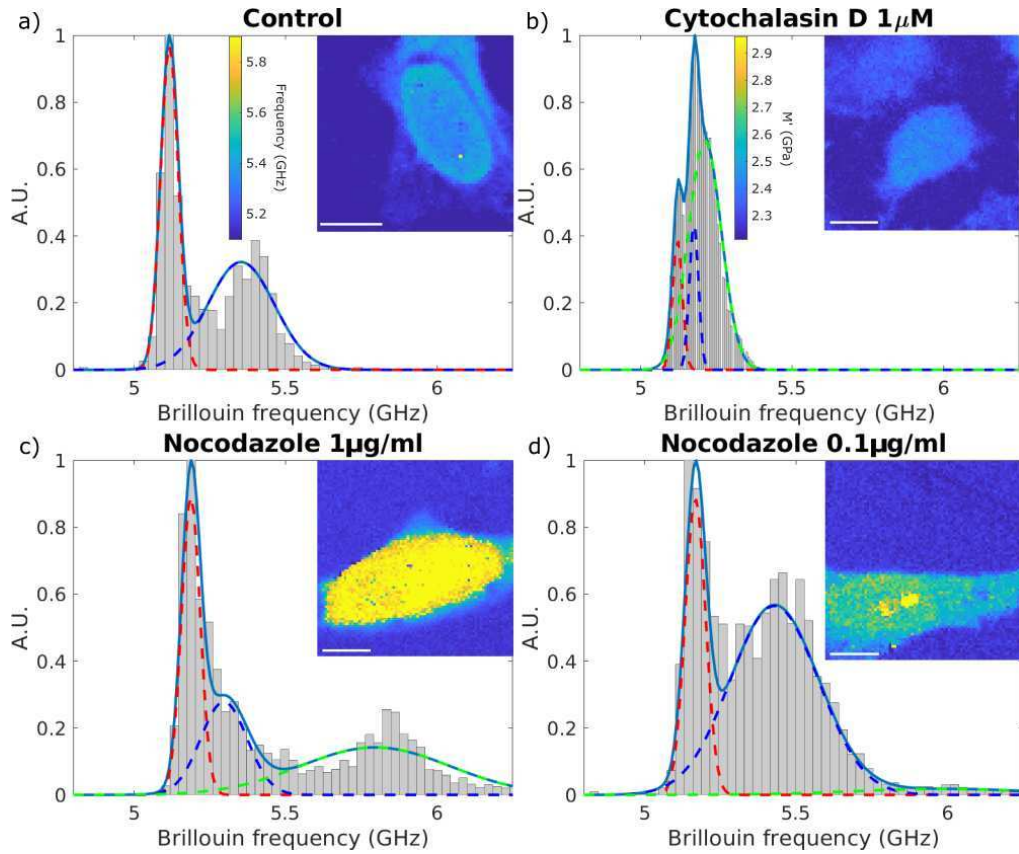
Figure 5.12: Distributions of Brillouin frequencies measured from fixed cell experiments. Each pixel measured in the respective experiments was allocated a bin and resulting distribution was fitted by a sum of Gaussian distributions. Inset are representative images from each condition, with the same colour scale for all images, labelled in terms of both Brillouin frequency and longitudinal elastic modulus (M'). Scale bars are $10\,\mu$ m.

141

cell which that cell part occupies; the mean frequency of the distribution determines the stiffness of that part.

Nocodazole, caused two distributions to shift in a dose-dependent manner. At a low dose (Figure 5.12d), most of the cell (blue distribution) was slightly stiffer than the control, while a small part of the cell (green distribution) was much stiffer. At a high dose (Figure 5.12c), the stiffer distribution represents a greater proportion of the total, although it is less stiff. The softer distribution is now softer than a control cell. The stiffening of a cell after microtubule disruption is explained by the tensegrity model (Figure 2.1d) in which microtubules carry tension; after microtubule disruption, actomyosin contractility increases leading to stiffening of the cell[34].

The initial interpretation for the bimodal distribution and difference in stiffness between the two components is that they represent pixels which are predominantly either nucleus or cytoplasm. The nucleus has previously been reported to have a higher Brillouin frequency than cytoplasm[195], and to stiffen after Nocodazole treatment[34]. The doses investigated here (3 and $0.3\,\mu\text{g/ml}$) are lower than those used by Antonacci (10 and $20\,\mu\text{g/ml}$), and the opposite trend is observed: the mean of distribution 2 decreases with increasing Nocodazole concentration.

Inspection of the relative area taken by each component on the histograms (Figure 5.12c and d) suggests that the distribution 2 for a concentration of $0.3\,\mu\text{g/ml}$ is a much smaller portion of the total cell than distribution 2 in the higher concentration. The representative image shows several high-frequency features near the middle of the cell, possibly nucleoli.

5.3.2 Lethal Dose Study

The first step towards live cell study was to optimise the protocol and enable measurements from live cells over a period of hours which will allow study of the time evolution of cell mechanical properties. To achieve higher temporal resolution than External Passive Microrheology, repeat measurements on the same cell are would need to be made at least once per ten minutes. Many of the experiments towards this goal have incomplete Brillouin frequency data due to faults with the lasers caused by extended downtime during the COVID lockdowns, but this does not impact their validity as lethal dose experiments – the cells were still exposed to the same light and heat dose from the lasers, and fluorescent imaging was unaffected.

A key factor in designing the scan protocol was the low contrast within live cells. Figure 5.13 shows this, with "before and after death" phonon images overlaid on fluorescent images of a HeLa cell. Co-registration was achieved by recording the position of the laser on the camera field of view and positioning the phonon image accordingly. Some data from the first phonon image has been discarded due to laser locking issues – these pixels have been rendered as transparent.

When a cell dies, the drop in fluorescent intensity is coincident with a drop in the Brillouin frequency. Representative data is shown in Figure 5.14a. Typically live cells have a Brillouin frequency (with $780\,$nm wavelength probe) of $5.6{\pm}0.1\,$GHz, while dead cells have a Brillouin frequency of $5.35{\pm}0.05\,$GHz. Cell media has a Brillouin shift of $5.20{\pm}0.05\,$GHz. Interpretation of the shift when cells die requires caution - although the decrease in Brillouin frequency would imply the cell is softer, an intuitive result, both the refractive index and water content of cells changed during apoptosis[197], affecting the relation between Brillouin frequency and
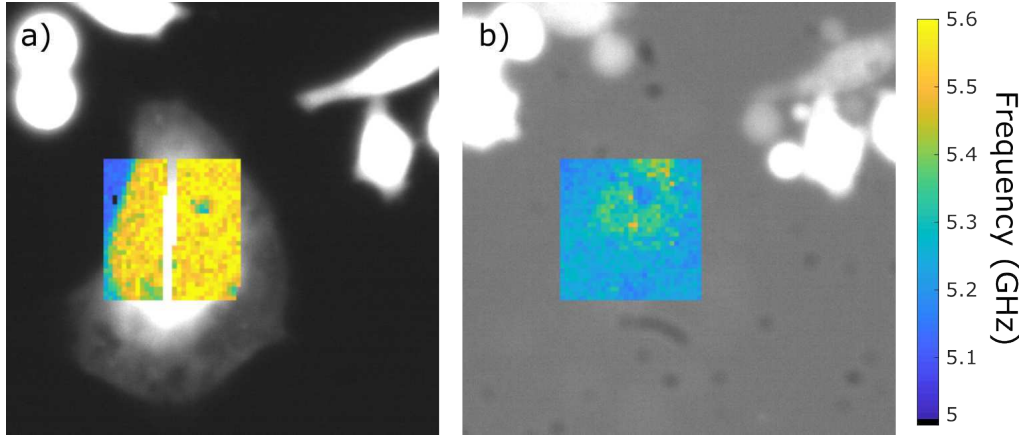
Figure 5.13: Overlay of phonon microscopy images (blue and yellow) on fluorescent images (black and white) taken a) before and b) after a HeLa cell died. Contrast relative to media almost entirely disappears after cell death. Some pixels were omitted from the first phonon image due to aforementioned technical issues. Phonon data covers a $31\,\mu m \times 31\,\mu m$ field of view. Colour scale (far right) is the same for both images.

longitudinal modulus (Equation 5.6).

The transducer design ($20\,nm$ - $200\,nm$ - $20\,nm$) was chosen as it reduced light exposure of the cells, and produced large acoustic amplitudes leading to good acoustic SNR. The downside of this is that most of the light is converted to heat, thus trading phototoxicity for thermotoxicity. Figure 5.14b shows the distribution of cell death times for cells which were scanned (red) or not scanned and visible in the same field of view on the fluorescent images (blue). At the end of the scan, $27\,\%$ of the non-scanned cells had died, while 3 of the 5 cells subjected only to line scanning had died.

To evaluate the statistics, I assume the probability of cell death during the scan is $27\,\%$ for any cell (scanned or not). Using a binomial test, I find that the proportion of cells which were scanned and die is not significantly higher ($p = 0.11$). Thus this data shows that cells are not dying significantly faster when they are scanned.

The rate of death is still prohibitive to long studies of live cell samples.
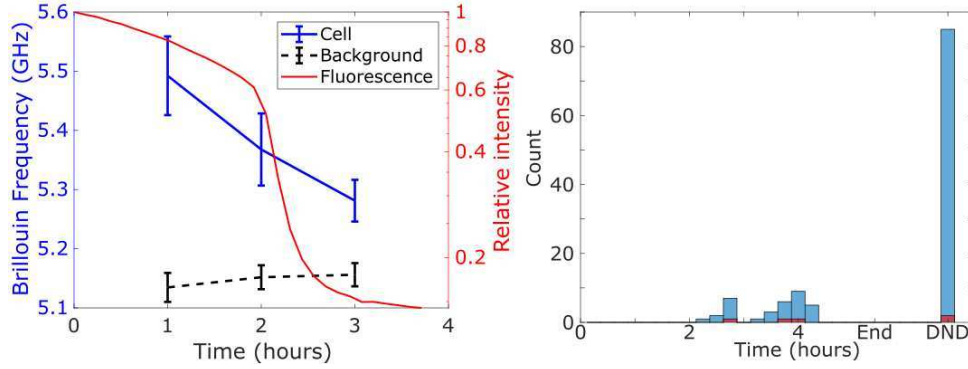
Figure 5.14: a) Measurements at 3 times during a scan show Brillouin frequency (blue) drops at the same time as Calcein-AM fluorescence intensity (red). Slight change in background frequency (black) is discussed in Section 5.4. b) Death time distributions for lethal dose experiment with 20 nm - 200 nm - 20 nm transducer. Cells which were scanned are shown in red. The proportion of cells which died before the end of the experiment was not significantly different for scanned vs non-scanned.

I attribute the high rate of death to two main factors: localised heating produces a heat shock response from the cells which were scanned, and heat conduction may induce response from cells tens of microns away from the laser spot. The localised heating is addressed with an updated transducer design, below. I also note two other factors which will affect lethal dose in experiments spanning several hours: the sample stage is at room temperature, and there is no gas exchange possible.

To compare performance of different transducers, I consider the dose exposure of the cells. To account for the statistical variations in cell death, I calculate the L.D.50: the dose (in J) which is sufficient to kill 50 % of cells in a given experiment; dose (per cell) is defined as

$$L.D.50 = nPt \tag{5.9}$$

where n is the number of pixels in the line scan, P is the total beam power, and t is the dwell time for each pixel. The number of pixels in the line scan

145

Design (nm)	L.D.50 (J)	Time (mins)	Power (mW)	Dwell (s)	N
23-220-23	19	228	4	2	6
20-200-20	20	240	4	2	6
12-133-12	12	130	5	2	5
15-130-15	< 1 †	10	3	1	10
15-130-15	< 1 †	10	6	0.2	10
20-160-20	2 ∗	60	3.5	1	10
20-160-20	< 1 †	10	10	0.2	10
20-180-20	127 ∗	300	20	2	6

Table 5.2: Different transducers designs were trialled and the L.D.50 at a given total power (pump plus probe) is compared. Experiments with the same transducer dimensions were carried out on the same day. L.D.50s marked with † indicate experiments where all cells died too fast to accurately determine L.D.50, and those marked with ∗ indicate experiments where fewer than half of the cells died. Time is duration from first measurement to when 50 % of cells died (or, for ∗, duration of experiment). Dwell is the time to acquire 1 pixel, and N is number of cells scanned in that experiment.

(as opposed to number of pixels on the cell) was used in order to account for the heat dose received when the laser spot is within a few microns of the cell. The results from all lethal dose experiments are shown in Table 5.2.

5.3.2.1 Final lethal dose Experiment

This section presents the results from the lethal dose experiment with the final transducer design, 20 nm - 180 nm - 20 nm. The plan for the lethal dose experiment was to begin with a high power and kill cells quickly, before performing subsequent scans at lower powers to find a dose which does not cause faster cell death.

To this end, I performed a scan using 16 mW of pump light and 4 mW
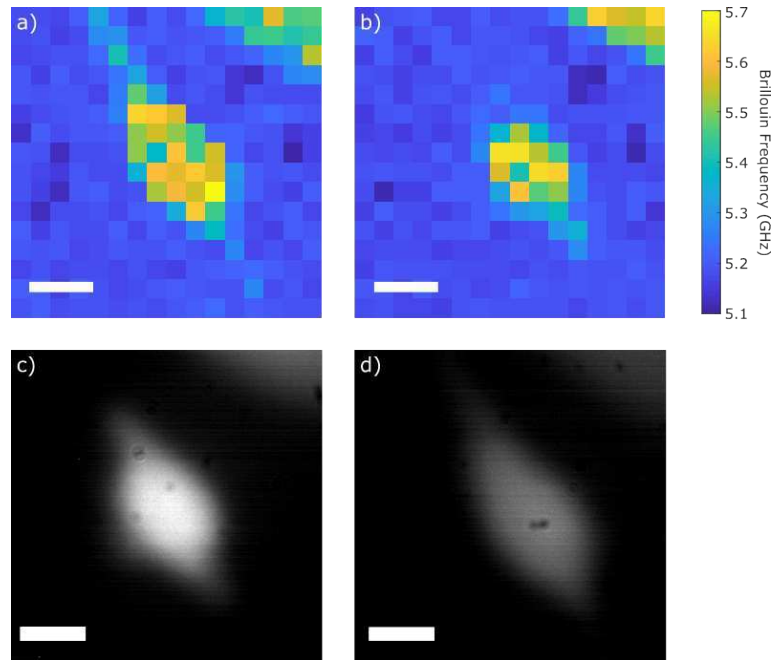
Figure 5.15: a,b) Brillouin frequency maps and c,d) Calcein-AM fluorescent images of a live HeLa cell before and after 1 hour of imaging, as described in the text. The rounding visible indicates the cell is not healthy. The Brillouin frequency of the cell has decreased, likely due to the processes leading up to apoptosis. Scale bars are 10 µ m

of probe, with 2 s pixel dwell time. Using the live cell scanning protocol (Figure 5.9), 6 cells were selected for 5 counts. After the initial scan, none of the scanned cells had died, so the line scans were repeated for a total of 4 hours scan time.

Figure 5.15 shows Brillouin frequency maps and live fluorescent images of the cell chosen for a 2D scan. The 2D scan covered a 30 µm×30 µm area, with 1 µm step size, and the line scans were also 30 µm with 1 µm spacing. The images took 30 minutes to acquire, and each line scan took 1 minute.The cell did not die during the scan, as confirmed by the fluorescent images, however the rounding of the cell, visible by both modalities, indicates that the cell is not healthy.

Inspection of the fluorescent images for one of the cells solely subjected to
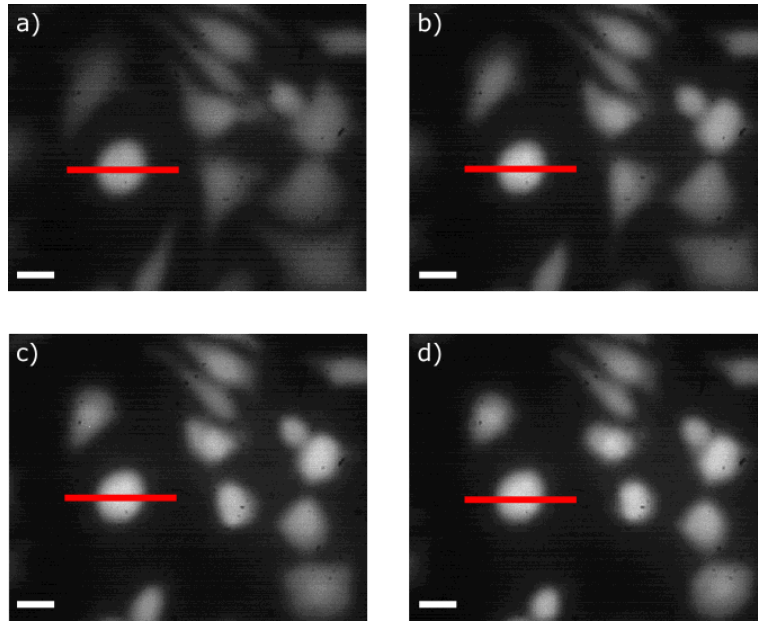
Figure 5.16: Calcein-AM fluorescence images taken a) at the beginning of the scan, and after b) 1 hour, c) 2 hours, d) 3.5 hours of repeated line scans of the area marked in red. It can be seen that none of the cells die, however by 3.5 hours they have all rounded up, indicating poor health. Scan protocol is described in the text. Scale bar is 10 µ m.

line scans (Figure 5.16) shows that all cells within the field of view had a similar response to the scan. After 3.5 hours of scanning the cell marked in red, none of the cells visible in this field of view have died. However, all have rounded up.

The field of view shown in Figure 5.16 is not anomalous. Of the 6 cells scanned in this experiment, none died, as shown by both frequency and fluorescence data in Figure 5.17. This lethal dose study demonstrates a transducer design and scan protocol for live cell experiments over a timescale of hours. There is no long-term trend in the mean Brillouin frequency of the cells, however the distribution of Brillouin frequencies broadens indicating a heterogeneous cell response to being scanned.
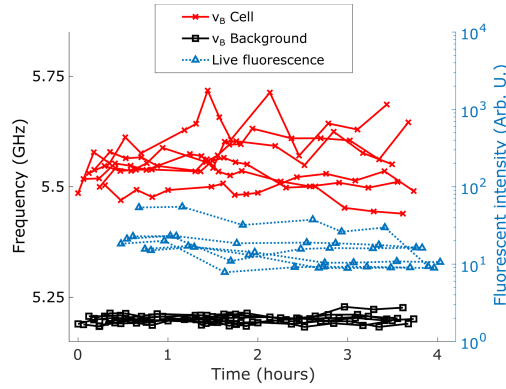
Figure 5.17: For each cell scanned, the line scan is segmented into "cell" and "background". The fluorescent images are analysed as described in Section 5.2.6. Each line represents data from one cell (or background adjacent to that cell). This result demonstrates that it is possible to perform repeated measurements over several hours without killing cells.

5.3.3 Cytoskeletal Disruption in Live Cells

Having settled on a transducer design and scan protocol which enable study of live cells for multiple hours, I now consider delivery of a drug to the cells. The tube connecting the syringe to the sample holder, shown in Figure 5.2b, was connected to a Y-piece with two syringes. These were connected to syringe pumps (NE-1000, SyringePump.com, USA) to deliver either media or media mixed with drug.

Before starting experiments with cells, the syringe pump protocol needed to be validated. To design the pump protocol, I started with a rough calculation of the volume held within the sample chamber which yielded $300\,\mu l$. Using food dye, I observed that running the syringe at constant flow rate lead to poor mixing between the liquids.

The final pump protocol was to run the pump to dispense $7\,\mu l$ in $0.42\,s$, and then pause for $0.58\,s$. The time-averaged flow rate was thus $7\,\mu l/s$, hence delivering the entire sample chamber volume in under 1 minute. The protocol was run for 300 repetitions (i.e. $2.1\,ml$ total volume) to ensure the
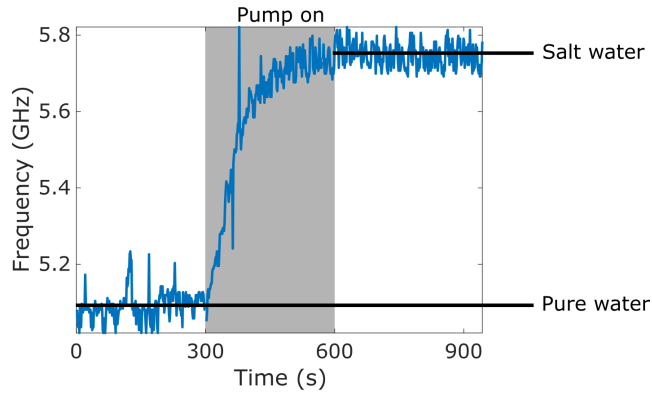
Figure 5.18: A syringe pump was turned on at 300 s to replace distilled water with salt water while phonon microscopy measurements were made. Frequency reached steady value within 200 s of starting the pump. Pump was on for time indicated by the shaded area, running the program described in the text.

chamber had been fully flushed.

To test the protocol, I used one syringe with distilled water and one with salt water (NaCl, 230 g salt per 1 kg water). Figure 5.18 shows the Brillouin frequency changing when salt water replaces distilled water. The pump was turned on at 300 s, and a stable frequency is reached by 500 s. This demonstrates the ability to replace one solution with another, in situ, enabling delivery of a drug to live cells without interrupting the scan protocol developed for live cell study.

5.3.3.1 Actin Depolymerisation

The first drug investigated was Latrunculin B, an actin depolymeriser. This is the same drug used on cells in Chapter 4, and was expected to cause cells to soften. Two batches of serum-free media were made up, one containing 1 µM Latrunculin B. These were loaded into syringes and connected to the cell chamber which was initially filled with drug-free media.

Live cells were prepared in the same manner as for the lethal dose exper-
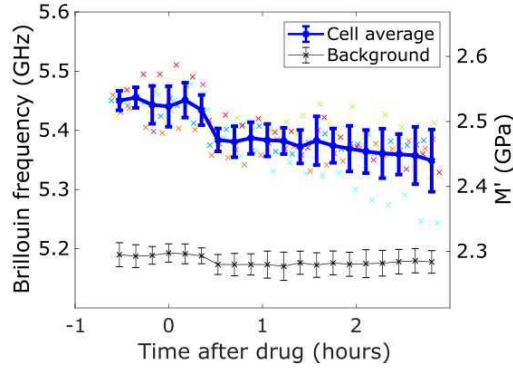
Figure 5.19: Time course experiment showing Brillouin frequency and longitudinal elastic modulus of live cells changing after addition of an actin depolymerizing drug. Crosses indicate individual cell averages, blue indicates mean ± standard deviation of all cells scanned.

iments. Using the live cell scanning protocol and syringe pump protocol that were developed already, an experiment was performed with N=12 cells for M=20 counts. The pixel dwell time was 1s, giving temporal resolution (time per count) of 10 minutes.

Segmentation was performed manually, dividing the line scan into cell and background. Subsequent analysis excluded cells which died or moved during the experiment; although cell motility (or "crawling") is expected to decrease after actin disruption, cells may move if they round up after drug treatment. There were 7 cells which remained within the scan area for the whole experiment - the averages for each cell at each time point are plotted as crosses on Figure 5.19. The average for all cells ± standard deviation is plotted in blue with error bars, and the background is plotted in black.

The Brillouin frequency of the cells decreases sharply within 20 minutes of adding the drug, from 5.45±0.03 GHz to 5.38 ± 0.03 GHz, before decreasing further at a rate of 27 MHz/hr. The initial drop is congruent with the results seen from Cytochalasin D on fixed cells (Section 5.3.1), and results from microrheology (Chapter 4) where actin disruption causes cells to

soften. The slower decrease, seen roughly 1.5 hours after drug treatment, may be explained by the different purposes actin fulfils within a cell. This is discussed in Section 5.4. A similar trend is not seen in control cells as shown in Figure 5.17.
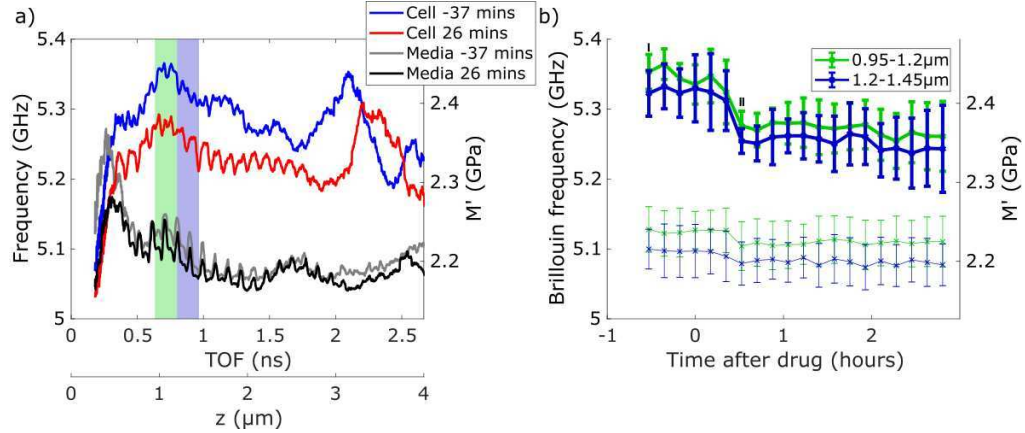
Figure 5.20: a) Mean cell Brillouin frequencies vs depth for the two counts (37 minutes before and 26 minutes after drug addition). A decrease in frequency is seen at all depths, not just near the basal surface of the cell. Axial reconstruction described in text. Two highlighted ranges are considered in more detail in b. b) Brillouin frequency at two select depths plotted for every count. This depth was chosen as it spans the frequency peak at around 1 μm. The difference in media frequency at two depths is caused by the temperature gradient near the transducer[93]. Black marks (I and II) denote two counts shown in a.

Filamentous actin is primarily localised to a ∼200 nm thin cortex on the inside of the plasma membrane[198]. Theoretically, phonon microscopy has sufficient axial resolution to resolve this layer, as estimated in Section 5.2.2. To access axial information, a wavelet transform is used as per Section 5.2.3.1. The mean frequency of all cells as a function of time of flight is plotted in Figure 5.20. Conversion from time of flight (TOF) to position assumes speed of sound is homogenously $1.5 \, \text{kms}^{-1}$. The frequency vs depth plot shows a maximum at ∼0.5 ns, followed by a steady decline. Disruption of actin does not alter the shape of this profile, merely shifting it downwards by ∼500 MHz.

5.4 Discussion

Results have been presented from phonon microscopy of live and fixed cells. The fixed cell results demonstrated the ability to resolve individual components of cells. Live cell results included optimisation and demonstration of biocompatibility, and measuring the effects of an actin depolymerizing drug over several hours. These are an advancement in the application of time-resolved Brillouin scattering to biological specimens, proving that Phonon Microscopy is at least as suitable for live cell study as other Brillouin scattering techniques.

5.4.1 Actin Disruption

To my knowledge no prior cell mechanics study has reported measurements *during* treatment by a cytoskeleton-targetting drug. Thus the interpretation here contains speculation based upon understanding of actin dynamics from cellular biology. The change in Brillouin frequency after addition of Latrunculin B, shown in Figure 5.19, appears to be composed of a biphasic response. Shortly after adding the drug, there is a sharp drop in Brillouin frequency, followed by a slower downward trend. One possible explanation relates to the turnover rate of actin within cells.

It is well known that actin undergoes a continuous turnover known as treadmilling, with new G-actin units adding to one end of a filament while they dissociate from the other end. The lifetime of an actin filament can be highly variable[29, 199], and there may be processes other than treadmilling contributing to actin turnover[200]. The action of Latrunculin B (and several other actin-targetting drugs) is to bind to actin monomers and to the growing end of actin filaments, preventing further assembly[201]. Thus

the number of actin filaments within the cell will decrease after the drug is added because the filaments naturally disassemble.

The observed biphasic softening of the cells may relate to there being a spread of rates of actin disassembly: If there are two processes for actin turnover which have rate constants differing sufficiently, the contribution of actin to cell elasticity will exhibit a biphasic decay as the fraction of actin undergoing fast turnover will disassemble first and quickly, while the fraction of actin undergoing slow turnover will disassemble slowly. Unfortunately, comparing the biphasic response seen in my data to other published results is not possible as there are (to my knowledge) no published results showing time resolved changes in cell mechanics after addition of an actin polymerisation inhibitor and very few such fluorescent imaging studies.

5.4.2 Thermal Effects

The causes of cell death during imaging by phonon microscopy were considered, and three main possibilities emerged: heating by laser absorption at the transducer, other phototoxic effects due to laser exposure, or poor conditions within the sample chamber. Finite element modelling has been performed by other members of the group to investigate heating effects in phonon microscopy, revealing that the temperature reaches a steady state within a few milliseconds of turning on the lasers. the temperature rise at the transducer surface is less than $10\,°C$ for the experimental setup used in live cell experiments, and that this falls rapidly with distance from the transducer[93].

To determine the cause of cell death, a viability experiment was performed using an "upside-down" transducer, i.e. with the transducer cavity on the

bottom of the sapphire, not in contact with the cells atop the sapphire. The heating from laser absorption is 170 µm away from the cells, but acoustic measurements are not possible. This revealed that heating by the transducer was the main cause of cell death. Optimisation of the scan protocol and transducer design reduced this heating and cell death was avoided as demonstrated in the lethal dose study presented.

For lethal dose studies, the death times of several cells within the same fluorescent image field of view was compared assuming that cell deaths were independent events (i.e. probability of one cell dying is not affected by other cells). The death times of cells near the cell being scanned may, however, be affected by the scan. That is, scanning 50 µm away from a cell may increase the chance of it dying. This hypothesis was confirmed visually when panning across the sample after the scan. A greater proportion of cells appeared dead in the vicinity of the cells which were scanned than in areas further away. This may be due to heat conduction from the laser although finite element modelling suggests that temperature rise is less than 1 °C a few microns away from the laser focus[93], or due to biochemical signals released by the scanned cell in response to heat shock. In either case, it should be kept in mind when performing live cell experiments over several hours.

Laser absorption causes localised heating at the transducer and a depth-dependent shift in Brillouin frequency seen for the media in Figure 5.20. The Brillouin frequency of liquid water increases $\sim$10 % from room temperature to a maximum at $\sim$70 °C[202], compared to the depth-dependent frequency shift seen here which is around 1 %. Heating will lead to a systematic underestimation of the cell stiffness which worsens with increasing with greater laser power. To reduce this, only a total of 5 mW of laser power is used for the actin disruption experiment, giving an estimated temper-

ature rise of $5\,°C$ at a distance of $1\,µm$ from the transducer surface[93]. There is an additional sample-dependent variation in Brillouin frequency due to random variation in the transducer optical absorption, however the design of live cell experiments here utilises repeated measurements of the same cells an an internal control, removing this effect.

The background frequency, i.e. the mean frequency value for pixels which were not "on" the cell, varies by a few percent during experiments. This is likely due to small variations in temperature: over the course of several hours, focal drift is the main factor causing a change in local heating as the size of the focal spot, and hence pump fluence, will vary. This can be caused by the room temperature changing when the air conditioning turns on or off.

5.4.3 Signal Processing

The relatively large number of measurements acquired in the fixed cell experiments allowed the distributions of frequencies to be considered and changes to different intracellular components to be considered. For each live cell in the Latrunculin B experiment, only 620 pixel measurements were acquired, compared to 6561 for each of the fixed cells in the Nocodazole experiments. Thus histogram-based analysis was not applied to live cell results.

The transverse resolution of phonon microscopy is theoretically limited by the smaller of the pump or probe spot size (here both are $1.1\,µm$). In live cell study however, the long acquisition times are prohibitive to resolving details within cells. Similarly to how a two second exposure photograph blurs many details, this is added to the effect of having ~30 minute im-

age acquisition times; thus intracellular components can move significantly on the time scale of the image acquisition. Thus although a live cell has heterogeneous density on the nanoscale, the optical system and signal processing essentially perform spatiotemporal averaging over both the focal volume and the acquisition time; this effect is compounded with the poor opto-acoustic contrast of live cells, and very little detail is visible within the cell. Thus the results reported here have been averaged, often over several cells, to improve SNR and statistical power of observations.

The axial reconstruction, shown in Figure 5.20, shows a sharp increase in Brillouin frequency peaking at around 1 μm depth. When interpreting this, it is important to bear in mind the effect of transducer resonance: the transducer may "ring" for a short time after excitation in which case the portion of the time trace immediately after the coincidence peak (marked i on Figure 5.6) will contain oscillations at the resonant frequency of the transducer, not the Brillouin frequency. This results in an effective blind zone adjacent to the transducer which explains why the media and cell frequencies are so similar up to ∼0.5 ns, equivalent to ∼0.7 μm in water.

5.4.4 Applications of Phonon Microscopy

There are several factors currently limiting broader application of phonon microscopy. These can be summarised as cost, limitations to samples which can be studied, and biocompatibility. To make the measurements presented here, a large and expensive optical setup was needed including two femtosecond pulsed lasers in ASOPS configuration, preventing widespread adoption of the technology. This also limits the portability, meaning samples must be brought to the instrument. Transational challenges, however, are not unusual for microscopy, especially custom-built instruments, and

prevents many capable technologies from reaching clinical applications.

Currently the system requires fine alignment to overlap two beams within the sample and deliver the probe light to a detector. Additionally, measurements are limited to within a few microns of the coverslip due to the strong attenuation of sound at gighertz frequencies. Optical fibres with opto-acoustic transducers coated onto the tip have been developed as an alternative, overcoming both of these limitations and developing towards endoscopic applications[203, 204]. To achieve this, portable laser systems will be needed.

Acquisition time is a challenge for any technique studying sensitive biological samples. Phonon microscopy is no exception and it was shown here that laser heating is the predominant cause of death in cells measured. To improve acquisition time, I assisted in the development of parallel detection for phonon microscopy[205]. The setup uses larger pump and probe spot sizes, followed by a fibre bundle to simultaneously measure six nearby points on the sample. This allowed a speedup of $3\times$, now limited by acquisition hardware rather than signal-to-noise ratio.

5.5 Conclusion

This chapter detailed experimental setup and signal processing for phonon microscopy. Results were presented from cytoskeletal disruption studies in fixed and live cells which were in agreement with Brillouin scattering results available in literature. Fixed cells enables much longer experiments and generation of larger data sets. This in turn allows the distribution of Brillouin frequencies within cells to be further studied with tools such as Gaussian mixture models.

Live cell study protocols were developed, and the acoustic characteristic of cell death was studied using Calcein-AM for fluorescent imaging of live cells. After trialling several transducer designs, one was found that enabled continuous measurements of live cells over four hours without killing them. To the best of my knowledge, this represents the longest continuous Brillouin scattering measurements of single live cells reported anywhere, an improvement of over two hours[93, 173, 206].

The biocompatibility demonstrated enabled an experiment to measure the effects of disrupting the actin cytoskeleton in live cells, where repeated measurements of the same cells provides an internal control to the experiment. A biphasic shift in Brillouin frequency can be seen with phonon microscopy during treatment with Latrunculin B. The shift corresponds to cells softening quickly after addition of the drug, and then continuing to soften over the next hour. I conjecture, with justification based on literature, that the biphasic response is caused by a range of turnover times for actin monomers within the cell. The heterogeneity of the longitudinal modulus was probed considering the direction vertically up from where the cell adheres to the transducer however with current signal to noise ratio, acquisition speed and signal processing methods, there is no noticeable change in longitudinal modulus to the cortical layer of the cell relative to the bulk cytoplasm. This is the first time that the effects of actin depolymerisation on longitudinal elastic modulus (M') has been measured in live cells. The mean change across 7 cells was a 2% decrease (compared to $0.5\,\%$ inter-cellular variation), and values for control and drug treated cells were comparable to those previously reported[206].

For ease of comparison, typical Brillouin frequencies and equivalent moduli have been listed in Table 5.3. The contrast between live cells and fixed cells highlights the importance of live cell study as the fixation process causes

Cell condition	Typical ν_B (GHz)	Equivalent M′ (GPa)
Healthy	5.55	2.61
Dead	5.35	2.43
Fixed	5.35	2.43
Lat B live	5.38	2.52
Cyt D fixed	5.17	2.27
Noco 3µg/ml fixed	5.30	2.38
Noco 0.3µg/ml fixed	5.43	2.50
Water	5.15	2.27
Salt water	5.75	3.13
Cell media	5.20	2.33

Table 5.3: Summary of phonon microscopy results in this chapter. Equivalent longitudinal moduli were calculated with Equation 5.6. All cell values are for HeLa cells where density, ρ, was assumed to be $1050\,\mathrm{kg/m^3}$ and refractive index, n, to be 1.3716; these values may not hold true for the fixed or dead cells. For pure water and media, $\rho = 1000\,\mathrm{kgm^3}$ and $n = 1.33$, and for salt water $\rho = 1170\,\mathrm{kg/m^3}$ and $n = 1.37$[207].

an apparent softening in the longitudinal modulus. Fixed cells have a similar shift to dead cells, which may be due to aggregation of subcellular components in fixation and apoptosis respectively. The values reported here for M' in fixed cells should be taken cautiously as the density and refractive index used were the same as for live cells.

Chapter 6

Conclusions

In this thesis I set out to perform single cell bio-mechanical measurements of the effects of cytoskeleton disruption in live cells. Two techniques, External Passive Microrheology (EPM, Chapters 3 and 4) and Phonon Microscopy (PM, Chapter 5), each probing a distinct time-scale and length-scale, were chosen to compare and contrast. Many existing techniques for measuring cell mechanics rely upon applying external forces to the cell which can cause fluidisation and rejuvenation[64], processes by which the viscoelasticity of the cell changes over time breaking the ergodicity of the system[88, 120]; others rely on foreign particles being incorporated into the cells[102], which may have unknown effects. EPM uses thermal fluctuations to probe the mechanical properties of cells without applying external forces, allowing study of both the viscoelastic properties and the force generation of single living cells. PM uses coherent acoustic pulses generated and detected by pulsed lasers to measure the elasticity of living cells while only applying minimal, localised, strain and achieving higher spatio-temporal resolution than is possible with EPM.

6.1   Objectives of the Thesis

Below is a restatement of the objectives set out in Section 1.4:

1. Passive Microrheology measurements of live cells:

    1.1. Develop software to perform video microrheology data acquisition on an existing optical trapping microscope.

    1.2. Develop analyis software to process microrheology data:

    1.2.1. Implement methods to perform numerical inversion from time to frequency domains.

    1.2.2. Create methods to measure characteristic relaxation times and frequencies.

    1.3. Perform live cell experiments:

    1.3.1. Develop analytical framework to quantify cell stiffness and viscosity.

    1.3.2. Measure changes in cell mechanical properties and active force generation over time.

    1.3.3. Elucidate the effect of actin disruption on cell stiffness, viscosity and active force generation.

2. Phonon microscopy measurements of live cells:

    2.1. Demonstrate sensitivity of phonon microscopy to the effects of cytoskeletal disruption using fixed cells.

    2.2. Develop biocompatibility of the technique:

    2.2.1. Fabricate transducers for both pump and probe at infrared wavelengths.

    2.2.2. Implement fluorescence imaging including hardware control and image processing to determine cell death time.

    2.2.3. Investigate factors contributing to biocompatibility including heating and laser light exposure.

    2.3. Measure the effect of actin disruption in live cells:

    2.3.1. Design experiment with an internal control.

    2.3.2. Develop and test drug delivery method.

    2.3.3. Process data to yield spatiotemporally-resolved cell elasticity during actin disruption.

6.2 Microrheology of Live Cells

Aim 1 of the thesis was to perform passive microrheology measurements of the viscoelastic properties of single live cells. The method chosen uses an optical trap to position a streptavidin-functionalised microsphere on the surface of a cell, the trapping laser is then turned off before making measurements of the pseudo-Brownian motion of the microsphere. This avoids applying external forces and is shown to simultaneously measure the viscoelasticity and active force generation of cells, a combination which has not previously been demonstrated in a single measurement.

Microrheology measurements were implemented on an existing optical trapping microscope (aim 1.1) using video microscopy and real-time image processing to perform particle tracking. The software developed to do this enabled data acquisition rates of over 1 kHz for arbitrarily long durations and has been shared to the community on an open-source license via github[142]. The effects of particle tracking errors was investigated and experimental methods were developed to minimise these.

Analysis of particle tracking data (aim 1.2) follows the well-established theory underpinning microrheology to invert the time-dependent mean-squared displacement to the frequency-dependent complex shear modulus[114]. Techniques were implemented using vectorised operations in MATLAB to perform this inversion quickly while minimising numerical errors (aim 1.2.1). Interpretation of data was aided by measuring characteristic relaxation times and equivalent frequencies (aim 1.2.2); while this is commonly done in optical trapping viscosity measurements by fitting a monoexponential decay to the position autocorrelation function[117, 208], this requires a preconception of the form of the experimental data[109]. To measure the relaxation times with minimal a priori knowledge of the form of the data, a

method utilising power-law fitting was developed and tested by measuring the viscosity of water.

Live cell experiments (aim 1.3) used streptavidin-functionalised microspheres which bind to integrin receptors on the cell surface[159]. Particle tracking data was interpreted using an analytical framework based upon established microrheology methods[1, 117, 141] and numerical techniques developed in this thesis (aim 1.3.1). Repeated measurements of the same cell-bead pair provide internal controls to monitor changes in cell mechanical properties over periods of tens of minutes (aim 1.3.2).

Integrin binding triggers focal adhesion formation[36, 57, 159, 161] and this results in a stiffening of the cell over tens of minutes after the bead binds (median $\pm$ half inter-quartile range of change in geometric stiffness $\Delta\beta G_0' =$2$\pm$5 N/m). This is, to the best of my knowledge, the first time the development of focal adhesions has been probed with microrheology, although imaging studies have confirmed cytoskeletal reorganisation under similar conditions[158].

Analysis of data from cell experiments was aided by an analogy to optical trapping, revealing a cellular viscosity a factor of 23 times greater than the viscosity of water, which is similar to the factor of 25 reported by fluorescence correlation spectroscopy[96]; interestingly, this viscosity is invariant during the aforementioned cell stiffening. Disruption of the actin cytoskeleton by Latrunculin B caused cell softening ($\Delta\beta G_0' =$-4$\pm$5 N/m) without changing the viscosity (aim 1.3.3).

Using the optical trap to position the bead on the cell surface allowed for control over the degree of embedding of the bead into the cell; this, coupled with fast video microrheology, was able to resolve the short-time viscous behaviour of the bead adhesion site on the cell surface which has

not previously been reported. Combining measurements of the cell stiffness and active strain generation allowed the force generation of the cell to be probed (aim 1.3.3). Confirming prior results which attribute increases active strain after actin disruption to a lowering of cell prestress but do not simultaneously measure cell elasticity[141], I was able to demonstrate that both the force generation and stiffness decrease which leads to a higher active strain rate.

The technique demonstrated here for measurements of single cells may be applied in the future for study of cell mechanics during specific interactions between cells and functionalised surfaces. For example, clathrin-mediated endocytosis is a process by which the cell surface forms a concave pit which grows and eventually closes to form a membrane-encapsulated bubble within the cell known as an endosome[209]. While it is obvious that the cell must generate forces to cause this, it has not yet been possible to study cell mechanics during this process. Techniques such as atomic force microscopy would not be able to access the binding site without interfering with the process, whereas EPM would be able to follow the process by using the *pseudo*-Brownian motion of the endocytosed particle to probe the viscoelasticity of the binding site.

6.3   Phonon microscopy

The second aim of the thesis was to develop phonon microscopy experiments on live cells. Phonon microscopy, and other forms of Brillouin microscopy, are in their infancy regarding applications to living matter[93, 173, 195, 210–213]. Phonon microscopy has been previously limited by biocompatibility due to use of ultra-violet lasers to generate coherent acoustic

pulses[93, 173]. Here I avoid this by using an opto-acoustic transducer designed to optimise signal-to-noise ratio when working with infra-red lasers to generate and detect the acoustic pulses. Transducers were fabricated on sapphire coverslips using sputter-coating of gold and ITO in an Au-ITO-Au sandwich forming a Fabry-Pérot interferometer to increase pump laser absorption (aim 2.2.1).

Preliminary phonon microscopy experiments were performed using ultraviolet pump lasers and fixed cells to demonstrate sensitivity to changes brought about by disruption of the actin and microtubule networks within cells (aim 2.1). When working with fixed cells it is easy to collect large numbers of point measurements across several cells, and data was analysed using gaussian mixture models, a histogram fitting technique. Control cells exhibit a single gaussian distribution of Brillouin frequency (mean $\pm$ standard deviation: 5.40$\pm$0.1 GHz); cells treated with either Cytochalasin D, an actin-disrupting drug, or Nocodazole, a microtubule-disrupting drug, exhibit a bimodal distribution of Brillouin frequencies with one component stiffening and one component softening in each case (Cyt.D.: 5.18$\pm$0.02 GHz and 5.21$\pm$0.05 GHz, Noco.: 5.30$\pm$0.08 GHz and 5.8$\pm$0.2 GHz).

To work with live cells (aim 2.2), first an assay for cell death was implemented using Calcein-AM, a fluorescent label activated by cytoplasmic esterase activity. Fluorescent imaging capability was added to the phonon microscope using LED widefield illumination and a basic CCD camera with appropriate excitation and emission filters. I integrated control of the illumination and imaging into the software used to collect phonon microscopy data (aim 2.2.2). This enabled a lethal dose study to determine optimal transducer dimensions to maximise biocompatibility and signal-to-noise ratio. It was determined that heating by laser absorption at the transducer is the main cause of cell death when working with infra-ref pump and

probe beams. A protocol was developed consisting of line measurements on several cells consecutively before repeating, reducing the exposure to any single cell. Reported here are continuous measurements on live cells over the course of up to four hours without killing them, a first for phonon microscopy.

The effects of actin disruption on live cells in situ was investigated (aim 2.3) in a change-over-time experiment providing an internal control: cells were measured for a short time before replacing the media within the chamber with media containing the drug (aim 2.3.1). Use of a closed sample chamber necessitated the development of a syringe pump protocol to replace the media within the chamber quickly and completely without washing away cells. The protocol was tested by replacing deionised water with salt water, where Brillouin frequency measurements reached a stable value five minutes after turning on the syringe pump (aim 2.3.2).

Phonon microscopy measurements of live cells during actin disruption were the first such time-resolved mechanical measurement on single live cells (aim 2.3.3). Hela cells exhibited a sharp drop in Brillouin frequency, a proxy for stiffness, immediately after addition of the drug (from 5.45 ± 0.03 GHz to 5.38 ± 0.03 GHz), and continued to soften slowly over the next hour, to 5.35 ± 0.06 GHz. An advantage of phonon microscopy over other Brillouin techniques is that each point measurement contains axially-resolvable measurements of the Brillouin frequency. Wavelet analysis of the actin disruption experiment showed that Hela cells exhibited a region of high Brillouin frequency just above the basal membrane, and this contrast remains after disruption of the actin. Thus the disruption of actin affects not just the mechanics of the cell cortex, but also of the cytoplasm.

Phonon microscopy is a promising technique for studying adherent cell me-

chanics with higher axial resolution than other Brillouin scattering techniques[93]. The capability for studying dynamic processes in live cells was demonstrated here and a future application that phonon microscopy is well suited for would be the mechanics of cellular adhesion. Currently transducer resonance creates a "blind zone" of around 600 nm adjacent to the transducer, however using a polymer layer would move the cell out of this zone. The effect of substrate stiffness on focal adhesion formation has been studied with fluorescence microscopy[12, 35], however access to the basal surface of the cell has prevented study of the mechanics of focal adhesions. Phonon microscopy is perfectly situated to study this.

Bibliography

[1] Rebecca L. Warren, Manlio Tassieri, Xiang Li, Andrew Glidle, David J. Paterson, Allan Carlsson, and Jonathan M. Cooper. Rheology at the micro-scale: new tools for bio-analysis. In Pietro Ferraro, Monika Ritsch-Marte, Simonetta Grilli, and David Stifter, editors, *Optical Methods for Inspection, Characterization, and Imaging of Biomaterials*. SPIE, may 2013.

[2] Fernando Pérez-Cota, Richard J. Smith, Emilia Moradi, Leonel Marques, Kevin F. Webb, and Matt Clark. High resolution 3d imaging of living cells with sub-optical wavelength phonons. *Scientific Reports*, 6(1), December 2016.

[3] Donald E Ingber, Ning Wang, and Dimitrije Stamenović. Tensegrity, cellular biophysics, and the mechanics of living systems. *Reports on Progress in Physics*, 77(4):046603, 2014.

[4] Jeff Hardin, Gregory Paul Bertoni, and Lewis J Kleinsmith. *Becker's World of the Cell*. Pearson Higher Ed, 2017.

[5] Fiona K Glenister, Ross L Coppel, Alan F Cowman, Narla Mohandas, and Brian M Cooke. Contribution of parasite proteins to altered mechanical properties of malaria-infected red blood cells. *Blood, The Journal of the American Society of Hematology*, 99(3):1060–1063, 2002.

[6] Carmela Rianna and Manfred Radmacher. Cell mechanics as a marker for diseases: biomedical applications of afm. In *AIP Conference Proceedings*, volume 1760, page 020057. AIP Publishing LLC, 2016.

[7] Silvia Pelucchi, Ramona Stringhi, and Elena Marcello. Dendritic spines in alzheimer's disease: How the actin cytoskeleton contributes to synaptic failure. *International Journal of Molecular Sciences*, 21(3):908, January 2020.

[8] MM Brandão, A Fontes, ML Barjas-Castro, LC Barbosa, FF Costa, CL Cesar, and STO Saad. Optical tweezers for measuring red blood cell elasticity: application to the study of drug response in sickle cell disease. *European Journal of Haematology*, 70(4):207–211, 2003.

[9] Subra Suresh, J Spatz, John P Mills, Alexandre Micoulet, Ming Dao, CT Lim, M Beil, and Thomas Seufferlein. Connections between single-cell biomechanics and human disease states: gastrointestinal cancer and malaria. *Acta biomaterialia*, 1(1):15–30, 2005.

[10] Sanjay Kumar and Valerie M Weaver. Mechanics, malignancy, and metastasis: the force journey of a tumor cell. *Cancer and Metastasis Reviews*, 28:113–127, 2009.

[11] Gautier Follain, David Herrmann, Sébastien Harlepp, Vincent Hyenne, Naël Osmani, Sean C Warren, Paul Timpson, and Jacky G Goetz. Fluids and their mechanics in tumour transit: shaping metastasis. *Nature Reviews Cancer*, 20(2):107–124, 2020.

[12] Robert J Pelham Jr and Yu-li Wang. Cell locomotion and focal adhesions are regulated by substrate flexibility. *Proceedings of the national academy of sciences*, 94(25):13661–13665, 1997.

[13] Dennis E Discher, Paul Janmey, and Yu-li Wang. Tissue cells feel and respond to the stiffness of their substrate. *Science*, 310(5751):1139–1143, 2005.

[14] Kandice R Johnson, Jennifer L Leight, and Valerie M Weaver. Demystifying the effects of a three-dimensional microenvironment in tissue morphogenesis. *Methods in cell biology*, 83:547–583, 2007.

[15] Donald E Ingber, Deepa Prusty, Zhengqi Sun, Hannah Betensky, and Ning Wang. Cell shape, cytoskeletal mechanics, and cell cycle control in angiogenesis. *Journal of biomechanics*, 28(12):1471–1484, 1995.

[16] Nicholas D Evans, Caterina Minelli, Eileen Gentleman, Vanessa LaPointe, Sameer N Patankar, Maria Kallivretaki, Xinyong Chen, Clive J Roberts, and Molly M Stevens. Substrate stiffness affects early differentiation events in embryonic stem cells. *Journal of European Cells and Materials*, 18:1–14, 2009.

[17] Harold P. Erickson. The discovery of the prokaryotic cytoskeleton: 25th anniversary. *Molecular Biology of the Cell*, 28(3):357–358, feb 2017. PMID: 28137947.

[18] Daniel A Fletcher and R Dyche Mullins. Cell mechanics and the cytoskeleton. *Nature*, 463(7280):485–492, 2010.

[19] Jingchao Wu and Anna Akhmanova. Microtubule-organizing centers. *Annual review of cell and developmental biology*, 33:51–75, 2017.

[20] Paul Weiss. From cell to molecule. the molecular control of cellular activity. *JM Allen, McGraw-Hill Book Co*, 1962.

[21] Marko Radulovic and Jasminka Godovac-Zimmermann. Proteomic approaches to understanding the role of the cytoskeleton in host-

defense mechanisms. *Expert Review of Proteomics*, 8(1):117–126, 2011.

[22] Ildiko Szeverenyi, Andrew J Cassidy, Cheuk Wang Chung, Bernett TK Lee, John EA Common, Stephen C Ogg, Huijia Chen, Shu Yin Sim, Walter LP Goh, Kee Woei Ng, et al. The human intermediate filament database: comprehensive information on a gene family involved in many human diseases. *Human mutation*, 29(3):351–360, 2008.

[23] A. W. C. Lau, B. D. Hoffman, A. Davies, J. C. Crocker, and T. C. Lubensky. Microrheology, stress fluctuations, and active behavior of living cells. *Physical Review Letters*, 91(19), nov 2003.

[24] Geoffrey M Cooper, Robert E Hausman, and Robert E Hausman. *The cell: a molecular approach*, volume 4. ASM press Washington, DC, 2007.

[25] A Ott, M Magnasco, A Simon, and A Libchaber. Measurement of the persistence length of polymerized actin using fluorescence microscopy. *Physical Review E*, 48(3):R1642, 1993.

[26] H Isambert and AC Maggs. Dynamics and rheology of actin solutions. *Macromolecules*, 29(3):1036–1040, 1996.

[27] Francesco Pampaloni, Gianluca Lattanzi, Alexandr Jonáš, Thomas Surrey, Erwin Frey, and Ernst-Ludwig Florin. Thermal fluctuations of grafted microtubules provide evidence of a length-dependent persistence length. *Proceedings of the National Academy of Sciences*, 103(27):10248–10253, 2006.

[28] MGL Van den Heuvel, S Bolhuis, and C Dekker. Persistence length

measurements from stochastic single-microtubule trajectories. *Nano letters*, 7(10):3138–3144, 2007.

[29] Julie A Theriot and Timothy J Mitchison. Actin microfilament dynamics in locomoting cells. *Nature*, 352(6331):126–131, 1991.

[30] Klemens Rottner and Theresia EB Stradal. Actin dynamics and turnover in cell motility. *Current opinion in cell biology*, 23(5):569–578, 2011.

[31] Jeanne N Jodoin, Jonathan S Coravos, Soline Chanet, Claudia G Vasquez, Michael Tworoger, Elena R Kingston, Lizabeth A Perkins, Norbert Perrimon, and Adam C Martin. Stable force balance between epithelial cells arises from f-actin turnover. *Developmental cell*, 35(6):685–697, 2015.

[32] K. M. Smurova, A. A. Birukova, A. D. Verin, and I. B. Alieva. Dose-dependent effect of nocodazole on endothelial cell cytoskeleton. *Biochemistry (Moscow) Supplement Series A: Membrane and Cell Biology*, 2(2):119, July 2008.

[33] Dimitrije Stamenovic, Srboljub M Mijailovich, Iva Marija Tolić-Nørrelykke, Jianxin Chen, and Ning Wang. Cell prestress. ii. contribution of microtubules. *American Journal of Physiology-Cell Physiology*, 282(3):C617–C624, 2002.

[34] Jitao Zhang, Farid Alisafaei, Miloš Nikolić, Xuefei A Nou, Hanyoup Kim, Vivek B Shenoy, and Giuliano Scarcelli. Nuclear mechanics within intact cells is regulated by cytoskeletal network and internal nanostructures, brillouin. *Small*, 16(18):1907688, 2020.

[35] Chuanyue Wu. Focal adhesion: a focal point in current cell biology and molecular medicine. *Cell adhesion & migration*, 1(1):13–18, 2007.

[36] S Wiesner, KR Legate, and R Fässler. Integrin-actin interactions. *Cellular and Molecular Life Sciences CMLS*, 62(10):1081–1099, 2005.

[37] Yongliang Wang and Xuefeng Wang. Integrins outside focal adhesions transmit tensions during stable cell adhesion. *Scientific reports*, 6(1):1–9, 2016.

[38] Francis J Alenghat and Donald E Ingber. Mechanotransduction: all signals point to cytoskeleton, matrix, and integrins. *Science's STKE*, 2002(119):pe6–pe6, 2002.

[39] John R Masters. Hela cells 50 years on: the good, the bad and the ugly. *Nature Reviews Cancer*, 2(4):315–319, 2002.

[40] Zaken, Ministerie van Algemene. Abortion - government.nl. *www.government.nl/* retrieved 2024-02-10., 2015.

[41] Duncan Wilson. A troubled past? reassessing ethics in the history of tissue culture. *Health Care Analysis*, 24:246–259, 2016.

[42] Terhi Riikonen, Pia Vihinen, Marita Potila, Wolfgang Rettig, and Jyrki Heino. Antibody against human $\alpha 1\beta 1$ integrin inhibits hela cell adhesion to laminin and to type i, iv, and v collagens. *Biochemical and biophysical research communications*, 209(1):205–212, 1995.

[43] Melissa S Maginnis, J Craig Forrest, Sarah A Kopecky-Bromberg, S Kent Dickeson, Samuel A Santoro, Mary M Zutter, Glen R Nemerow, Jeffrey M Bergelson, and Terence S Dermody. $\beta 1$ integrin mediates internalization of mammalian reovirus. *Journal of virology*, 80(6):2760–2770, 2006.

[44] Ning Wang, James P Butler, and Donald E Ingber. Mechanotransduction across the cell surface and through the cytoskeleton. *Science*, 260(5111):1124–1127, 1993.

[45] Donald E Ingber. Cellular basis of mechanotransduction. *The Biological Bulletin*, 194(3):323–327, 1998.

[46] J H. C. Wang and B P. Thampatty. An introductory review of cell mechanobiology. *Biomechanics and Modeling in Mechanobiology*, 5(1):1–16, jan 2006.

[47] JMt Mitchison and MM Swann. The mechanical properties of the cell surface. *J. exp. Biol*, 31(3):443–460, 1954.

[48] Andreas R Bausch, Winfried Möller, and Erich Sackmann. Measurement of local viscoelasticity and forces in living cells by magnetic tweezers. *Biophysical journal*, 76(1):573–579, 1999.

[49] Jochen Guck, Revathi Ananthakrishnan, Hamid Mahmood, Tess J. Moon, C. Casey Cunningham, and Josef Käs. The Optical Stretcher: A Novel Laser Tool to Micromanipulate Cells. *Biophysical Journal*, 81(2):767–784, August 2001.

[50] Ben Fabry, Geoffrey N. Maksym, James P. Butler, Michael Glogauer, Daniel Navajas, and Jeffrey J. Fredberg. Scaling the Microrheology of Living Cells. *Physical Review Letters*, 87(14):148102, September 2001.

[51] Giuliano Scarcelli, Pilhan Kim, and Seok Hyun Yun. In Vivo Measurement of Age-Related Stiffening in the Crystalline Lens by Brillouin Optical Microscopy, brillouin. *Biophysical Journal*, 101(6):1539–1545, September 2011.

[52] Pei-Hsun Wu, Christopher M Hale, Wei-Chiang Chen, Jerry SH Lee, Yiider Tseng, and Denis Wirtz. High-throughput ballistic injection nanorheology to measure cell mechanics. *Nature protocols*, 7(1):155–170, 2012.

[53] Cheng Zhu, Gang Bao, and Ning Wang. Cell mechanics: mechanical response, cell adhesion, and molecular deformation. *Annual review of biomedical engineering*, 2(1):189–226, 2000.

[54] D. Stamenovic and D. E. Ingber. Models of cytoskeletal mechanics of adherent cells. *Biomechanics and Modeling in Mechanobiology*, 1(1):95–108, jun 2002.

[55] C. T. Lim, E. H. Zhou, and S. T. Quek. Mechanical models for living cells—a review. *Journal of Biomechanics*, 39(2):195–216, January 2006.

[56] John M Tarbell and MY Pahakis. Mechanotransduction and the glycocalyx. *Journal of internal medicine*, 259(4):339–350, 2006.

[57] Zhiqi Sun, Shengzhen S Guo, and Reinhard Fässler. Integrin-mediated mechanotransduction. *Journal of Cell Biology*, 215(4):445–456, 2016.

[58] Heriberto Moran, Limary M Cancel, Peigen Huang, Sylvie Roberge, Tuoye Xu, John M Tarbell, and Lance L Munn. Glycocalyx mechanotransduction mechanisms are involved in renal cancer metastasis. *Matrix Biology Plus*, 13:100100, 2022.

[59] Jochen Guck, Stefan Schinkinger, Bryan Lincoln, Falk Wottawah, Susanne Ebert, Maren Romeyke, Dominik Lenz, Harold M. Erickson, Revathi Ananthakrishnan, Daniel Mitchell, Josef Käs, Sydney Ulvick, and Curt Bilby. Optical deformability as an inherent cell marker for testing malignant transformation and metastatic competence. *Biophysical Journal*, 88(5):3689–3698, may 2005.

[60] Franziska Lautenschläger, Stephan Paschke, Stefan Schinkinger, Arlette Bruel, Michael Beil, and Jochen Guck. The regulatory role of cell

mechanics for migration of differentiating myeloid cells. *Proceedings of the National Academy of Sciences*, 106(37):15696–15701, 2009.

[61] Dino Di Carlo. A mechanical biomarker of cell state in medicine. *Journal of laboratory automation*, 17(1):32–42, 2012.

[62] Fu-Shi Quan and Kyung Sook Kim. Medical applications of the intrinsic mechanical properties of single cells. *Acta biochimica et biophysica Sinica*, 48(10):865–871, 2016.

[63] Peter Sollich. Rheological constitutive equation for a model of soft glassy materials. *Physical Review E*, 58(1):738, 1998.

[64] Guillaume Lenormand, Predrag Bursac, James P Butler, and Jeffrey J Fredberg. Out-of-equilibrium dynamics in the cytoskeleton of the living cell. *Physical Review E*, 76(4):041901, 2007.

[65] Paul Beard. Biomedical photoacoustic imaging. *Interface focus*, 1(4):602–631, 2011.

[66] Katsutoshi Miura and Seiji Yamamoto. A scanning acoustic microscope discriminates cancer cells in fluid. *Scientific Reports*, 5(1):15243, 2015.

[67] Fernando Pérez-Cota, Salvatore La Cavera III, Shakila Naznin, Rafael Fuentes-Domínguez, Richard J. Smith, and Matt Clark. Apparent attenuation by opto-acoustic defocus in phonon microscopy, brillouin. *Photoacoustics*, 19:100180, September 2020.

[68] Fan Yang, Carlo Bevilacqua, Sebastian Hambura, Ana Neves, Anusha Gopalan, Koki Watanabe, Matt Govendir, Maria Bernabeu, Jan Ellenberg, Alba Diz-Muñoz, et al. Pulsed stimulated brillouin microscopy enables high-sensitivity mechanical imaging of live and fragile biological specimens. *Nature Methods*, pages 1–9, 2023.

[69] Andreas R Bausch, Florian Ziemann, Alexei A Boulbitch, Ken Jacobson, and Erich Sackmann. Local measurements of viscoelastic parameters of adherent cell surfaces by magnetic bead microrheometry. *Biophysical journal*, 75(4):2038–2049, 1998.

[70] Robert M Hochmuth. Micropipette aspiration of living cells. *Journal of biomechanics*, 33(1):15–22, 2000.

[71] Oliver Otto, Philipp Rosendahl, Alexander Mietke, Stefan Golfier, Christoph Herold, Daniel Klaue, Salvatore Girardo, Stefano Pagliara, Andrew Ekpenyong, Angela Jacobi, et al. Real-time deformability cytometry: on-the-fly cell mechanical phenotyping. *Nature methods*, 12(3):199–202, 2015.

[72] Young Zoon Yoon, Jurij Kotar, Aidan T. Brown, and Pietro Cicuta. Red blood cell dynamics: from spontaneous fluctuations to non-linear response. *Soft Matter*, 7(5):2042–2051, 2011.

[73] Vahid Sheikh-Hasani, Mehrad Babaei, Ali Azadbakht, Hamidreza Pazoki-Toroudi, Alireza Mashaghi, Ali Akbar Moosavi-Movahedi, and Seyed Nader Seyed Reihani. Atorvastatin treatment softens human red blood cells: an optical tweezers study. *Biomedical optics express*, 9(3):1256–1261, 2018.

[74] Nils M Kronenberg, Philipp Liehm, Anja Steude, Johanna A Knipper, Jessica G Borger, Giuliano Scarcelli, Kristian Franze, Simon J Powis, and Malte C Gather. Long-term imaging of cellular forces with high precision by elastic resonator interference stress microscopy, brillouin. *Nature cell biology*, 19(7):864–872, 2017.

[75] Robert W Style, Rostislav Boltyanskiy, Guy K German, Callen Hyland, Christopher W MacMinn, Aaron F Mertz, Larry A Wilen,

Ye Xu, and Eric R Dufresne. Traction force microscopy in physics and biology. *Soft matter*, 10(23):4047–4055, 2014.

[76] Ning Cai, Alvin Chi-Keung Lai, Kin Liao, Peter R Corridon, David J Graves, and Vincent Chan. Recent advances in fluorescence recovery after photobleaching for decoupling transport and kinetics of biomacromolecules in cellular physiology. *Polymers*, 14(9):1913, 2022.

[77] Francesca Palombo and Daniele Fioretto. Brillouin light scattering: applications in biomedical sciences. *Chemical reviews*, 119(13):7833–7847, 2019.

[78] Giuseppe Antonacci, Timon Beck, Alberto Bilenca, Jürgen Czarske, Kareem Elsayad, Jochen Guck, Kyoohyun Kim, Benedikt Krug, Francesca Palombo, Robert Prevedel, et al. Recent progress and current opinions in brillouin microscopy for life science applications. *Biophysical Reviews*, 12(3):615–624, 2020.

[79] William Hardiman, Matt Clark, Claire Friel, Alan Huett, Fernando Pérez-Cota, Kerry Setchfield, Manlio Tassieri, and Amanda J. Wright. Living cells as a biological analog of optical tweezers – a non-invasive microrheology approach. *Acta Biomaterialia*, 2023.

[80] Lap Man Lee and Allen P Liu. The application of micropipette aspiration in molecular mechanics of single cells. *Journal of nanotechnology in engineering and medicine*, 5(4), 2014.

[81] Marta Urbanska, Hector E Muñoz, Josephine Shaw Bagnall, Oliver Otto, Scott R Manalis, Dino Di Carlo, and Jochen Guck. A comparison of microfluidic methods for high-throughput cell deformability measurements. *Nature methods*, 17(6):587–593, 2020.

[82] Enrique A López-Guerra and Santiago D Solares. Modeling viscoelasticity through spring–dashpot models in intermittent-contact atomic force microscopy. *Beilstein journal of nanotechnology*, 5(1):2149–2163, 2014.

[83] Kristina Haase and Andrew E Pelling. Investigating cell mechanics with atomic force microscopy. *Journal of The Royal Society Interface*, 12(104):20140970, 2015.

[84] Igor Sokolov. Atomic force microscopy in cancer cell research. *Cancer nanotechnology*, 1:1–17, 2007.

[85] GH Kim, P Kosterin, AL Obaid, and BM Salzberg. A mechanical spike accompanies the action potential in mammalian nerve terminals. *Biophysical journal*, 92(9):3122–3129, 2007.

[86] Charlotte Alibert, Bruno Goud, and Jean-Baptiste Manneville. Are cancer cells really softer than normal cells? *Biology of the Cell*, 109(5):167–189, 2017.

[87] Emad Moeendarbary, Léo Valon, Marco Fritzsche, Andrew R Harris, Dale A Moulding, Adrian J Thrasher, Eleanor Stride, L Mahadevan, and Guillaume T Charras. The cytoplasm of living cells behaves as a poroelastic material. *Nature materials*, 12(3):253–261, 2013.

[88] Peter Sollich, François Lequeux, Pascal Hébraud, and Michael E Cates. Rheology of soft glassy materials. *Physical review letters*, 78(10):2020, 1997.

[89] Steven S An, Ben Fabry, Mathew Mellema, Predrag Bursac, William T Gerthoffer, Usamah S Kayyali, Matthias Gaestel, Stephanie A Shore, and Jeffrey J Fredberg. Role of heat shock pro-

tein 27 in cytoskeletal remodeling of the airway smooth muscle cell. *Journal of applied physiology*, 96(5):1701–1713, 2004.

[90] Predrag Bursac, Guillaume Lenormand, Ben Fabry, Madavi Oliver, David A Weitz, Virgile Viasnoff, James P Butler, and Jeffrey J Fredberg. Cytoskeletal remodelling and slow dynamics in the living cell. *Nature materials*, 4(7):557–561, 2005.

[91] Guillaume Lenormand, Emil Millet, Chan Young Park, C Corey Hardin, James P Butler, Nicanor I Moldovan, and Jeffrey J Fredberg. Dynamics of the cytoskeleton: How much does water matter? *Physical Review E*, 83(6):061918, 2011.

[92] Rolf D Hubmayr, Stephanie A Shore, Jeffrey J Fredberg, Emanuelle Planus, RA Panettieri Jr, Winfried Moller, Joachim Heyder, and Ning Wang. Pharmacological activation changes stiffness of cultured human airway smooth muscle cells. *American Journal of Physiology-Cell Physiology*, 271(5):C1660–C1668, 1996.

[93] Fernando Pérez-Cota, Rafael Fuentes-Domínguez, Salvatore La Cavera, William Hardiman, Mengting Yao, Kerry Setchfield, Emilia Moradi, Shakila Naznin, Amanda Wright, Kevin F Webb, et al. Picosecond ultrasonics for elasticity-based imaging and characterization of biological cells. *Journal of Applied Physics*, 128(16):160902, 2020.

[94] Fernando Pérez-Cota, Richard J. Smith, Hany M. Elsheikha, and Matt Clark. New insights into the mechanical properties of acanthamoeba castellanii cysts as revealed by phonon microscopy, brillouin. *Biomedical Optics Express*, 10(5):2399, April 2019.

[95] Itay Remer, Roni Shaashoua, Netta Shemesh, Anat Ben-Zvi, and Alberto Bilenca. High-sensitivity and high-specificity biomechanical

imaging by stimulated brillouin scattering microscopy. *Nature Methods*, 17(9):913–916, 2020.

[96] Tomasz Kalwarczyk, Natalia Ziębacz, Anna Bielejewska, Ewa Zaboklicka, Kaloian Koynov, Jędrzej Szymanński, Agnieszka Wilk, Adam Patkowski, Jacek Gapinński, Hans-J urgen Butt, and Robert Hołyst. Comparative analysis of viscosity of complex liquids and cytoplasm of mammalian cells at the nanoscale. *Nano Letters*, 11(5):2157–2163, may 2011.

[97] Kenji Nishizawa, Kei Fujiwara, Masahiro Ikenaga, Nobushige Nakajo, Miho Yanagisawa, and Daisuke Mizuno. Universal glass-forming behavior of in vitro and living cytoplasm. *Scientific reports*, 7(1):15143, 2017.

[98] Venkat Maruthamuthu, Benedikt Sabass, Ulrich S Schwarz, and Margaret L Gardel. Cell-ecm traction force modulates endogenous tension at cell–cell contacts. *Proceedings of the National Academy of Sciences*, 108(12):4708–4713, 2011.

[99] Philipp Liehm, Nils Michael Kronenberg, and Malte Christian Gather. Analysis of the precision, robustness, and speed of elastic resonator interference stress microscopy. *Biophysical Journal*, 114(9):2180–2193, 2018.

[100] Michael T Yang, Daniel H Reich, and Christopher S Chen. Measurement and analysis of traction force dynamics in response to vasoactive agonists. *Integrative biology*, 3(6):663–674, 2011.

[101] Porntula Panorchan, Jerry SH Lee, Thomas P Kole, Yiider Tseng, and Denis Wirtz. Microrheology and rock signaling of human endothelial cells embedded in a 3d matrix. *Biophysical journal*, 91(9):3499–3507, 2006.

[102] Jerry SH Lee, Porntula Panorchan, Christopher M Hale, Shyam B Khatau, Thomas P Kole, Yiider Tseng, and Denis Wirtz. Ballistic intracellular nanorheology reveals rock-hard cytoplasmic stiffening response to fluid flow. *Journal of cell science*, 119(9):1760–1768, 2006.

[103] Hiroyuki Ebata, Katsuhiro Umeda, Kenji Nishizawa, Wataru Nagao, Shono Inokuchi, Yujiro Sugino, Takafumi Miyamoto, and Daisuke Mizuno. Activity-dependent glassy cell mechanics : Mechanical properties measured with active microrheology. *Biophysical Journal*, 122(10):1781–1793, 2023.

[104] Giuseppe Antonacci, Matthew R Foreman, Carl Paterson, and Peter Török. Spectral broadening in brillouin imaging. *Applied Physics Letters*, 103(22), 2013.

[105] Carlo Bevilacqua, Juan Manuel Gomez, Ulla-Maj Fiuza, Chii Jou Chan, Ling Wang, Sebastian Hambura, Manuel Eguren, Jan Ellenberg, Alba Diz-Muñoz, Maria Leptin, et al. High-resolution line-scan brillouin microscopy for live imaging of mechanical properties during embryo development. *Nature Methods*, 20(5):755–760, 2023.

[106] Raimund Schlüßler, Stephanie Möllmert, Shada Abuhattum, Gheorghe Cojoc, Paul Müller, Kyoohyun Kim, Conrad Möckel, Conrad Zimmermann, Jürgen Czarske, and Jochen Guck. Mechanical mapping of spinal cord growth and repair in living zebrafish larvae by brillouin imaging. *Biophysical journal*, 115(5):911–923, 2018.

[107] Pei-Jung Wu, Irina V Kabakova, Jeffrey W Ruberti, Joseph M Sherwood, Iain E Dunlop, Carl Paterson, Peter Török, and Darryl R Overby. Water content, not stiffness, dominates brillouin spectroscopy measurements in hydrated materials. *Nature methods*, 15(8):561–562, 2018.

[108] Michelle Bailey, Martina Alunni-Cardinali, Noemi Correa, Silvia Caponi, Timothy Holsgrove, Hugh Barr, Nick Stone, C Peter Winlove, Daniele Fioretto, and Francesca Palombo. Viscoelastic properties of biopolymer hydrogels determined by brillouin spectroscopy: A probe of tissue micromechanics. *Science advances*, 6(44):eabc1937, 2020.

[109] RML Evans, Manlio Tassieri, Dietmar Auhl, and Thomas A Waigh. Direct conversion of rheological compliance measurements into storage and loss moduli. *Physical Review E*, 80(1):012501, 2009.

[110] Adolf Fick. Ueber diffusion. *Annalen der Physik*, 170(1):59–86, 1855.

[111] Yun Ling, Martin Lysy, Ian Seim, Jay Newby, David B Hill, Jeremy Cribb, and M Gregory Forest. Measurement error correction in particle tracking microrheology. *The Annals of Applied Statistics*, 16(3):1747–1773, 2022.

[112] Thomas G Mason and David A Weitz. Optical measurements of frequency-dependent linear viscoelastic moduli of complex fluids. *Physical review letters*, 74(7):1250, 1995.

[113] Jingyuan Xu, Virgile Viasnoff, and Denis Wirtz. Compliance of actin filament networks measured by particle-tracking microrheology and diffusing wave spectroscopy. *Rheologica acta*, 37(4):387–398, 1998.

[114] Thomas G Mason, Kavita Ganesan, J Harry van Zanten, Denis Wirtz, and Scot C Kuo. Particle tracking microrheology of complex fluids. *Physical review letters*, 79(17):3282, 1997.

[115] Manlio Tassieri. Microrheology with optical tweezers: peaks & troughs. *Current Opinion in Colloid & Interface Science*, 43:39–51, oct 2019.

[116] Manlio Tassieri. Comment on "a symmetrical method to obtain shear moduli from microrheology" by k. nishi, ml kilfoil, cf schmidt, and fc mackintosh, soft matter, 2018, 14, 3716. *Soft Matter*, 14(42):8666–8670, 2018.

[117] Manlio Tassieri, RML Evans, Rebecca L Warren, Nicholas J Bailey, and Jonathan M Cooper. Microrheology with optical tweezers: data analysis. *New Journal of Physics*, 14(11):115032, 2012.

[118] Kengo Nishi, Maria L Kilfoil, Christoph F Schmidt, and Fred C MacKintosh. A symmetrical method to obtain shear moduli from microrheology. *Soft matter*, 14(19):3716–3723, 2018.

[119] Taiki Yanagishima, Daan Frenkel, Jurij Kotar, and Erika Eiser. Real-time monitoring of complex moduli from micro-rheology. *Journal of physics: Condensed matter*, 23(19):194118, 2011.

[120] J-Z Xue, DJ Pine, Scott Thomas Milner, X-L Wu, and PM Chaikin. Nonergodicity and light scattering from polymer gels. *Physical Review A*, 46(10):6550, 1992.

[121] Alex J Levine and TC Lubensky. Response function of a sphere in a viscoelastic two-fluid medium. *Physical Review E*, 63(4):041510, 2001.

[122] Alex J Levine and TC Lubensky. One-and two-particle microrheology. *Physical review letters*, 85(8):1774, 2000.

[123] B Schnurr, F Gittes, FC MacKintosh, and CF Schmidt. Determining microscopic viscoelasticity in flexible and semiflexible polymer networks from thermal fluctuations. *Macromolecules*, 30(25):7781–7792, 1997.

[124] F Gittes, BDOP Schnurr, PD Olmsted, Fred C MacKintosh, and Christoph F Schmidt. Microscopic viscoelasticity: shear moduli of soft materials determined from thermal fluctuations. *Physical review letters*, 79(17):3286, 1997.

[125] Alex J Levine and TC Lubensky. Two-point microrheology and the electrostatic analogy. *Physical Review E*, 65(1):011501, 2001.

[126] John C Crocker, Megan T Valentine, Eric R Weeks, Thomas Gisler, Peter D Kaplan, Arjun G Yodh, and David A Weitz. Two-point microrheology of inhomogeneous soft materials. *Physical Review Letters*, 85(4):888, 2000.

[127] Keir C Neuman and Steven M Block. Optical trapping. *Review of scientific instruments*, 75(9):2787–2809, sep 2004.

[128] Julius Adams Stratton. *Electromagnetic theory / by Julius Adams Stratton ; IEEE Antennas and Propagation Society, sponsor.* IEEE press series on electromagnetic wave theory. John Wiley & Sons, Inc., 2015.

[129] Arthur Ashkin, James M Dziedzic, JE Bjorkholm, and Steven Chu. Observation of a single-beam gradient force optical trap for dielectric particles. *Optics letters*, 11(5):288–290, 1986.

[130] Thomas Andrew Waigh. Advances in the microrheology of complex fluids. *Reports on Progress in Physics*, 79(7):074601, 2016.

[131] Arthur Ashkin and James M Dziedzic. Optical trapping and manipulation of viruses and bacteria. *Science*, 235(4795):1517–1520, 1987.

[132] David G. Glass, Niall McAlinden, Owain R. Millington, and Amanda J. Wright. A minimally invasive optical trapping system

to understand cellular interactions at onset of an immune response. *PLOS ONE*, 12(12):e0188581, December 2017.

[133] Niall McAlinden, David G Glass, Owain Millington, and Amanda J Wright. Viability studies of optically trapped t-cells. In *Optical Trapping and Optical Micromanipulation VIII*, volume 8097, pages 128–137. SPIE, 2011.

[134] Charlotte Alibert, David Pereira, Nathan Lardier, Sandrine Etienne-Manneville, Bruno Goud, Atef Asnacios, and Jean-Baptiste Manneville. Multiscale rheology of glioma cells. *Biomaterials*, 275:120903, 2021.

[135] Carlo Bradac. Nanoscale optical trapping: a review. *Advanced Optical Materials*, 6(12):1800005, 2018.

[136] Léon Brillouin. Diffusion de la lumière et des rayons x par un corps transparent homogène, brillouin. In *Annales de physique*, volume 9, pages 88–122, 1922.

[137] LI Mandelstam. Light scattering by inhomogeneous media. *Zh. Russ. Fiz-Khim. Ova*, 58(381):146, 1926.

[138] Immanuil L Fabelinskiĭ. Seventy years of combination (raman) scattering. *Physics-Uspekhi*, 41(12):1229, 1998.

[139] Chandrasekhara Venkata Raman and Kariamanikkam Srinivasa Krishnan. A new type of secondary radiation. *Nature*, 121(3048):501–502, 1928.

[140] Gr Landsberg and L Mandelstam. A novel effect of light scattering in crystals. *Naturwissenschaften*, 16(557), 1928.

[141] Predrag Bursac, Ben Fabry, Xavier Trepat, Guillaume Lenormand, James P Butler, Ning Wang, Jeffrey J Fredberg, and Steven S An. Cytoskeleton dynamics: fluctuations within the network. *Biochemical and biophysical research communications*, 355(2):324–330, 2007.

[142] William Hardiman. Optrap-analysis (github repository), 2018.

[143] Manlio Tassieri, Graham M Gibson, RML Evans, Alison M Yao, Rebecca Warren, Miles J Padgett, and Jonathan M Cooper. Measuring storage and loss moduli using optical tweezers: Broadband microrheology. *Physical Review E*, 81(2):026308, 2010.

[144] Daryl Preece, Rebecca Warren, RML Evans, Graham M Gibson, Miles J Padgett, Jonathan M Cooper, and Manlio Tassieri. Optical tweezers: wideband microrheology. *Journal of optics*, 13(4):044022, 2011.

[145] Mohammad Sarshar, Winson Wong, and Bahman Anvari. Comparative study of methods to calibrate the stiffness of a single-beam gradient-force optical tweezers over various laser trapping powers. *Journal of biomedical optics*, 19(11):115001, 2014.

[146] Amanda J. Wright, Tiffany A. Wood, Mark R. Dickinson, Helen F. Gleeson, and Tom Mullin. The transverse trapping force of an optical trap: Factors affecting its measurement. *Journal of Modern Optics*, 50(10):1521–1532, July 2003.

[147] Arthur Edelstein, Nenad Amodaj, Karl Hoover, Ron Vale, and Nico Stuurman. Computer control of microscopes using μmanager. *Current protocols in molecular biology*, 92(1):14–20, 2010.

[148] Caroline A Schneider, Wayne S Rasband, and Kevin W Eliceiri.

Nih image to imagej: 25 years of image analysis. *Nature methods*, 9(7):671–675, 2012.

[149] Nadine Tarantino, Jean-Yves Tinevez, Elizabeth Faris Crowell, Bertrand Boisson, Ricardo Henriques, Musa Mhlanga, Fabrice Agou, Alain Israël, and Emmanuel Laplantine. Tnf and il-1 exhibit distinct ubiquitin requirements for inducing nemo–ikk supramolecular structures. *Journal of Cell Biology*, 204(2):231–245, 2014.

[150] Andrew B Matheson, Lynn Paterson, Amanda J Wright, Tania Mendonca, Manlio Tassieri, and Paul A Dalgarno. Optical tweezers with integrated multiplane microscopy (optimum): a new tool for 3d microrheology. *Scientific reports*, 11(1):1–9, 2021.

[151] Aneesur Rahman. Correlations in the motion of atoms in liquid argon. *Physical review*, 136(2A):A405, 1964.

[152] Eric R Weeks and DA Weitz. Properties of cage rearrangements observed near the colloidal glass transition. *Physical review letters*, 89(9):095704, 2002.

[153] Matthew G Smith, Graham M Gibson, and Manlio Tassieri. i-rheoft: Fourier transforming sampled functions without artefacts. *Scientific reports*, 11(1):1–12, 2021.

[154] Thierry Savin and Patrick S. Doyle. Static and Dynamic Errors in Particle Tracking Microrheology. *Biophysical Journal*, 88(1):623–638, jan 2005.

[155] Thierry Savin and Patrick S. Doyle. Role of a finite exposure time on measuring an elastic modulus using microrheology. *Physical Review E*, 71(4), apr 2005.

[156] Giorgio Volpe and Giovanni Volpe. Simulation of a brownian particle in an optical trap. *American Journal of Physics*, 81(3):224–230, 2013.

[157] F Gittes and FC MacKintosh. Dynamic shear modulus of a semiflexible polymer network. *Physical Review E*, 58(2):R1241, 1998.

[158] Olga Adamczyk, Zbigniew Baster, Maksymilian Szczypior, and Zenon Rajfur. Substrate stiffness mediates formation of novel cytoskeletal structures in fibroblasts during cell–microspheres interaction. *International journal of molecular sciences*, 22(2):960, 2021.

[159] R Alon, EA Bayer, and M Wilchek. Cell adhesion to streptavidin via rgd-dependent integrins. *European journal of cell biology*, 60(1):1–11, 1993.

[160] Carol Jurchenko, Yuan Chang, Yoshie Narui, Yun Zhang, and Khalid S Salaita. Integrin-generated forces lead to streptavidin-biotin unbinding in cellular adhesions. *Biophysical journal*, 106(7):1436–1446, 2014.

[161] Christa G. Walther, Robert Whitfield, and David C. James. Importance of interaction between integrin and actin cytoskeleton in suspension adaptation of CHO cells. *Applied Biochemistry and Biotechnology*, 178(7):1286–1302, dec 2015.

[162] Ning Wang and Donald E Ingber. Control of cytoskeletal mechanics by extracellular matrix, cell shape, and mechanical tension. *Biophysical journal*, 66(6):2181–2189, 1994.

[163] Ning Wang, Iva Marija Tolic-Nørrelykke, Jianxin Chen, Srboljub M Mijailovich, James P Butler, Jeffrey J Fredberg, and Dimitrije Stamenovic. Cell prestress. i. stiffness and prestress are closely associated

in adherent contractile cells. *American Journal of Physiology-Cell Physiology*, 282(3):C606–C616, 2002.

[164] Susan L Bellis. Advantages of rgd peptides for directing cell association with biomaterials. *Biomaterials*, 32(18):4205–4210, 2011.

[165] Mark S Johnson, Ning Lu, Konstantin Denessiouk, Jyrki Heino, and Donald Gullberg. Integrins during evolution: evolutionary trees and model organisms. *Biochimica et Biophysica Acta (BBA)-Biomembranes*, 1788(4):779–789, 2009.

[166] Ben Fabry, Geoffrey N Maksym, James P Butler, Michael Glogauer, Daniel Navajas, Nathan A Taback, Emil J Millet, and Jeffrey J Fredberg. Time scale and other invariants of integrative mechanical behavior in living cells. *Physical Review E*, 68(4):041914, 2003.

[167] Daisuke Mizuno, DA Head, FC MacKintosh, and CF Schmidt. Active and passive microrheology in equilibrium and nonequilibrium systems. *Macromolecules*, 41(19):7194–7202, 2008.

[168] Donald E Ingber. Cellular tensegrity: defining new rules of biological design that govern the cytoskeleton. *Journal of cell science*, 104(3):613–627, 1993.

[169] Dimitrije Stamenović, Jeffrey J. Fredberg, Ning Wang, James P. Butler, and Donald E. Ingber. A Microstructural Approach to Cytoskeletal Mechanics based on Tensegrity. *Journal of Theoretical Biology*, 181(2):125–136, July 1996.

[170] D.E. Ingber, S.R. Heidemann, P. Lamoureux, and R.E. Buxbaum. Opposing views on tensegrity as a structural framework for understanding cell mechanics. *Journal of Applied Physiology*, 2000.

[171] Donald E Ingber. Tensegrity i. cell structure and hierarchical systems biology. *Journal of cell science*, 116(7):1157–1173, 2003.

[172] Manlio Tassieri. Linear microrheology with optical tweezers of living cells 'is not an option'! *Soft Matter*, 11(29):5792–5798, 2015.

[173] Fernando Pérez-Cota, Richard J Smith, Emilia Moradi, Leonel Marques, Kevin F Webb, and Matt Clark. Thin-film optoacoustic transducers for subcellular brillouin oscillation imaging of individual biological cells. *Applied optics*, 54(28):8388–8398, September 2015.

[174] Richard J Smith, Fernando Pérez-Cota, Leonel Marques, and Matt Clark. 3d phonon microscopy with sub-micron axial-resolution. *Scientific Reports*, 11(1):1–10, 2021.

[175] Richard J Smith, Fernando Pérez-Cota Cota, Leonel Marques, Xuesheng Chen, Ahmet Arca, Kevin Webb, Jonathon Aylott, Micheal G Somekh, and Matt Clark. Optically excited nanoscale ultrasonic transducers. *The Journal of the Acoustical Society of America*, 137(1):219–227, 2015.

[176] A Assion, M Geisler, J Helbing, V Seyfried, and T Baumert. Femtosecond pump-probe photoelectron spectroscopy: Mapping of vibrational wave-packet motion. *Physical Review A*, 54(6):R4605, 1996.

[177] Martin C Fischer, Jesse W Wilson, Francisco E Robles, and Warren S Warren. Invited review article: pump-probe microscopy. *Review of Scientific Instruments*, 87(3):031101, 2016.

[178] Osamu Matsuda, Maria Cristina Larciprete, Roberto Li Voti, and Oliver B Wright. Fundamentals of picosecond laser ultrasonics. *Ultrasonics*, 56:3–20, 2015.

[179] John Frederick Nye et al. *Physical properties of crystals: their representation by tensors and matrices.* Oxford university press, 1985.

[180] C Thomsen, Holger T Grahn, Humphrey J Maris, and Jan Tauc. Surface generation and detection of phonons by picosecond light pulses. *Physical Review B*, 34(6):4129, 1986.

[181] Vitalyi E Gusev and Pascal Ruello. Advances in applications of time-domain brillouin scattering for nanoscale imaging. *Applied Physics Reviews*, 5(3):031101, 2018.

[182] Otto L Muskens and Jaap I Dijkhuis. High amplitude, ultrashort, longitudinal strain solitons in sapphire. *Physical review letters*, 89(28):285504, 2002.

[183] Gilad Rosenblatt, Boris Simkhovich, Guy Bartal, and Meir Orenstein. Nonmodal plasmonics: Controlling the forced optical response of nanostructures. *Phys. Rev. X*, 10:011071, Mar 2020.

[184] Vitalyi E Gusev. Detection of nonlinear picosecond acoustic pulses by time-resolved brillouin scattering. *Journal of Applied Physics*, 116(6):064907, 2014.

[185] T Dehoux, B Audoin, O Zouani, and MC Durrieu. Mechanical characterization of temperature-sensitive objects using picosecond ultrasonics. In *Journal of Physics: Conference Series*, volume 278, page 012043. IOP Publishing, 2011.

[186] Mirjam Schürmann, Jana Scholze, Paul Müller, Jochen Guck, and Chii J. Chan. Cell nuclei have lower refractive index and mass density than cytoplasm. *Journal of Biophotonics*, 9(10):1068–1076, 2016.

[187] José Méndez. Density and composition of mammalian muscle. *Metabolism*, 9:184–188, 1960.

[188] Canan Baysal and Ali Rana Atilgan. Relaxation kinetics and the glassiness of native proteins: coupling of timescales. *Biophysical journal*, 88(3):1570–1576, 2005.

[189] KL Ngai, SIMONE Capaccioli, and N Shinyashiki. The protein "glass" transition and the role of the solvent. *The Journal of Physical Chemistry B*, 112(12):3826–3832, 2008.

[190] Irina M Kuznetsova, Konstantin K Turoverov, and Vladimir N Uversky. What macromolecular crowding can do to a protein. *International journal of molecular sciences*, 15(12):23090–23140, 2014.

[191] KL Ngai, R Casalini, Simone Capaccioli, M Paluch, and CM Roland. Do theories of the glass transition, in which the structural relaxation time does not define the dispersion of the structural relaxation, need revision? *The Journal of Physical Chemistry B*, 109(37):17356–17360, 2005.

[192] Liesbeth MC Janssen. Mode-coupling theory of the glass transition: A primer. *Frontiers in Physics*, 6:97, 2018.

[193] Gernot Guigas, Claudia Kalla, and Matthias Weiss. Probing the nanoscale viscoelasticity of intracellular fluids in living cells. *Biophysical journal*, 93(1):316–323, 2007.

[194] Zoran Zivkovic et al. Improved adaptive gaussian mixture model for background subtraction. In *ICPR (2)*, pages 28–31. Citeseer, 2004.

[195] Giuseppe Antonacci and Sietse Braakman. Biomechanics of subcellular structures by non-invasive brillouin microscopy. *Scientific Reports*, 6(1):37217, 2016.

[196] Giuliano Scarcelli, William J Polacheck, Hadi T Nia, Kripa Patel, Alan J Grodzinsky, Roger D Kamm, and Seok Hyun Yun. Noncontact

three-dimensional mapping of intracellular hydromechanical properties by brillouin microscopy. *Nature methods*, 12(12):1132, 2015.

[197] Michael A Model and Ethan Schonbrun. Optical determination of intracellular water in apoptotic cells. *The Journal of Physiology*, 591(23):5843–5849, 2013.

[198] Andrew G Clark, Kai Dierkes, and Ewa K Paluch. Monitoring actin cortex thickness in live cells. *Biophysical journal*, 105(3):570–580, 2013.

[199] James L McGrath, John H Hartwig, Yanik Tardy, and C Forbes Dewey Jr. Measuring actin dynamics in endothelial cells. *Microscopy research and technique*, 43(5):385–394, 1998.

[200] Takushi Miyoshi and Naoki Watanabe. Can filament treadmilling alone account for the f-actin turnover in lamellipodia? *Cytoskeleton*, 70(4):179–190, 2013.

[201] Walter M Morton, Kathryn R Ayscough, and Paul J McLaughlin. Latrunculin alters the actin-monomer subunit interface to prevent polymerization. *Nature cell biology*, 2(6):376–378, 2000.

[202] J Rouch, CC Lai, and SH Chen. Brillouin scattering studies of normal and supercooled water. *The Journal of Chemical Physics*, 65(10):4016–4021, 1976.

[203] Salvatore La Cavera III, Fernando Pérez-Cota, Richard J Smith, and Matt Clark. Phonon imaging in 3d with a fibre probe. *Light: Science & Applications*, 10(1):91, 2021.

[204] Fernando Pérez-Cota, Giovanna Martinez-Arellano, William Hardiman, I. I. I. Salvatore LaCavera, Luke Thornton, Rafael Fuentes-Domínguez, Richard J. Smith, Alan McIntyre, and Matt Clark. Clas-

sification of cancer cells at sub-cellular level by phonon microscopy and deep learning: Towards phonon-based diagnostics. *In preparation*, 2023.

[205] Rafael Fuentes-Domínguez, Mengting Yao, William Hardiman, Kerry Setchfield, Fernando Pérez-Cota, Richard J Smith, Matt Clark, et al. Parallel imaging with phonon microscopy using a multi-core fibre bundle detection. *Photoacoustics*, 31:100493, 2023.

[206] Miloš Nikolić and Giuliano Scarcelli. Long-term brillouin imaging of live cells with reduced absorption-mediated damage at 660nm wavelength. *Biomedical optics express*, 10(4):1567–1580, 2019.

[207] William M Haynes. *CRC handbook of chemistry and physics*. CRC press, 2016.

[208] Thomas A Waigh. Microrheology of complex fluids. *Reports on progress in physics*, 68(3):685, 2005.

[209] Umidahan Djakbarova, Yasaman Madraki, Emily T Chan, and Cömert Kural. Dynamic interplay between cell membrane tension and clathrin-mediated endocytosis. *Biology of the Cell*, 113(8):344–373, 2021.

[210] Thomas Dehoux, Maroun Abi Ghanem, Omar F Zouani, Mathieu Ducousso, Nikolay Chigarev, Clément Rossignol, Nicolas Tsapis, Marie-Christine Durrieu, and Bertrand Audoin. Probing single-cell mechanics with picosecond ultrasonics. *Ultrasonics*, 56:160–171, 2015.

[211] C Rossignol, N Chigarev, M Ducousso, B Audoin, G Forget, F Guillemot, and MC Durrieu. In vitro picosecond ultrasonics in a single cell. *Applied Physics Letters*, 93(12), 2008.

[212] Sorasak Danworaphong, Motonobu Tomoda, Yuki Matsumoto, Osamu Matsuda, Toshiro Ohashi, Hiromu Watanabe, Masafumi Nagayama, Kazutoshi Gohara, Paul H Otsuka, and Oliver B Wright. Three-dimensional imaging of biological cells with picosecond ultrasonics. *Applied physics letters*, 106(16), 2015.

[213] Robert Prevedel, Alba Diz-Muñoz, Giancarlo Ruocco, and Giuseppe Antonacci. Brillouin microscopy: an emerging tool for mechanobiology. *Nature Methods*, 16(10):969–977, sep 2019.

[214] Louise Cramer and Arshad Desai. Fluorescence procedures for the actin and tubulin cytoskeleton in fixed cells, 2012.

Appendices

Appendix A

Github Repository

All code developed for this thesis is available via two Github repositories, OpTrap-Analysis and Phonon, which can be access via my Github profile at https://github.com/beeeel[142]. The OpTrap-Analysis repository is of wider interest so I will now describe the contents. The software tools on this repository are under constant development, however a branch named "thesis" contains the code as-is at time of writing. Included in this repository is a MATLAB class called msdanalyzer which was developed by Jean-Yves Tinevez[149] and modified for use in my analyses.

To use code within this repository, first download the repository using Git; a graphical user interface is available on Windows which trivialises the process. In MATLAB, the relevant folder names need to be added to the path using the 'addpath' command. To use the acquisition scripts, first ensure you have a recent Micro-Manager build. Open Micro-Manager, and in the ImageJ window choose "Plugins", then "Compile" or "Compile and Run", and compile each of the Java classes within the repository folder named "javaImageProcessing".

The analysis code was designed around reusing a *struct* (MATLAB data structure) which begins with just the name of the folder containing the data, and is populated with raw and processed data as subsequent analysis modules are run. The same *struct* can be passed to various plotting commands to show various aspects of the data. This form makes it easy to rapidly inspect data and develop analysis pipelines such as those demonstrated in Chapters 3 and 4. Functions acting upon this *struct*, or those drawing data from it, have names prefixed with 'bead_'.

A.1   Microrheology Data Acquisition

The processing scripts which made microrheology data acquisition possible were developed with the kind support of the Micro-Manager community on the forum *image.sc*. Here I describe the newest version of the acquisition script at the time of writing, 'fast_acq_v9_n.bsh'. The workings of the script are shown in Figure A.1, and I shall now describe the motivation for the design before defining the acquisition and processing parameters which may be ambiguous.

The design of this script was subject to two constraints: firstly, images must be processed in real-time, allowing arbitrarily long acquisitions and compact data for post-processing; secondly, the acquisition process must be simple to reduce opportunities for mistakes such as typing the wrong region of interest (ROI) or overwriting existing data. For these reasons, image processing was implemented in Java and the ROI is drawn by the user and read via the ImageJ API.

The acquisition and processing parameters (except the ROI) are defined within the script, and many are set once and kept constant for a series of

experiments. Acquisition parameters are the file name to save, exposure time for the camera, the acquisition length as number of images (not length of time), and the save interval, *Saveint*; this defines how often to keep an image, typically 1,000 i.e. 0.1% of images are kept after the acquisition; hence it can be verified during post-processing that the bead remains within the ROI or that the threshold was set correctly.

Processing parameters are all used by the centroid algorithm. A simple centroid calculation with threshold was defined in Equation 3.6, and this can be extended by considering a situation with several beads within the ROI. In this case, the ROI is divided along its width according the list of widths called *subWidth* which is defined by the user. For example a 400 pixel wide ROI with 3 beads in may have a *subWidth* specification of $\{130, 130, 140\}$, and the centroid of each "sub-ROI" is calculated independently. Finally, a number of rows at the top and bottom of the ROI may be excluded by analysis by setting the *skipRows* parameter; this is because the Hamamatsu Orca Flash v2 camera used by a colleague has more noise on the top and bottom rows than the rest of the ROI.

The data is written out as a raw bytestream; the 64-bit floating point numbers used within Micro-Manager are stored on disk with the file extension ".dat". This minimises the file sizes and processing required to save and load data. To load them into MATLAB correctly, a function called 'byteStreamToDouble' which takes a filename as its sole argument was written in MATLAB. Due to indexing differences (Java counting from 0 and MATLAB from 1), centroids calculated from the same image using identical code in Java and MATLAB are consistently different by 0.5 pixels; this systematic offset does not affect subsequent analyses.

```
                Start ◄─────────────────────        ┌──────────────────────────┐
                  │                                  │ Acquisition parameters:  │
                  ▼                                  │                          │
            Does data file exist? ──Yes──► Error: overwrite  File name           │
                  │                         prevented       Drawn ROI            │
                  │No                                       Exposure time        │
                  ▼                                         Acquisition length   │
         Preallocate memory for                             saveInt              │
         centroids and images                                                    │
                  │                                         Processing parameters:│
                  ▼                                                              │
          Get full-frame image,                             Threshold value     │
          set ROI and exposure                              Subwidth specification│
                  │                                         Skip rows            │
                  ▼                                  └──────────────────────────┘
               Start
          sequence acquisition
                  │
                  ▼
            While images ──Yes──► n % saveInt == 0? ──Yes──► Get image and metadata
            in buffer > 0                 │                           │
                  │No                     │No                         ▼
                  ▼                       ▼                  Place image and metadata
            Plot raw data          Get image only                in datastore
                  │                       │                           │
                  ▼                       ▼                           ▼
            Reset ROI,            Calculate centroids        Calculate centroids and
            start live view                                        save to file
                  │
                  ▼
         Save image datastores
                  │
                  ▼
                 End
```
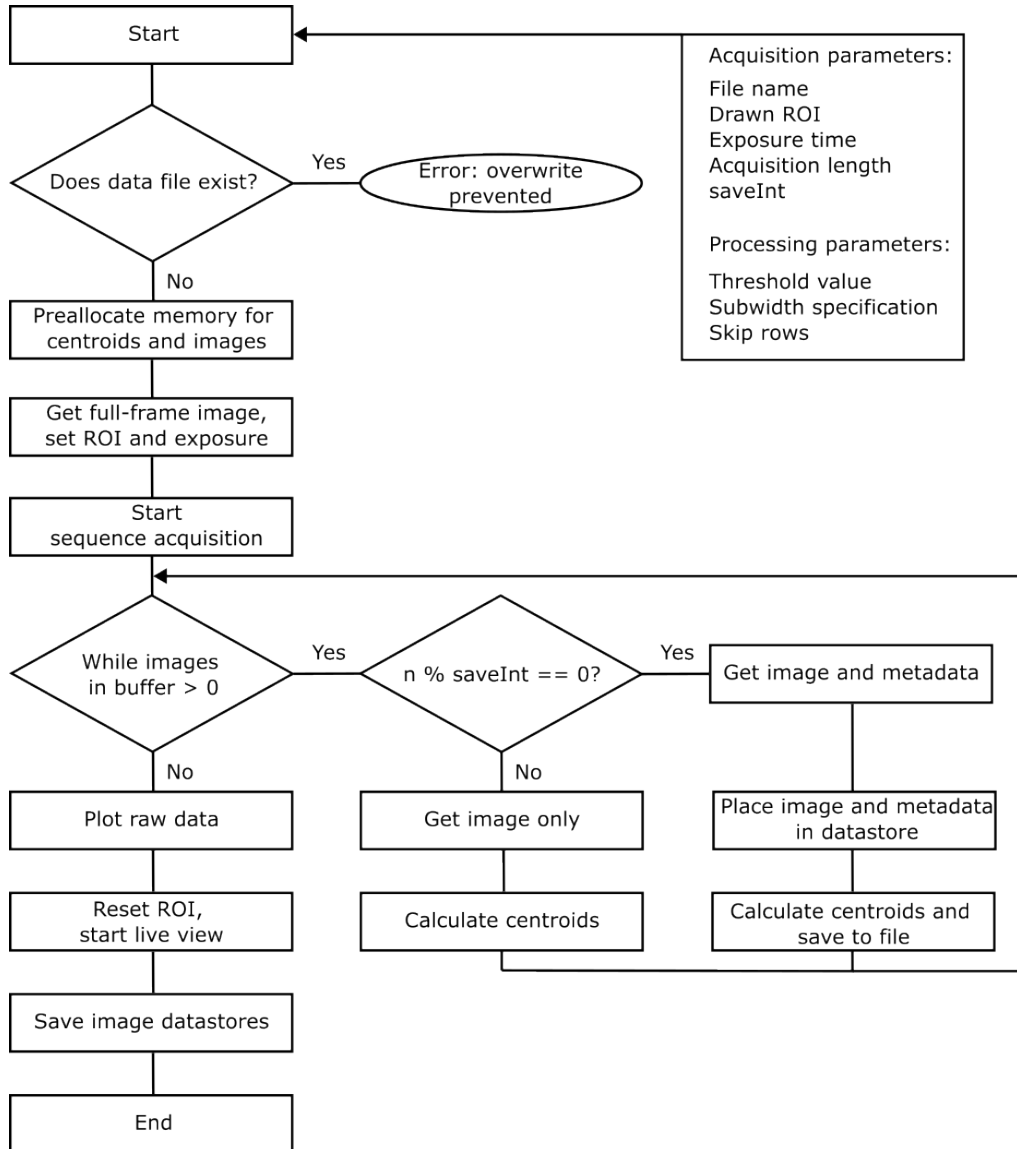
Figure A.1: Flowchart of Data Acquisition

Data acquisition script run by Micro-Manager. Before starting, the user draws a region of interest (ROI) and types a number of parameters for the acquisition and processing; these are defined in the accompanying text. First, the script checks to prevent overwriting data. Next, memory is allocated for centroids and datastores which will contain the saved images and metadata. Then exposure is set and a full-frame image is acquired; the ROI is set to the rectangle drawn by the user before starting the sequence acquisition. At this point, Micro-Manager handles the hardware control and reads images into a circular buffer. The processing loop consists of reading images from this buffer and processing them; one in every *saveInt* images (typically 1,000) are kept along with metadata, and every image acquired is processed to calculate centroids. Once the acquisition is finished, the raw data is plotted, the ROI is reset, and the image datastores are saved to disk.

Appendix B

Cell Culture and Preparation

B.1   Phonon Microscopy Experiments

Hela (ATCC CCL-2) cells were grown in Dulbecco's Modified Eagle Medium, supplemented with 10% (v/v) Fetal Bovine Serum (Merck: F9665), 1% (v/v) L-glutamine (Merck: G7513), 1% (v/v) Penicillin-Streptomycin solution (Merck: P0781) and 1% (v/v) Non-essential Amino Acid Solution (Gibco:11140-050); these were grown in a T75 flask using standard protocols for adherent cells.

Transducers were fabricated as described in C, sterilised in 70% ethanol, and coated with poly-L-lysine (P4832, Sigma-Aldritch) to aid cell adhesion. Coating was carried out per manufacturer's instructions.

B.1.1   Fixed Cells

Before fixed cell phonon microscopy experiments, 10^5 cells were seeded onto a transducer coverslip in a 35mm petri dish with 2ml of growth me-

dia as above. Cells were incubated overnight at 37°C with 5% CO_2, and before experiments cells were treated for 30 minutes with a drug dissolved in dimethyl sulphoxide (DMSO) and diluted in phosphate buffered solution (PBS, Fisher: BP3991), or the same concentration of DMSO in PBS without drug. After treatment, cells were rinsed in PBS and fixed in 5% formalin solution for 20 minutes. The sample holder was flushed with ethanol and rinsed twice with water before being assembled with the coverslip and filled with degassed distilled water.

B.1.2 Live Cells

Before live cell phonon microscopy experiments, 10^5 cells were seeded onto a transducer coverslip in a 35mm petri dish with 2ml of growth media as above. Cells were incubated overnight and before experiments the sample holder was flushed with ethanol and rinsed twice with cell media before being assembled with the coverslip and filled with media. The media was supplemented with 20µg/ml Calcein-AM (ThermoFisher, USA, C3099) for fluorescent viability imaging.

B.2 Confocal Imaging

Cytoskeletal staining for confocal imaging was performed following instructions available online from Cramer and Desai[214]. Hela S3 (ATCC CCL-2) cells were grown as for microrheology experiments (Section 4.2); for confocal imaging, 10^5 cells were seeded onto glass coverslips in a 6-well plate with 2ml of growth media as above. Cells were incubated overnight, and treated with Latrunculin B dissolved in DMSO and diluted in PBS or an equivalent concentration of DMSO in PBS. After treatment, cells were rinsed

with PBS fixed in 5% formalin for 20 minutes and permeabilised with 0.5% triton-X in PBS for 10 minutes.

Actin was stained using rhodamine phalloidin dissolved in PBS for 15 minutes, after which cells were rinsed twice in PBS. Next, DNA was stained using Hoechst 33342 (ThermoFisher: H3570) for 10 minutes. Finally, the coverslips were mounted on microslides and imaged using a Zeiss Airyscan 2 confocal laser scanning microscope. Data were analysed and images were reconstructed using Zeiss Zen software.

Appendix C

OAT fabrication

Opto-acoustic transducers were fabricated following methods developed by members of the Optics and Photonics Research Group. Here I will described preparing substrates and fabricating transducers using sputter coating, characterising them using white light transmission spectroscopy, and recycling sapphire substrates.

First, the substrate (i.e. sapphire coverslip (WST-2515, UQG Optics, UK)) was cleaned using a series of solvent baths in a sonicator. The solvents used (in order) were ethyl lactate, acetone, methanol and isopropanol. After each one, the substrate was dried using a nitrogen gun.

Next, the substrate was placed in the sputter coater (HHV BT300 bench-top sputter coater) on top of a glass microslide and the vacuum pumps run to a pre-process pressure of 10^{-4}mbar. By empirical observations, the microslide under the substrate aided in transducer adhesion to the substrate, although the mechanism is unknown. The substrate and glass microslide were held in place using kapton tape. Sputterer recipes were calculated using calibrations for deposition time against layer thickness which are
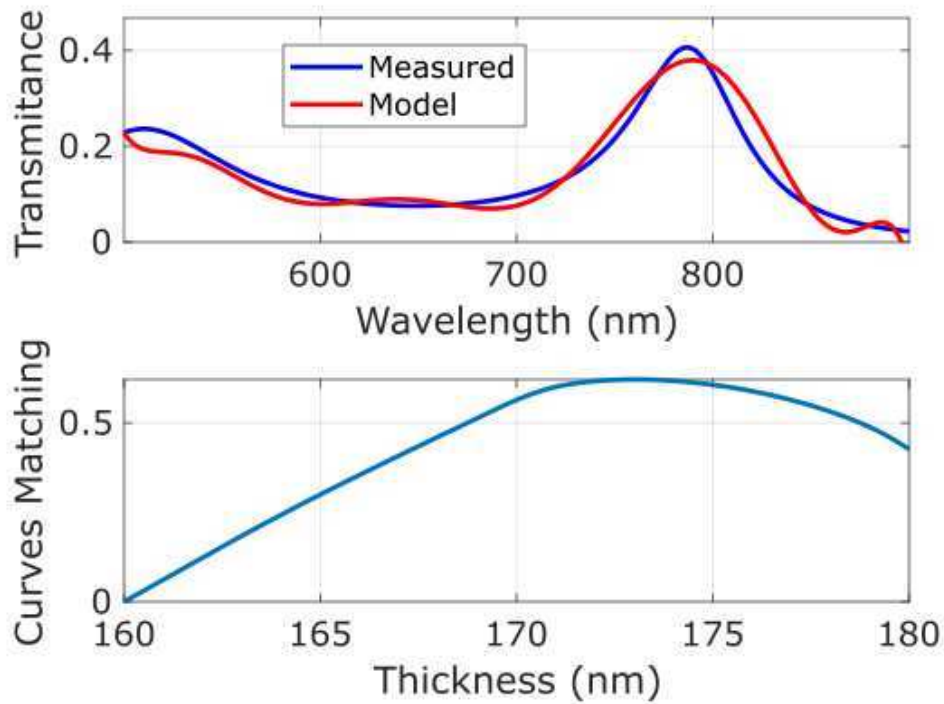
Figure C.1: Transducer Characterisation

After fabrication, transducers were characterised with white light transmission spectroscopy. Top: experimentally measured spectrum compared to model spectrum for 21-173-21nm transducer. Bottom: fit quality for different thicknesses of the ITO (middle) layer.

available as a shared resource.

After sputter coating, white light transmission spectra were acquired for the transducer and bare substrate; this is demonstrated in Figure C.1. An optical model was used to predict the transmission spectra given the user's guess at the layer dimensions. The fit quality of the model with a range of dimensions was compared to the experimental data and the best fit chosen.

After experiments, transducers were either reused or stripped so the sapphire could be recoated. Removal of the transducer was performed using either piranha solution or hot methanol and hydrochloric acid. All chemicals were used within a fume hood at all times. Piranha solution was made by mixing 1.5ml of hydrogen peroxide with 4.5ml of concentrated sulphuric

acid, and the transducer was placed into this immediately. Alternatively, methanol was mixed with an equal volume of concentrated hydrochloric acid, and transducer was added to the mixture and sonicated in a water bath set to 80°C. In either case, the waste was neutralised with sodium bicarbonate before disposal.